

Die approbierte Originalversion dieser Dissertation ist an der Hauptbibliothek der Technischen Universität Wien aufgestellt (<http://www.ub.tuwien.ac.at>).

The approved original version of this thesis is available at the main library of the Vienna University of Technology (<http://www.ub.tuwien.ac.at/englweb/>).

DISSERTATION

# The ALICE Silicon Pixel Detector System

ausgeführt zum Zwecke der Erlangung des akademischen Grades eines Doktors der technischen Wissenschaften unter der Leitung von

Ao. Univ. Prof. Dr. Christian W. Fabjan  
Atominstitut der Österreichischen Universitäten (E141)

eingereicht an der Technischen Universität Wien  
Fakultät für Physik



von

Dipl.-Ing. Fadmar Osmić

Matrikelnummer 9625893  
geboren am 14. März 1978 in Tuzla, Bosnien und Herzegowina  
Kohlgrasse 2a/29/2, A-1050 Wien

Diese Arbeit wurde unterstützt vom Österreichischen Bundesministerium für Bildung,  
Wissenschaft und Kultur.

Genf, am 12. Mai 2005



to my daughter Selma  
she is my *raison d'être*

mojim roditeljima  
vaš ponos je moja motivacija

für Julia  
für die Liebe und die Kraft



## Kurzfassung

Am CERN, der europäischen Organisation für Teilchenphysik in Genf wird derzeit der "Large Hadron Collider" (LHC) konstruiert, der es ermöglichen wird, subnukleare Phänomene mit noch nie dagewesener Präzision zu studieren. ALICE ("A Large Ion Collider Experiment") ist eines der vier großen Experimente am LHC. Es ist speziell für Kollisionen schwerer Ionen konzipiert, mit dem Ziel starkwechselwirkende Materie bei extremen Energiedichten zu beobachten. Es werden QCD-Phasenübergänge und die Physik des Quarkgluonplasmas untersucht.

Wie auch viele andere Experimente der Hochenergiephysik, verwendet auch ALICE Siliziumpixeldetektoren zur Teilchenspurbestimmung nahe am Kollisionspunkt. Der ALICE Silizium Pixel Detektor (SPD) bildet die beiden innersten Lagen des ALICE Experiments, und liefert aufgrund der hohen Granularität genaueste Informationen über die Teilchenspuren. Bei Schwerionenkollisionen kann es zu mehr als 80 Spuren/cm<sup>2</sup> in der ersten Lage des SPD kommen. Die Information über die Teilchenspuren wird bei 2 Radien gemessen: 3.9 cm und 7.6 cm vom Ort der Wechselwirkung entfernt. Die Ortsauflösung des SPD liegt bei rund 12  $\mu\text{m}$  in radialer Richtung. Eine der großen Herausforderungen des SPD sind die strengen Vorgaben an das Materialbudget (weniger als 1% X0 pro Lage), um jedweden Einfluss auf die den SPD durchquerenden Teilchen so gering wie möglich zu halten. Diese Beschränkungen wurden während der Design- und Produktionsphase aufs Genaueste eingehalten und so ist die gesamte Dicke des Detektors nur 350  $\mu\text{m}$  und die Leitungen für die Signale von der Auslese zur weiterverarbeitenden Elektronik am Detektor werden ausschließlich aus Aluminium hergestellt.

Die Ergebnisse dieser Arbeit erläutern die durchgeführten Messungen, die notwendig waren, um die Qualität der eingebauten Komponenten zu gewährleisten und die Detektorleistung zu charakterisieren und sie beschreibt die verschiedenen Produktionsphasen des SPD.

Kriterien zur Qualitätssicherung und Testprotokolle für die verschiedenen Komponenten des SPD wurden entwickelt und optimiert. Diese Tests beinhalten sowohl visuelle Kontrollen, elektrische Tests als auch Messungen mittels radioaktiver Quellen.

Zwei Strahltests wurden während der letzten Jahre durchgeführt. In 2003 wurde eine Pixelebene in einem Schwerionenstrahl als auch in einem Proton/Pionenstrahl untersucht. Vier weitere Pixelebenen wurden als Referenzebenen zur Teilchenspuranalyse verwendet. In 2004 fand ein Strahltest mit je zwei Lagen jedes Teildetektors des ALICE Inner Tracking Systems (ITS) statt. Zum ersten Mal wurden auch das ALICE DAQ System (DATE) und das ALICE Trigger System eingesetzt. Ein neuartiger Algorithmus zur Spurenanalyse, welches die Neigung und den Azimutalwinkel der Ebenen zueinander berücksichtigt, wurde speziell für den Proton/Pion Strahl entwickelt. Diese neue Methode erlaubt es auch Daten aus dem Strahltest 2003 mit nicht fokussiertem Strahl zu analysieren. Weiters wurde eine Studie zur Clustergröße in Abhängigkeit des Schwellwerts und Teilcheneinfallswinkels, durchgeführt, um einen Vergleich zwischen 2 verschiedenen Sensordicken (200 und 300  $\mu\text{m}$ ) herzustellen.

Ein auf einem gepulsten Infrarot Laser basierendes Testsystem wurde entwickelt, um SPD Prototypmodule und das FastOr Signal des Pixelchips zu testen. Dieses Testsystem erlaubte zum ersten Mal eine Arbeitseinstellung und eine komplette Charakterisierung des im Auslesechip intern generierten FastOr Signals. Dieses Signal wird zur L0-Triggerentscheidung während des ALICE Proton-Proton Programms beitragen. Zum ersten Mal wird in einem großen Experi-

ment der Hochenergiephysik die Information über eine Teilchenspur aus einem Pixeldetektor als "low level trigger" herangezogen. Weiters gelang eine detaillierte Charakterisierung des ALICE1LHCb-Chips unter genau definierter zeitlicher Korrelation und Energieabgabe an den Siliziumsensor. Die Kalibrierung des Lasers erfolgte mit Hilfe des internen Schwellenwerts des Auslesechips und zweier radioaktiver Quellen ( $^{55}\text{Fe}$  und  $^{109}\text{Cd}$ ). So wurde im Rahmen dieser Messungen zum ersten Mal eine absolute Kalibrierung des Detektors durchgeführt. Die Lasermessungen der Prototypmodule konnten direkt mit den Ergebnissen der Strahltests von 2002 und 2003 verglichen werden.

Ich habe während meiner Doktorarbeit am CERN Testkriterien für die SPD Komponenten entwickelt und angewandt. Weiters habe ich ein Testsystem basierend auf einem Infrarot Laser aufgebaut, das eine detaillierte Charakterisierung des Detektors, eine spezielle Studie der Clustergrößen und die Funktionalität des FastOr Signals erlaubt. Die durch den Laser erhaltenen Ergebnisse der Clustergrößen wurden mit den Resultaten aus den Daten der Strahltests verglichen.

## Abstract

The European Organization for Particle Physics (CERN) in Geneva is currently constructing the Large Hadron Collider (LHC), which will allow the study of the subnuclear ranges of physics with an accuracy never achieved before. Within the LHC project, ALICE is dedicated to the study of strongly interacting matter at extreme densities and high temperatures.

ALICE as many other modern High Energy Physics (HEP) experiments uses silicon pixel detectors for tracking close to the interaction point (IP). The ALICE Silicon Pixel Detector (SPD) will constitute the two innermost layers of ALICE, and will due to its high granularity provide precise tracking information. In heavy ion collisions, the track density could be as high as 80 tracks/cm<sup>2</sup> in the first SPD layer. The SPD will provide tracking information at radii of 3.9 and 7.6 cm from the IP. It is a fundamental element for the study of the weak decays of the particles carrying heavy flavour, whose typical signature will be a secondary vertex separated from the primary vertex by a few hundred microns only. The SPD will provide a spatial resolution of around 12  $\mu\text{m}$  in the  $r\varphi$ -direction. One of the specific challenges for the ALICE SPD will be the stringent material budget constraints ( $<1\%$  per layer) in order to have as small as possible influence on the traversing particles. In the design and production process, these constraints were followed to the point, so will the sensor and the readout chip have a total thickness of only 350  $\mu\text{m}$  and the signal lines from the front-end to the on-detector electronics will be deployed in complete aluminum.

The results presented in this thesis illustrate the measurements performed in order to characterize the detector performance and qualify components for inclusion in the detector and depicts the work carried out needed for the production phase of the SPD.

Quality assurance criteria and test procedures have been developed and fine-tuned for the different components of the SPD. The tests involved visual inspection, electrical tests as well as measurements using a radioactive source.

Two beam tests were carried out in the past years. In October 2003 one pixel plane was studied in a heavy ion beam as well as in a proton/pion beam. Four other pixel planes were used as reference planes for tracking. In November 2004 a joint beam test with two planes of each subdetector of the ALICE Inner Tracking System (ITS) took place. For the first time the ALICE data acquisition system (DATE) and the ALICE trigger system were used with two planes of each subdetector. A new tracking algorithm for the proton/pion beam data taking the tilt and the azimuthal angle into account was developed. With this new tracking method it was possible also to analyze the data taken at the wide beam setting during the beam tests 2003. Further, a study of the cluster sizes as function of different operating parameters, i.e. threshold, and track incidence angle was performed giving a comparison between two sensor thicknesses (200  $\mu\text{m}$  and 300  $\mu\text{m}$ ).

A test system based on a pulsed infrared laser was established in order to test SPD assemblies and the FastOr signal generated by the pixel chip. This laser allowed for the first time a complete characterization of the working point and performance of the chip internally generated FastOr signal. This signal will contribute to the L0 trigger decision in ALICE proton-proton runs. It will be the first time a large high energy physics experiment uses tracking information from a pixel detector for low level triggering. Furthermore, the setup allowed a detailed study

of the ALICE1LHCB chip characteristics with well defined timing and energy deposition in the silicon sensor. A laser calibration was performed using the internal threshold DAC and two radioactive sources ( $^{55}\text{Fe}$  and  $^{109}\text{Cd}$ ) providing a precise absolute calibration of the detector for the first time. The laser measurements on ALICE assemblies could directly be compared with the results of the beam test 2002 and 2003.

During my doctoral thesis at CERN, I have developed and applied test criteria for the SPD components. Furthermore, I developed an infra red laser test system which allowed a detailed study of the detector performance, a special cluster size study and the functionality of the FastOr signal. The cluster size studies obtained with the laser measurements are compared with the results from the beam test data taken in high energy particle beams.

## Acknowledgements

First of all I would like to thank Prof. Christian Fabjan for wakening my interest in particle and detector physics and offering me the possibility of carrying out my PhD at CERN.

The happy conclusion of this work is due to the understanding, guidance and support of my supervisor Dr. Petra Riedler. I always could count on her knowledge and experience in the field of silicon detectors.

I am especially grateful to Giorgio Stefanini for welcoming me in the ALICE SPD group and for his advice during the development phase of the laser setup. I would also like to thank Paul Nilsson, Jan Conrad, Domenico Elia, Federico Attinori and Henrik Tydesjo for their help with the beam test analysis.

I am equally indebted to Michael Campbell and Lukas Tlustos for their advice and fruitful discussions concerning the laser calibrations and measurements. Knowing that I could count on them whenever I experienced difficulties meant very much to me.

Many thanks are due to the SPD team for making me feel welcome in their midst and making my time at CERN so agreeable. I value their help very highly and I especially would like to thank Alex Kluge, Andrea Boccardi, Michael Burns and Michel Morel for their help in electronics.

Maurice Glaser deserves a special recognition for his help with the laser and for allowing me to use another two lasers, which made the measurements on diffusion and mobility of charge carriers complete.

My stay here would not have been the same had it not been for the friendship of so many. All the Austrians who helped keep up my morals and made me feel never far from home, my fellow team players and opponents from various soccer teams: GOZO, CERN, Echenevex.

Last but not least I want to mention some special people: Richard, who put away his literature for a while to correct and proof read my thesis in unaccountable long nights,

my daughter Selma, who might only begin to comprehend how much strength I draw from her existence and who was probably even happier than me that I had finished the writing of my PhD-thesis,

my parents who never held me back but encouraged me in all my dreams, and my girlfriend Julia, who is the only person who knows.



# Contents

<b>1</b>	<b>The ALICE Experiment at CERN</b>	<b>1</b>
1.1	Introduction . . . . .	2
1.2	LHC . . . . .	2
1.2.1	The LHC Experiments . . . . .	5
1.3	ALICE . . . . .	5
1.3.1	Quark Gluon Plasma (QGP) . . . . .	6
1.3.2	QGP Signatures . . . . .	7
1.3.3	Proton-Proton Physics . . . . .	9
1.3.4	The ALICE Detector System . . . . .	9
1.4	Inner Tracking System (ITS) . . . . .	10
1.5	The ALICE Silicon Pixel Detector (SPD) . . . . .	11
<b>2</b>	<b>Semiconductor Particle Detectors</b>	<b>15</b>
2.1	Introduction . . . . .	16
2.2	General Principle of Silicon Detectors . . . . .	16
2.2.1	Charge Carrier Generation . . . . .	16
2.2.2	Charge Carrier Transport . . . . .	20
2.2.3	Intrinsic and Doped Silicon . . . . .	22
2.2.4	p-n junction . . . . .	24
2.3	Hybrid Pixel Detectors . . . . .	26
2.3.1	Pixel Detectors at LHC . . . . .	28
2.3.2	Future Pixel Detectors . . . . .	30
<b>3</b>	<b>The ALICE Silicon Pixel Detector (SPD)</b>	<b>33</b>
3.1	Introduction . . . . .	34
3.2	Components of the ALICE SPD . . . . .	34
3.2.1	The Readout Chip . . . . .	35
3.2.2	The Pixel Cell . . . . .	36
3.2.3	SPD Sensor . . . . .	38
3.2.4	Flip Chip Bonding of the SPD Ladders . . . . .	39
3.2.5	Front-end and Readout Electronics . . . . .	42

3.2.6	Half-Stave and Sector Assembly . . . . .	45
3.3	ALICE SPD Test Setup . . . . .	50
3.3.1	Readout Chain Architecture . . . . .	50
3.3.2	Test System Software . . . . .	51
3.4	Summary . . . . .	52
<b>4</b>	<b>Test Protocols in Production - Results</b>	<b>55</b>
4.1	Introduction . . . . .	56
4.2	ALICE SPD Probe Station . . . . .	56
4.3	Readout Chip Wafer Testing . . . . .	58
4.3.1	Test Procedure and Criteria . . . . .	58
4.3.2	Results - Readout Chip Yield . . . . .	61
4.4	Ladder Testing . . . . .	63
4.4.1	Ladder Test Procedure and Test Protocol . . . . .	63
4.4.2	Measurements and Results . . . . .	65
4.5	Sensor Tests . . . . .	68
4.5.1	Visual Inspection . . . . .	68
4.5.2	Study of the Back-Side Aluminum Adhesion . . . . .	71
4.5.3	Wire Bond Tests . . . . .	72
4.6	Metrology Measurements on Sensor Wafers and Ladders . . . . .	74
4.7	Summary . . . . .	76
<b>5</b>	<b>Beam Tests and Analysis</b>	<b>79</b>
5.1	Beam Test 2003 . . . . .	80
5.1.1	Experimental Setup . . . . .	80
5.1.2	Results . . . . .	83
5.2	Combined ITS Beam Test 2004 . . . . .	93
5.2.1	Experimental Setup . . . . .	94
5.2.2	Offline Analysis within the AliRoot Framework . . . . .	98
5.2.3	Cluster Study - Comparison BT 2003 and 2004 . . . . .	100
5.3	Summary . . . . .	103
<b>6</b>	<b>Development of an Infrared Laser Test System</b>	<b>105</b>
6.1	Introduction . . . . .	106
6.2	Laser Test Setup . . . . .	106
6.3	Laser Light Characteristics . . . . .	108
6.4	Laser Calibration . . . . .	109
6.5	Measurements carried out with the Laser Setup . . . . .	116
6.5.1	Time Walk of the Discriminator and the Delay Scans . . . . .	116
6.5.2	Study of the Sensitive Pixel Area . . . . .	118
6.5.3	Charge Sharing Measurements . . . . .	121

6.5.4	Bias scans . . . . .	127
6.6	FastOr-Study . . . . .	131
6.6.1	The FastOr Signal and the ALICE Trigger . . . . .	132
6.6.2	Chip Latency Measurements . . . . .	135
6.6.3	FastOr-Signal . . . . .	138
6.7	Summary . . . . .	144
<b>7</b>	<b>Conclusions</b>	<b>145</b>
<b>A</b>	<b>Scanning Electron Microscopy Functionality</b>	<b>149</b>
A.1	Introduction . . . . .	149
A.2	Working Principle . . . . .	149
A.3	Sample Preparation . . . . .	151
A.4	Lens Defects . . . . .	152
<b>B</b>	<b>Geometry Setup for the Beam Test 2003</b>	<b>153</b>
	<b>Bibliography</b>	<b>157</b>



# Chapter 1

## The ALICE Experiment at CERN

### Contents

---

1.1	Introduction . . . . .	2
1.2	LHC . . . . .	2
1.2.1	The LHC Experiments . . . . .	5
1.3	ALICE . . . . .	5
1.3.1	Quark Gluon Plasma (QGP) . . . . .	6
1.3.2	QGP Signatures . . . . .	7
1.3.3	Proton-Proton Physics . . . . .	9
1.3.4	The ALICE Detector System . . . . .	9
1.4	Inner Tracking System (ITS) . . . . .	10
1.5	The ALICE Silicon Pixel Detector (SPD) . . . . .	11

---

## 1.1 Introduction

The Standard Model [1] is a well established theory in good agreement with all confirmed accelerator data. It is a quantum field theory that describes the elementary particles of matter and their interactions. Gravitation, the weakest of the four fundamental forces is not included in the Standard Model. The other three forces are: The Strong interaction, the weak interaction and the electromagnetic interaction. In the standard model, the matter consists of leptons and quarks. There are 6 leptons and six quark flavors, arranged in three families, as illustrated in Figure 1.1. The quarks are called up, down, charm, strange, top and bottom. For each flavor there is also a corresponding anti-quark. The top row has electric charge  $q = \frac{2}{3}e$  and the bottom row has  $q = -\frac{1}{3}e$ , where  $e$  is the charge unit, i.e. the electric charge of the electron.

$$\begin{pmatrix} \nu_e \\ e^- \end{pmatrix} \begin{pmatrix} \nu_\mu \\ \mu^- \end{pmatrix} \begin{pmatrix} \nu_\tau \\ \tau^- \end{pmatrix}$$

$$\begin{pmatrix} u \\ d \end{pmatrix} \begin{pmatrix} c \\ s \end{pmatrix} \begin{pmatrix} t \\ b \end{pmatrix}$$

Figure 1.1: The three quark and lepton families.

Although, the standard model has been proven in various experiments with an accuracy of  $10^{-3}$  to  $10^{-4}$ , one important mechanism still lacks the experimental verification. The electroweak symmetry breaking mechanism, called Higgs-mechanism [2], introduces mass to the point like particles in the Standard model. The associated particle, the Higgs boson, could not yet be observed experimentally. Its lower mass is set by LEP<sup>1</sup> to 114.4 GEV and an upper mass exceeding 1 TeV [3] would contradict the Standard Model. The energies achieved in proton-proton collisions at the Large Hadron Collider (LHC) at CERN will be considerably higher than in any other experiment and, thus will allow the production of the Higgs boson in this energy range. Although, the main purpose of the Large Hadron Collider (LHC) at CERN will be the search for the Higgs boson and as such the verification of the Standard Model, other fields of physics will be addressed. A more precise measurement of already known particles (W-boson, b-quark, top-quark, ...) will be possible, since they will be produced at high rates. The lightest supersymmetric particles could be produced and detected. Further, the CP-violation in B-physics will be studied. An important part of the LHC project will be the study of strongly interacting matter at extreme densities and temperatures in a dedicated experiment, ALICE.

## 1.2 LHC

In 2007, a new age in particle physics will start. The LHC, the most-energetic ever built accelerator will become operational. It will allow the study of the subnuclear ranges of physics with an accuracy never achieved before. The LHC will consist of two colliding synchrotron

---

<sup>1</sup>Large Electron Positron Collider, a  $e^+e^-$  collider with a center of mass energy of up to 200 GeV.

beams. It will accelerate protons and heavy ions with the objectives of very high center of mass energies  $\sqrt{s}$  of up to 14 TeV and luminosities of up to  $10^{34} \text{ cm}^{-2}\text{s}^{-1}$  in p-p runs.

The LHC will consist of 8 sectors (shown schematically in Figure 1.2). Each octant will have bending magnets in the outer region, and focusing and defocusing quadrupole magnets as well as accelerating RF-cavities in the central straight sections, so called insertions. In order to stay cost-effective, it was decided to reuse the old LEP infrastructure as much as possible and thus the LHC will be hosted in the old 27 km LEP tunnel. In order to be able to keep the beam within the LEP radius at such high momentum of the beam, the machine features a magnetic system of 1232 dipole magnets with a strength of 8.4 T with a current of 11.7 kA. To achieve such high magnetic fields and simultaneously avoiding excessive resistive losses, the dipole magnets have to be superconducting. For this purpose, the magnets will be cooled down to  $\sim 1.9 \text{ K}$  using superfluid Helium at atmospheric pressure, which has very efficient heat transfer properties by much lower viscosity than in the liquid state.

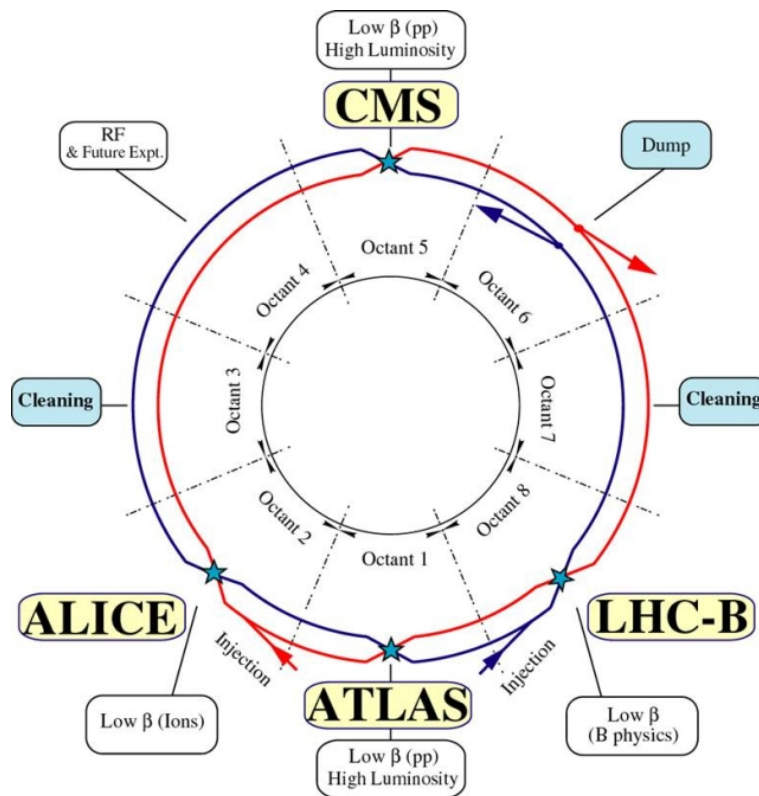


Figure 1.2: Schematic overview showing the four main experiments and the two ring structure of the LHC [4]

Contrary to LEP, where the electrons and positrons were circulating in the same beam pipe, the LHC will have two beam pipes for the two counter rotating beams. The two beam pipes will be housed in the same yoke and cryostat. A vertical B-field in the dipole magnets is induced by 6 superconducting blocks to guide the beams round the beam pipes. Pictures of the two beam

pipes and the magnetic field in one quarter of the dipole magnet are shown in Figure 1.3.

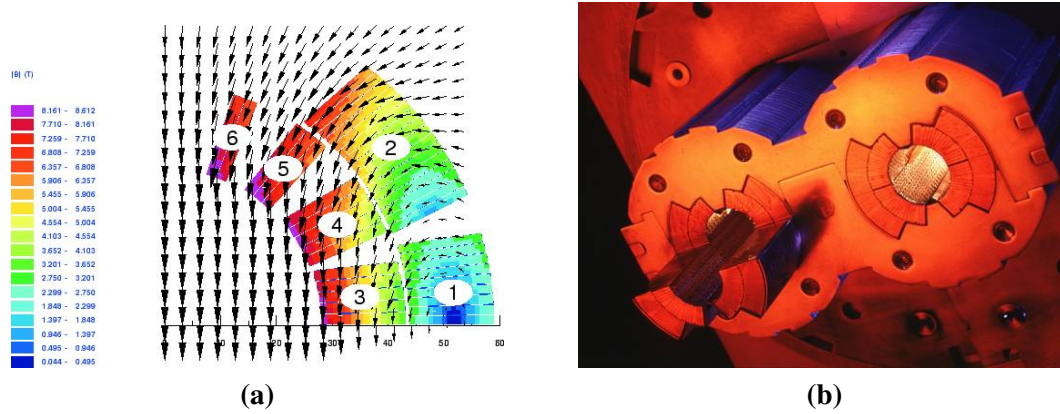


Figure 1.3: A quarter of a dipole aperture showing the 6 superconducting blocks and the magnetic field produced (a). Picture of the two dipoles forming the two beam pipes (b). [4]

At the nominal intensity, the bunch spacing in the LHC will be 7.48 m in space and 25 ns in time giving an interaction rate of 40 MHz. Each of the two beam pipes will be filled with 2808 bunches of  $1.15 \times 10^{11}$  protons at the start of the nominal fill. At the interaction points (IP) the transverse bunch radius will be squeezed down to  $16 \mu\text{m}$  in order to increase the probability of a collision. The focusing and bending of the beams on each other is shown in Figure 1.4. The bunch length will be 30 cm leading to a effective distribution of the vertex position along the beam axis of 5.5 cm (rms). The beams will be stored in the ring for about 10 to 20 hours before being dumped and the next insertion starts.

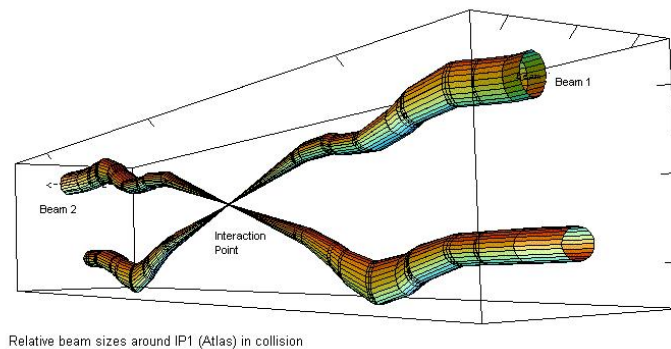


Figure 1.4: Relative beam sizes around IP1 (Atlas) in collision [4]

The LHC will also collide heavy ions (mostly  $\text{Pb}^{82+}$ ) with a total collision energy in PeV range. The luminosity in these runs will amount to  $L = 10^{27} \text{ cm}^{-2}\text{s}^{-1}$ . It will be smaller than in p-p runs due to limitations from the accelerator. The beam divergence will be larger due to higher charge of the ions and the performance of the detectors will be limited due to expected

high multiplicity in heavy ion runs.

### 1.2.1 The LHC Experiments

At the four interaction points of the LHC, four main detectors will be installed. While ALICE will be described in the subsequent chapter, a short outline of the other three detectors is given here:

- **A Toroidal LHC Apparatus (ATLAS)** will be installed in the interaction point 1 of the LHC. It uses two different magnetic field systems, an inner superconducting solenoid around the inner detector cavity with a 2 T field and an outer superconducting air cored toroid magnet system. ATLAS is a large-scale general purpose detector with the aim to exploit the full physics potential of the LHC. The main goal is the search for the Higgs boson and the detector is designed to be sensitive to largest possible Higgs masses. Also the search for heavy W and Z-like bosons will be covered, further the super symmetric particles and a detailed study of the top quark.
- **Compact Muon Solenoid (CMS)** is the second general-purpose experiment at CERN. In contrary to ATLAS, it uses only one magnetic system. A single superconducting solenoid generates a magnetic field of 4T. It is also designed to cover the full physics potential of the LHC. To achieve this, a precise measurement of the muons, leptons, photons and jets over a wide energy range will be done. The main detector systems are the Inner Tracker with ten layers of silicon strip detectors and silicon pixel detectors in the high occupancy range close to the interaction point. Further, an electromagnetic calorimeter with an excellent energy resolution and a muon system for momentum measurements up to highest luminosity. A special design feature of the CMS is the positioning of the ECAL inside the magnet. This arrangement will allow optimized detection of one of the main decay channels  $H \rightarrow \gamma\gamma$ .
- **LHCb** is designed for the Study of the CP violation in B-mesons decay at the LHC collider. In the LHC, the produced B-mesons are preferably produced in the forward direction and hence, LHCb is accomplished as a single arm spectrometer with an opening angle of 400 mrad with an acceptance of 10% to 20% of all Beauty decays. 21 layers of silicon detectors will provide excellent tracking information and also a very selective trigger in order to select Beauty events. LHCb will have two RICH systems in order to suppress background events and to provide B flavor tagging.

## 1.3 ALICE

An important part of the LHC project will be the study of strongly interacting matter at extreme densities (substantially larger than for ground state nuclei) and high temperatures. A Large Ion Collider Experiment (ALICE) is the dedicated experiment for these studies. According to current theories our universe evolved from a singular state of extreme energy densities, i.e. Big

Bang, to its present state through rapid expansion and cooling. After the Big Bang, the matter in the universe went through several phase transitions, like steam condensing into water. While most of these matter phases are not accessible by present experiments and will probably not be for a very long time, the transition from ordinary hadronic matter to the so called Quark Gluon Plasma (QGP) could be reached with the current accelerator technology. The Quantum Chromo Dynamcis (QCD), the quantum field theory describing the strong interaction between the quarks and the gluons, predicts that this phase transition should take place at a critical temperature of about 150 to 200 MeV, corresponding to an energy density of  $\epsilon_c \sim 1 \text{ GeVfm}^{-3}$  [5].

### 1.3.1 Quark Gluon Plasma (QGP)

Accelerators providing heavy ion collisions offer a possible way to create and study the QGP. By colliding ultra-relativistic heavy ions, the nuclei will be compressed to a point where individual hadrons will collapse and form the QGP. Figure 1.5 illustrates the formation of the QGP in a heavy ion collision. In this plasma, the quarks and gluons can exist for a very short time unbounded to any other particle and can move freely inside the whole, high density system. Besides this deconfinement, chiral symmetry is expected to be restored in the QGP, i.e. the quarks will have only their bare masses.

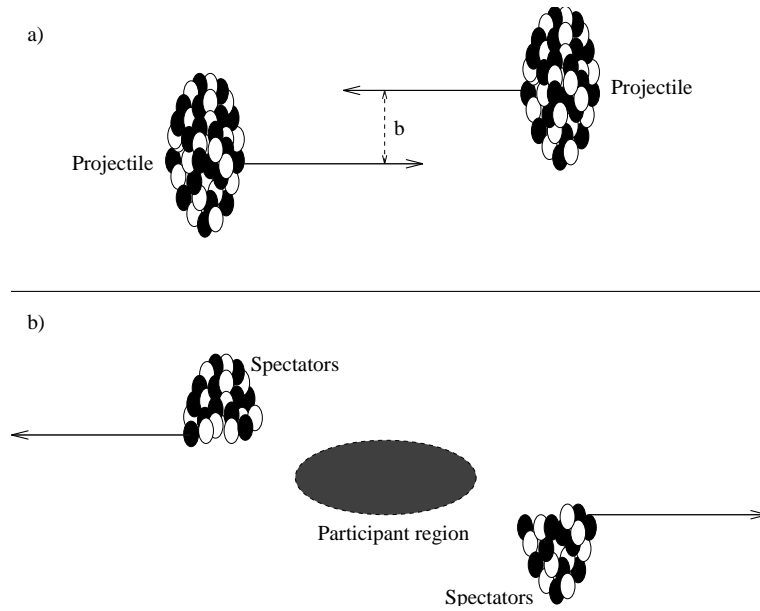


Figure 1.5: Schematic illustration of a collision between two heavy nuclei: (a) The two Lorentz contracted nuclei before the collision. The centrality is determined by the impact parameter  $b$ . (b) After the collision a participant region with high temperature and density is created. [6]

Heavy ion collisions at CERN-SPS and BNL-RICH have reported evidence for the QGP. Figure 1.6 shows a predicted phase diagram of nuclear matter as function of the temperature and the

ration of the baryon number and normal nuclear density. The increase in available energy in the collisions when going from SPS to LHC results in a higher temperature and more baryon free regions, where the number of particles and anti-particles are nearly equal. The highest QGP temperatures reached at heavy Pb-Pb collisions at LHC will be far from the phase transition region to allow a longer lifetime of the QGP.

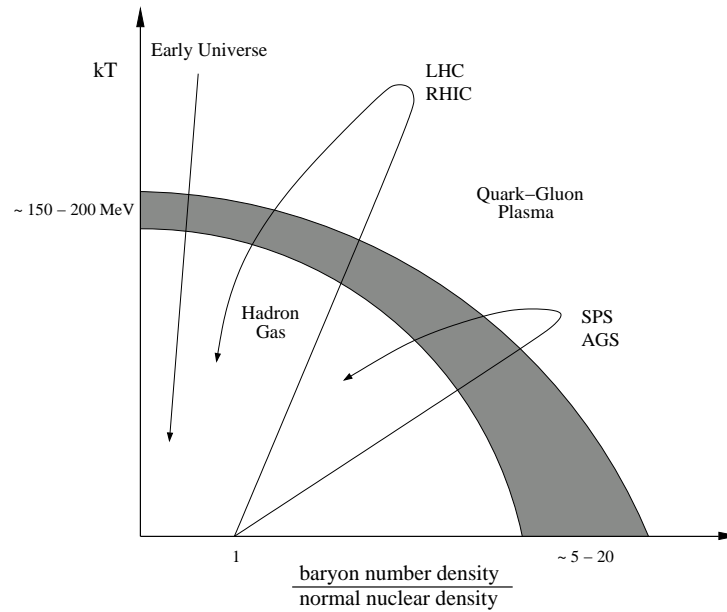


Figure 1.6: QCD phase diagram. Lattice QCD calculations at low baryon densities predict a phase transition at a temperature of about 150-200 MeV. [6]

### 1.3.2 QGP Signatures

The quarks and gluons coexisting in the QGP can not be observed directly due to the short life-time and the small spatial extension of the QGP. Therefore the informations from the early stages of universe may get lost when the system hadronizes. Various probes and observables have to be combined in order to get reliable proof of the formation of a QGP and to convey information about this medium. Some of these probes are coming directly from the QGP, like photons or leptons, which do not interact strongly and are therefore not affected by the plasma. By studying these probes a direct information from the QGP can be obtained. Another type of probes are those, which do interact strongly and hence, are modified or weakened in the QGP. Here the analysis relies mainly on comparison of these observables to the reference measurements taken during p-p or p-ion runs. Therefore, ALICE will, besides heavy ion collisions, also study proton-proton collisions. A description of the ideas behind some of the most promising signatures is given in the following paragraphs.

### Photon Production

The photons will be produced during different stages of the formation of the QGP. They interact only electromagnetically and have therefore a mean free path much larger than the size of the reaction volume. Since there are no final state interactions, like with hadrons, the photons provide a direct probe of the initial stages of the collision. Photons produced in the initial hard parton scattering are called prompt photons and they can reach an energy of up to several hundred GeV. They are followed by thermal photons produced in the QGP phase and the hadron gas phase with energies of up to a few GeV. An increase in the thermal photons is expected from a QGP. The production of the prompt photons can be calculated by means of the perturbative QCD (pQCD) and consequently validated by observing these photons. The huge background from the hadronic decays, e.g.  $\pi^0 \rightarrow \gamma\gamma$  and  $\eta \rightarrow \gamma\gamma$ , and the low production rates of direct photons make the detection of these photons very difficult.

### Dileptons

Dileptons are lepton - antilepton pairs, like  $(e/e^+$  or  $\mu/\mu^+$ , and they are produced throughout the evolution of the system. Like the direct photons, dileptons also offer a direct measurement of the QGP. They are an important tool for measuring the temperature and the dynamical properties of the matter produced in the heavy ion collision. The rate of the dileptons can be calculated using the pQCD.

### Jet Quenching

In heavy ion collisions, the incident hadrons break apart creating inter alia energetic colored partons. They undergo a cascade of decays and fragment finally into jets of particles. The propagation of partons through a hot and dense medium modifies their transverse momentum due to induced radiative energy loss, a phenomenon called "jet quenching". This results in the suppression of the high  $p_T$  particles and can therefore be studied by measurement of the momentum spectra. When a hard collision producing two jets occurs near the surface of the interacting region, jet quenching might lead to the weakening or complete absorption of one of the jets. This can be studied with azimuthal back-to-back correlation of the jets. By comparing the high- $p_T$  spectra from heavy ion and p-p collisions, the jet quenching can be verified.

### Strangeness Enhancement

In a QGP, the energies are high enough to allow production of heavy quarks. Since, the quarks are fermions, the creation of  $u\bar{u}$  and  $d\bar{d}$  pairs might be blocked due to the Pauli principle. In this case the  $s\bar{s}$  pairs will be favored in spite of their large energy mass. Here again, the comparison with the reference data from the p-p collisions will prove this effect of the QGP.

### $J/\Phi$ -Suppression

The  $J/\Phi$  particle is a bound state of a  $c\bar{c}$  pair. It is believed that the production of this particle will be suppressed in a QGP due to Debye screening. Also here, a comparison with the data from the p-p collisions, can prove the presence of the QGP.

### 1.3.3 Proton-Proton Physics

An integral part of the ALICE physics will be the proton-proton program. This will allow a first insight into pp physics at a new energy domain. A study of soft hadronic physics and the better understood high  $p_T$  region will be possible. It will also provide reference data for the study of heavy ion collisions using the same experimental setup and therefore reduce systematic errors in spatial and momentum acceptance, magnetic field, etc. Further, the low multiplicity data and therefore also simpler data will allow to commission and calibrate the various components of the ALICE detector. [7]

### 1.3.4 The ALICE Detector System

ALICE, depicted in Figure 1.7, is a 60 m long, 16 m wide, cylinder like detector consisting of a central detector system and several forward systems. The central system is placed in the former L3 warm solenoidal magnet, which produces a magnetic field of 0.5 T. The design of ALICE had to take into account the requirements to track and identify low momentum as well as high momentum particles. Further, secondary vertices coming from the decay of the short lived particles, such as D and B mesons, have to be reconstructed. The Experiment has to cope with highest particle multiplicities anticipated from the Pb-Pb collisions, up to 8000 particles per unit of rapidity at mid-rapidity.

To fulfill these requirements, ALICE will deploy, seen from the interaction point to the outside, 6 layers of high-resolution silicon detectors (Inner Tracking System - ITS), which together with the Time Projection Chamber (TPC) and a high granularity Transition Radiation Detector (TRD) will perform the tracking. The TRD, will also provide electron identification. It will be followed by the Time Of Flight (TOF) array for particle identification. These detectors cover the full azimuthal angle in a mid-pseudo-rapidity range of  $|\eta| \leq 0.9$ . The central system is concluded with two small-area detectors. An array of ring-imaging Cherenkov High Momentum Particle Identification Detectors - HMPID ( $|\eta| \leq 0.6$ ,  $57.6^\circ$  azimuthal coverage) and a high-density PHOTon Spectrometer (PHOS) as the electromagnetic calorimeter ( $|\eta| \leq 0.12$ ,  $100^\circ$  azimuthal coverage) [10].

The forward systems consists of a muon spectrometer ( $-4.0 \leq \eta \leq -2.4$ ), a Photon Multiplicity Detector (PMD), a silicon strip array of multiplicity detectors (Forward Multiplicity Detectors - FMD) covering the pseudo-rapidity region (up to  $\eta = 5.1$ ). The muon spectrometer is shielded by an absorber positioned close to the vertex point and consists of a dipole magnet, five tracking stations, an iron wall (muon filter) to absorb remaining hadrons, and two trigger stations

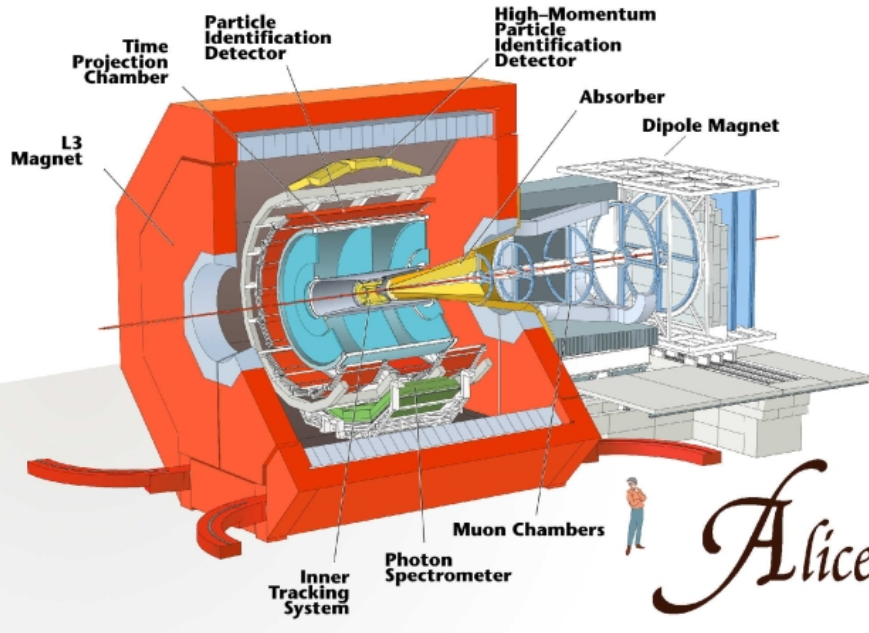


Figure 1.7: Layout of the ALICE detector. [9]

behind the muon filter. A set of scintillator and quartz counters in the forward region (V0 and T0 detectors) will contribute trigger information for the ALICE experiment. Further, two sets of neutron and hadron calorimeter in the far forward region, i.e. about 115 m away from the interaction point (IP) and at  $0^\circ$ , will measure the impact parameter. A detailed description of the different subsystems of ALICE is given in ALICE Technical Proposal [8] and ALICE Physics Performance Report [5].

## 1.4 Inner Tracking System (ITS)

The high background in heavy-ion collision will require very precise track finding. In order to achieve as good as possible two-track resolution, ALICE uses three-dimensional hit information wherever feasible. The TPC is the main tracking device, but due to large track densities close to the IP, the tracking at smaller radii is carried out by the ITS [10].

The ITS consists of 6 cylindrical layers at radii 3.9, 7.6, 15, 24, 30 and 44 cm from the interaction point. The number and position of the layers are optimized for efficient tracking and impact parameter resolution. The outer radius is determined by the track matching of the TPC and the inner radius by the geometrical constraints of the beam pipe. The ITS will cover the pseudo-rapidity range of  $|\eta| \leq 0.9$  for all vertices inside the interaction diamond ( $\pm\sigma$ ), i.e. 10.6 cm along the beam direction. The high particle density (about 80 per  $\text{cm}^2$ ) makes truly two-dimensional silicon detectors necessary and for this reason, the 4 innermost layers of the ITS are chosen to be each two layers of Silicon Pixel Detectors (SPD) and Silicon Drift De-

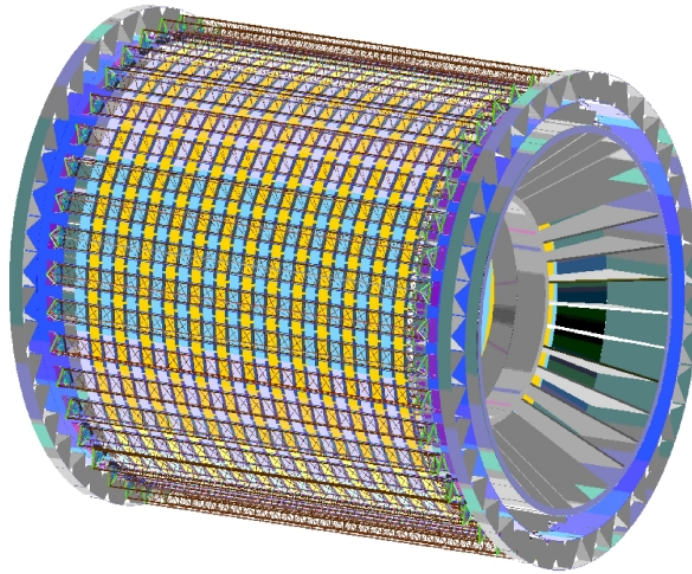


Figure 1.8: Layout of the ITS detector.[11]

tectors (SDD). The outer layers, where the particle density is expected to be below  $1 \text{ cm}^{-2}$  will consist of double sided Silicon Strip Detectors (SSD). Due to the analog readout of the SDD and SSD layers, the ITS will be able to provide  $dE/dx$  measurements and therefore identify low- $p_T$  particles. As a matter of fact, the low-momentum particles (below  $100 \text{ MeV}/c$ ) will be detectable only by the ITS. The most important objectives of the ITS are:

- location of the primary vertex with a resolution better than  $100 \mu\text{m}$
- reconstructing the secondary vertices from decays of hyperons and D and B mesons
- low momentum (below  $100 \text{ MeV}/c$ ) particle tracking and identification
- improvement of the momentum and angle resolution for the high- $p_t$  particles together with the TPC
- reconstruction, although with limited momentum resolution, of particles traversing the dead regions of the TPC

## 1.5 The ALICE Silicon Pixel Detector (SPD)

The SPD (shown in Figure 1.9 as a part of the ITS) will constitute the two innermost layers of ALICE, and will operate in a region where the track density could be as high as  $80 \text{ tracks}/\text{cm}^2$ . The only possibility to cope with such high densities is the use of detectors of high precision and granularity. The pixel layers will have to cope with the highest radiation doses in ALICE,

i.e.: the expected Total Ionizing Dose (TID) for 10 years running time received by the inner layer is estimated to be 275 krad and 68 krad by the outer layer. The integrated neutron flux (1 MeV neutron equivalent) is calculated to be  $\sim 6.4 \times 10^{11} \text{ n}_{\text{eq}}/\text{cm}^2$  in the inner layer and  $\sim 3.7 \times 10^{11} \text{ n}_{\text{eq}}/\text{cm}^2$  in the outer layer [13].

The ALICE SPD will employ two-dimensional silicon hybrid detectors with reverse-biased silicon detector diodes flip-chip bonded to readout chips (see chapter 2 for a more detailed description of hybrid silicon detectors). In total, the SPD will have about  $9.8 \times 10^6$  channels with a pixel size of  $50 \mu\text{m}$  by  $425 \mu\text{m}$ . A high segmentation leads to a low individual diode capacitance, resulting in low noise levels.

The readout of the SPD is binary: a threshold is applied to the preamplified and shaped signal, and each cell outputs a logical one if the threshold is exceeded. A detailed description of the architecture and the layout of the ALICE SPD is given in chapter 3.

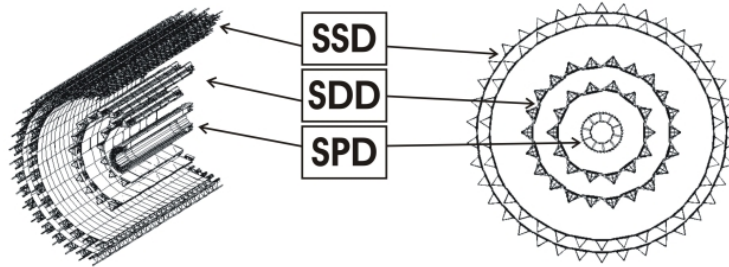


Figure 1.9: Illustration of the arrangement of the ITS subdetectors. The ALICE SPD constitutes the two innermost layers [5].

The ALICE SPD is a fundamental element for improving the spatial precision in the measurement of the charged tracks when propagated back to the interaction vertex. The measurement of particles carrying heavy flavor (charm and beauty) will be mainly based on the spatial precision achievable with the ALICE SPD [5]. These particles can be identified by reconstructing their weak decays, whose typical signature is a secondary vertex separated in space from the primary vertex by a few hundred microns only. Therefore, the impact-parameter resolution must be better than  $100 \mu\text{m}$  in the  $r\varphi$  plane. To achieve this, the SPD as the closest detector to the interaction point will have the best precision of around  $12 \mu\text{m}$  in the  $r\varphi$ -direction.

The ALICE SPD will have a faster readout than the other ITS detectors, since it will be triggered by other detectors. While the centrality trigger activates the readout of all ALICE detectors, the trigger of the muon arm will activate only a subset of detectors including the two pixel layers. The readout time of the SPD will be about  $260 \mu\text{s}$  and matches that of the muon chambers [8].

In Figure 1.10 the event display of a  $D^0 \rightarrow K^- \pi^+$  decay in a central Pb-Pb collision in transverse direction is shown. The digits in the two layers of the SPD are visualized. The trajectories of the particles from the Pb-Pb collision are shown for a limited azimuthal angle only. The topology of the event and the detection strategy are shown in Figure 1.11. The impact parameter  $d_0$

amounts to  $\sim 100 \mu\text{m}$ .

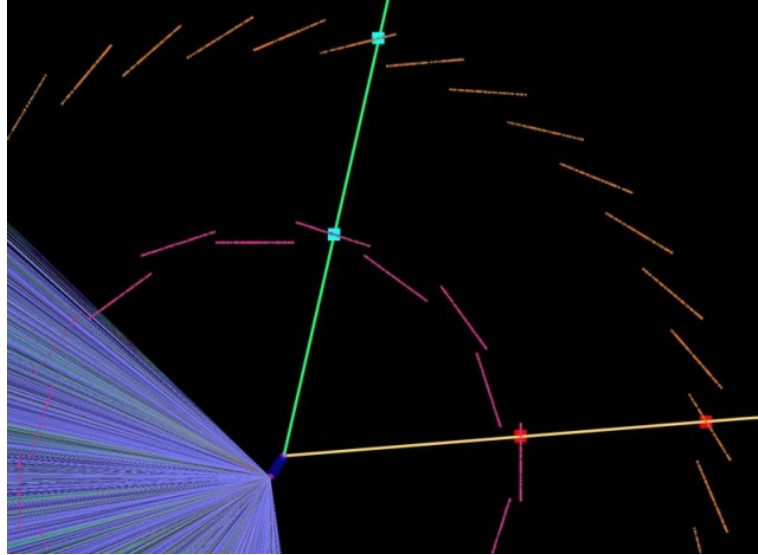


Figure 1.10: Simulation of an  $D^0 \rightarrow K^- \pi^+$  decay in a central Pb-Pb collision in transverse direction. The digits in the two layers of the SPD are visualized; the value of the magnetic field is set to zero. The background coming from the Pb-Pb collision is shown only for a limited azimuthal angle.[12]

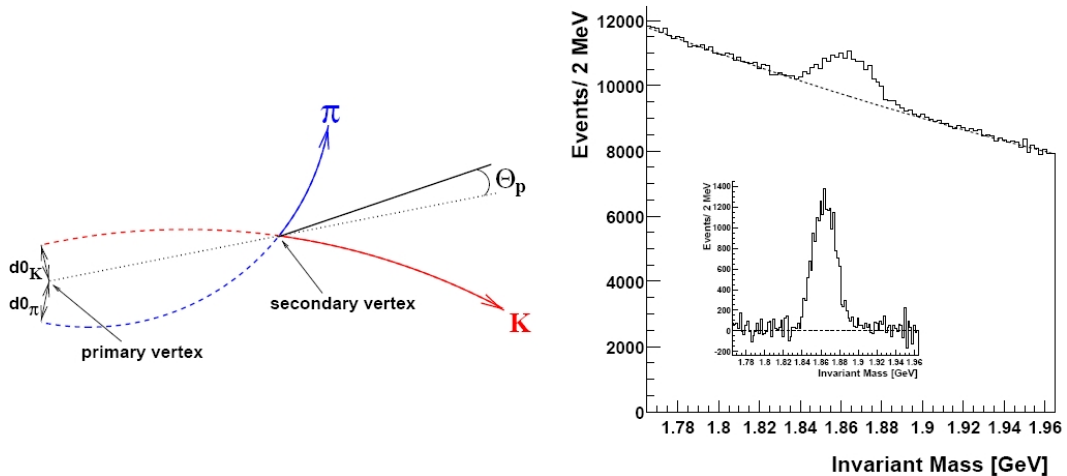


Figure 1.11: Schematic representation of the  $D^0 \rightarrow K^- \pi^+$  decay (left).  $K\pi$  invariant-mass distribution corresponding to  $10^7$  central Pb-Pb events (right); the background-subtracted distribution is shown in the insert. [14]

In combination with the FMD, the ALICE SPD will also contribute to the hadron multiplicity determination. To extend the rapidity coverage of the multiplicity measurement, the first pixel layer has a wider pseudo-rapidity coverage ( $|\eta| \leq 1.98$ ). The FastOr signal of the ALICE SPD will be part of the minimum bias trigger for the proton proton collisions. This will be the first time a large high energy physics experiment uses tracking information from a pixel detector for low level triggering. For a more detailed description of the FastOr signal and the Pixel Trigger (PIT) see chapter 6.5.5.

## Chapter 2

# Semiconductor Particle Detectors

### Contents

---

2.1	Introduction . . . . .	<b>16</b>
2.2	General Principle of Silicon Detectors . . . . .	<b>16</b>
2.2.1	Charge Carrier Generation . . . . .	16
2.2.2	Charge Carrier Transport . . . . .	20
2.2.3	Intrinsic and Doped Silicon . . . . .	22
2.2.4	p-n junction . . . . .	24
2.3	Hybrid Pixel Detectors . . . . .	<b>26</b>
2.3.1	Pixel Detectors at LHC . . . . .	28
2.3.2	Future Pixel Detectors . . . . .	30

---

## 2.1 Introduction

All the LHC experiments employ silicon pixel detectors to provide high granularity tracking as close as possible to the interaction point (IP). The high granularity in pixel detectors tolerate a hit density higher compared to that of microstrip and silicon drift detectors and allow precise measurements of the impact parameters. The high two dimensional spatial resolution (in the order of 10 to 20  $\mu\text{m}$ ) makes them suitable for primary and secondary vertexing.

The radiation levels close to the IP are very high in most LHC experiments. The growth of the leakage current due to radiation damage in the sensitive volume is in many cases the limiting factor for the deployment of the silicon detectors. In comparison to microstrip detectors, the length of the cell in pixel detectors is smaller and accordingly the noise level in each pixel cell caused by shottky noise is smaller. This makes the pixel detectors more suitable for high radiation environments. However, the overall operability of the sensor is limited by current stability. Due to the small cell size, also the capacitance in pixel cells is very low, requiring smaller charge signals for satisfactory signal-to-noise ratios.

In the following chapter, the general principle of pixel detectors is explained and an overview of the pixel detectors used in the LHC HEP-experiments is presented.

## 2.2 General Principle of Silicon Detectors

A silicon crystal has a diamond structure with each atom forming covalent bonds with its four nearest neighbors. In Figure 2.1 a schematic drawing of the covalent bonds and the position of silicon atoms in the crystal is displayed. The energy levels of the electrons are confined in two energy bands (valence and conduction band), where they are closely spaced. The energy states between the valence and the conduction band, called the band-gap  $E_g$ , is forbidden. The size of the band-gap classifies solids in insulators ( $E_g \sim 9 \text{ eV}$ ), semiconductors ( $E_g = 1 - 5 \text{ eV}$ ) and conductors (conduction and valence band overlapping or valence band partially filled).

### 2.2.1 Charge Carrier Generation

The basic idea of a semiconductor detector is that through illumination or irradiation electron-hole pairs are generated in the sensitive volume. This process is called *carrier generation*. Depending on the involved interaction mechanism in the sensitive volume, one distinguishes between the directly and indirectly ionizing radiation. In case of directly ionizing radiation, the incoming charged particle deposits part or all of its energy through direct Coulomb interaction with the orbital electrons in the volume. Neutral particles, such as photons or neutrons, deposit their energy in two steps (indirectly ionizing radiation). By passing through the medium, charged particles, mostly electrons or positrons in case of photon illumination, are generated. The so called secondary particles, transfer their energy to the bulk through direct Coulomb interactions with the orbital electrons.

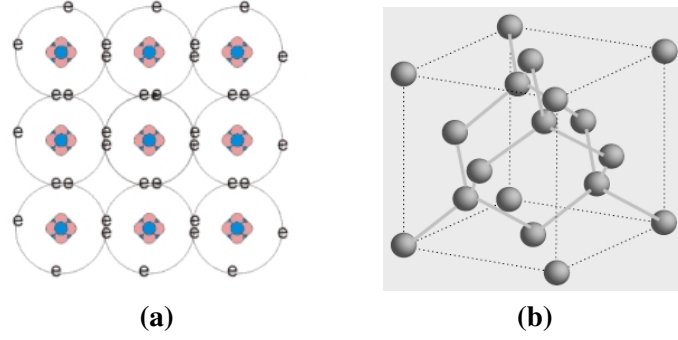


Figure 2.1: (a) Schematic diagram showing the covalent bonds of the silicon atoms to their nearest neighbors. (b) The lattice structure showing the arrangement of the silicon atoms in a unit cell. The lines between silicon atoms in the lattice illustration indicate nearest-neighbor bonds. [15] and [21]

### Photon Interactions

A beam of photons passing through matter will be weakened following an exponential attenuation:

$$I(x) = I_0 \cdot e^{-\mu x} \quad (2.1)$$

with  $I(x)$  being the photon flux intensity at the depth  $x$ ,  $I_0$  the primary intensity and  $\mu$  the attenuation coefficient. The photon beam will lose its energy due to absorption or scattering processes. Depending on the energy of the photon, several interaction mechanisms are possible.

The photoelectric absorption is dominant at low photon energies. The photon will transfer its complete energy to a tightly bound inner shell electron and become completely absorbed. The momentum conservation requires that a bound electron participates in this reaction, since the nucleus absorbs the recoil momentum. The electron will have an energy of  $E = E_{\text{photon}} - E_{\text{bind}}$  given by the difference of the energy of the incoming photon and the binding energy of the electron. In the following scattering processes the photo-electron will lose its energy due to phonon excitation and ionisation.

A photon can also undergo two kind of scattering processes: Compton effect or Rayleigh/Thomson scattering. The Compton effect describes the inelastic scattering of a photon on a free electron. Since the outer shell electrons are only weakly bound, they can be accounted as quasi-free electrons. Figure 2.2 illustrates this process. The scattered photon energy  $h\nu'$  and the energy of the compton-electron  $E'$  depend only on the scattering angle:

$$h\nu' = h\nu \frac{1}{1 + \frac{h\nu}{m_e c^2} (1 - \cos\theta_\gamma)} \quad (2.2)$$

$$E' = h\nu \left( 1 - \frac{1}{1 + \frac{h\nu}{m_e c^2} (1 - \cos\theta_\gamma)} \right) \quad (2.3)$$

where  $m_e c^2$  denotes the rest mass of an electron ( $m_e c^2 = 0.511 \text{ MeV}$ ). The maximum energy can be transferred onto the electron under an angle of  $\theta_\gamma = \pi$  (backscattering of the photon)

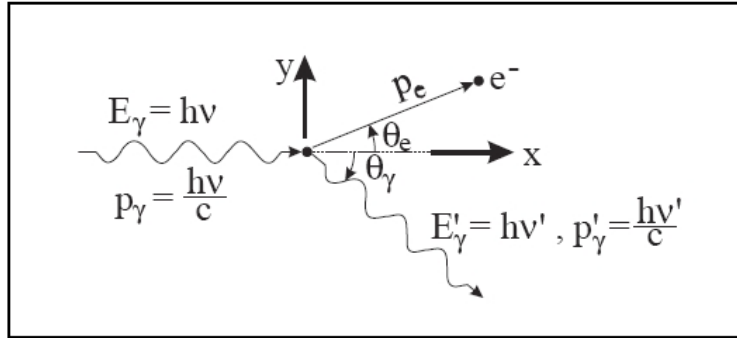


Figure 2.2: The kinematics for Compton scatter [16]

and is also called Compton edge. The transferred energy amounts to:

$$E'_{max} = \frac{2 \frac{(h\nu)^2}{m_e c^2}}{1 + 2 \frac{h\nu}{m_e c^2}} \quad (2.4)$$

The direction of the recoil electron is linked to the photon scattering angle by energy and momentum conservation and is given by:

$$\cos\theta_e = \left(1 + \frac{h\nu}{m_e c^2}\right) \tan \frac{\theta_\gamma}{2} \quad (2.5)$$

In case of the Rayleigh scattering the photon interacts with the whole atom elastically, meaning that the photon does not lose any energy, but changes its direction only. The shell electrons are involved in a coherent form, why this process is often referred to as the coherent scattering. The Thomson scattering is also elastic, but the photon interacts only with one quasi-free shell electron.

High energy photons ( $E_\gamma \geq 1.022 \text{ MeV}$ , which corresponds to two times the electron rest mass) can also decay into an electron-positron pair, which is referred to as pair creation. Due to momentum conservation the pair creation can occur only in the Coulomb field of a scattering partner, which will absorb the recoil.

The total linear attenuation coefficient is given by the sum of the three partial attenuation coefficients:

$$\mu = \tau_{photoelectric} + \sigma_{compton} + \kappa_{pair} \quad (2.6)$$

### Charged Particle Interaction

In contrary to photons or neutrons charged particles traversing matter, interact directly with the medium via the Coulomb interaction. The incoming particles are scattered either on orbital electrons or atomic nuclei. The scattering process can be elastic or inelastic. While in an elastic

collision, the incoming particle changes only its direction, in an inelastic process, the particle will lose some of its energy, too.

Depending on the mechanism of the energy transfer, the inelastic process can be further categorized:

- If the incoming particle interacts with an orbital electron, the result is either an ionisation or an excitation of the electron. This process is described by the so called *collision stopping power*. The energy transferred to the so produced secondary electrons can be sufficient for them to travel significant distances from the primary collision point causing themselves further ionisations. Such high energy secondaries are called delta-rays.
- If the incoming particle interacts inelastically via the Coulomb field of an atomic nucleus, the particle will radiate a part of its energy in form of the Bremsstrahlung. This kind of Coulomb interaction is described by the *radiative stopping power*.

The total mass stopping power  $S$  and with it the loss of kinetic energy  $E_{kin}$  per unit path length can then be described by

$$S_{tot} = S_{coll} + S_{rad} = -\frac{dE_{kin}}{dx} \quad (2.7)$$

Heavy charged particles lose their energy mainly through ionisation and excitation. The energy loss is then given by the mass stopping power and can be calculated with the Bethe-Bloch formula [18]:

$$-\frac{dE}{dx} = 4\pi N_A r_e^2 m_e c^2 z^2 \frac{Z}{A} \frac{1}{\beta^2} \left[ \ln \left( \frac{2m_e c^2 \gamma^2 \beta^2}{I} \right) - \beta^2 - \frac{\delta}{2} \right] \quad (2.8)$$

with

- $z$ : electrical charge of the incoming particle
- $Z, A$ : atomic number and mass of the absorber
- $m_e$ : electron mass  $0.511 \text{ MeV}$
- $r_e$ : classical electron radius
- $N_A$ : Loschmidt (=Avogadro) number =  $6.022 \cdot 10^{23} \text{ Mol}^{-1}$
- $I$ : mean excitation energy ( $173 \text{ eV}$  for silicon)
- $\delta$ : density effect correction to ionizing energy loss ( $6.02$  for silicon)

Due to their comparatively small rest mass, the energy loss caused by incoming electrons and positrons can not be described accurately by Equation 2.8. A more accurate expression suitable for this process can be found in [18].

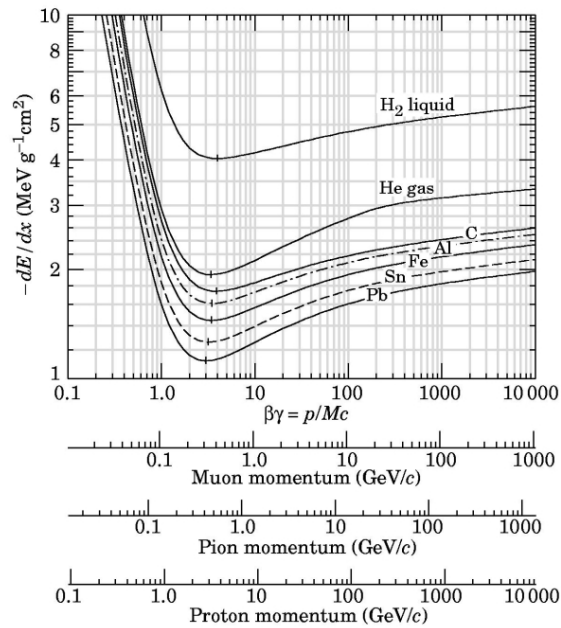


Figure 2.3: Mean energy loss rate in liquid (bubble chamber) hydrogen, gaseous helium, carbon, aluminum, iron, tin and lead. [19]

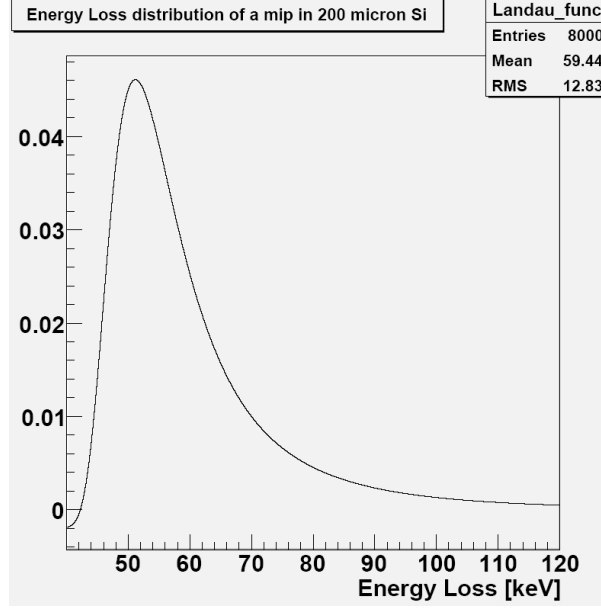
In Figure 2.3 the energy loss in different absorbers is plotted as a function of  $\beta\gamma$ . At  $\beta\gamma \sim 4$  a minimum in the ionisation can be seen. In practical cases most relativistic particles have energy loss rates close to this minimum, and are referred to as minimum ionizing particles (MIP's) [19].

The  $dE/dx$  values from Bethe-Bloch formula are average values. The ionization process for a single particle passing through matter is statistical and as such it underlies fluctuations. Therefore the energy loss of a single particle in matter is best described by a probability distribution. In case of thick absorbers, the energy loss follows the Gaussian distribution and in thin absorbers, the energy loss can be best described with a Landau distribution [17]. The energy loss of a MIP in a  $200 \mu\text{m}$  thick silicon absorber was calculated and can be seen in Figure 2.4. The mean energy loss amounts to  $\sim 60 \text{ keV}$  in  $200 \mu\text{m}$  of silicon. This corresponds to  $\sim 16600$  electron-hole pairs ( $\sim 2.6 \text{ fC}$ ).

## 2.2.2 Charge Carrier Transport

Electron-hole pairs created by a particle passing through a semiconductor will undergo the recombination process. Since this process will take a certain amount of time, the charge carriers will diffuse and if an external field is applied also drift through the semiconductor volume.

The diffusion results out of the carrier concentration gradient. A diffusion current from a region

Figure 2.4: Energy loss distribution of a MIP in 200  $\mu\text{m}$  of silicon.

of high concentration to regions of lower concentration will take place. This diffusion current  $J_{diff}$  is proportional to the spatial derivative of the electron density  $\frac{dn_e}{dx}$  and to the diffusion constant D:

$$J_{diff} = -qD \frac{dn_e}{dx} \quad \text{with} \quad D \propto v_{th} \lambda_C \quad (2.9)$$

with  $\lambda_C$  being the mean free path between two subsequent collisions and  $v_{th}$  the thermal velocity.

If an external electrical field is applied onto the semiconductor volume the charge carriers will be accelerated resulting in an average drift velocity  $v_{e,p}$ . This drift velocity is superimposed to the thermal random motion. Each carrier will experience a force proportional to the electric field  $\vec{E}$  and will gain therefore a momentum  $\pm q\vec{E}\tau_C$  with  $\tau_C$  being the mean free time (relaxation time) between two subsequent collisions. The drift velocity can then be calculated with

$$v_{e,p} = \mp \frac{q\tau_C}{m_{e,p}} \vec{E} = \mp \mu_{e,p} \vec{E} \quad (2.10)$$

allowing to calculate the macroscopic drift current:

$$J_{drift} = (n\mu_e + p\mu_p)q\vec{E} = \sigma\vec{E} \quad (2.11)$$

where  $\sigma$  is the material conductivity. At higher electrical fields the scattering process of the charge carriers due to impurities and lattice vibrations does not allow a constant increase in the drift velocity. The velocity saturates at high electric fields reaching the saturation velocity of

$$v_s = \sqrt{\frac{E_{op}}{m_*}} \quad (2.12)$$

with  $E_{op}$  being the optical phonon energy and  $m^*$  the effective carrier mass. The drift velocity in silicon saturates at approx.  $5 \cdot 10^5$  V/cm.

Mobility and diffusion can be correlated to each other via the *Einstein relation*:

$$D = \left( \frac{kT}{q} \right) \mu_e \quad (2.13)$$

### 2.2.3 Intrinsic and Doped Silicon

In an ideal silicon crystal at 0 K, all electrons are in the valance band filling it up to the Fermi-level and leaving the conduction band completely free. At room temperature, the conduction band is partly filled due to thermal excitation. The band-gap amounts to 1.12 eV at room temperature [20]. A transition of an electron from the valance band to the conduction band requires a minimum energy of about three times larger than  $E_g$ . An average energy of 3.6 eV is needed where about two third of it is used for exciting lattice vibrations.

Using the Fermi-Dirac distribution function

$$F(E) = \frac{1}{1 + \exp[(E - E_F)/kT]} \quad (2.14)$$

the electron density in the conduction band  $n$  and the hole density in the valance band  $p$  can be calculated:

$$n = N_C \exp\left(-\frac{E_C - E_F}{kT}\right) \quad \text{with} \quad N_C = 2 \left( \frac{2\pi m_e^* kT}{h^2} \right)^{3/2} \quad (2.15)$$

$$p = N_V \exp\left(-\frac{E_F - E_V}{kT}\right) \quad \text{with} \quad N_V = 2 \left( \frac{2\pi m_p^* kT}{h^2} \right)^{3/2} \quad (2.16)$$

where  $N_C$ ,  $N_V$  denotes the effective density of states at the conduction and valance edge ( $N_C = 2.8 \cdot 10^{19} \text{ cm}^{-3}$  for silicon [20]),  $E_F$  the Fermi energy,  $E_C$  the energy of the bottom of the conduction band,  $E_V$  the energy of the top of the valance band and  $m_{e,p}$  the effective mas of the electrons and holes<sup>1</sup>.

In intrinsic semiconductors, the electron density is equal to the hole density allowing the calculation of the intrinsic carrier concentration  $n_i$

$$np = n_i^2 = N_C N_V \exp\left(\frac{E_g}{kT}\right) \quad (2.17)$$

with the band gap energy  $E_g \equiv E_C - E_V$ . One can see that the carrier concentration does not depend on the Fermi level, but is only determined by the intrinsic properties of the semiconductor, the width of the band gap and the temperature. For silicon at room temperature, the intrinsic concentration is in the range of  $10^{10} \text{ cm}^{-3}$ . Keeping in mind that the intrinsic concentration of

<sup>1</sup>indirectly proportional to the curvature of the corresponding conduction and valance band

metals is in the order of about  $10^{21} \text{ cm}^{-3}$ , the number of free charge carriers in silicon is very small.

In order to increase the number of the free charge carriers in the silicon bulk, spacial impurities can be added. This is referred to as extrinsic semiconductors. The lattice atoms are replaced by a foreign atom, which form covalent bonds with their neighbors in the bulk. This is done by adding to the silicon bulk atoms which have one electron more or less in the outer electron shell than silicon.

Doping with the elements from the group V of the periodic table of elements, such as phosphorus, an extra electron is added. This creates an additional allowed energy level in the band gap close to the conduction band and moves the fermi level closer to the conduction band edge. This way the probability to populate the conduction band increases and thus, the number of the electrons in the conduction band rises. The silicon becomes *n-type* due to the surplus of negative charge carriers. Impurity atoms with an extra electron in the outer shell are referred to as *donors*.

Similarly, if the impurities to the silicon bulk have been introduced by adding elements from the group III, such as boron, the hole density in the valence band is increased and the silicon becomes p-type. In this case, the impurity atoms are referred to as *acceptors*. The doping of semiconductors is illustrated in Figure 2.5. The resistivity of the semiconductor  $\rho$  is related to

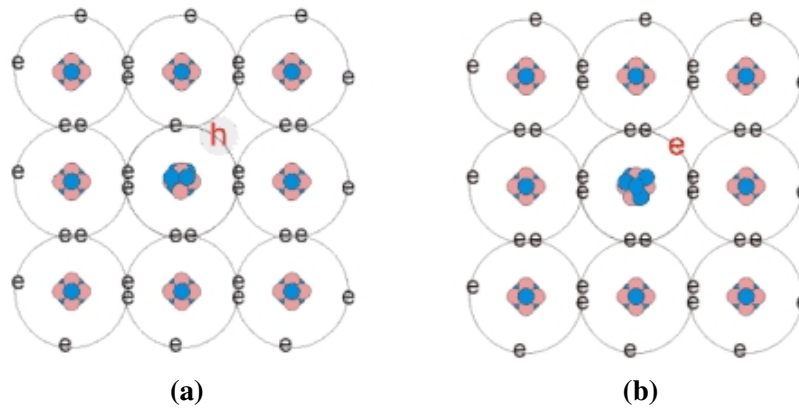


Figure 2.5: Schematic diagram showing only the valence electron shell to illustrate p-type (a) and n-type (b) semiconductors. [15]

the concentration of free charge carriers via the following Equation:

$$\rho = \frac{1}{q(\mu_e n + \mu_h p)} \quad (2.18)$$

where  $\mu_e, \mu_h$  are the mobility of electrons and holes and  $q$  the elementary charge. Intrinsic silicon has a resistivity of about  $235 \text{ k}\Omega\text{cm}$ , while for an n-type silicon the resistivity varies from 4 to  $6 \text{ k}\Omega\text{cm}$ .

### 2.2.4 p-n junction

For efficient detecting of particle passing through a silicon detector, the recombination of created charge carriers should be avoided. Also, the volume should be free of other charge carriers. This can be reached by using a p-n junction, where a n-type and a p-type silicon are brought into contact. Due to charge carrier concentration gradients at the junction the electrons will diffuse into the p-material and holes into the n-material recombining with their counterparts to form a charge free volume. This causes a surplus of negative charge carriers in the p-type side of the junction and the positive donor ions in the n-type side. As a result an electrical field over the junction occurs which counteracts and eventually stops the diffusion of the charge carriers. The corresponding potential is called built-in voltage and is given by

$$V_{bi} = \frac{kT}{q} \ln \frac{N_A N_D}{n_i^2} \quad (2.19)$$

with  $N_A$  and  $N_D$  as the acceptor resp. the donor density. The charge carrier free volume is referred to as depletion region and the width of the extension of this region into the p and n-type silicon can be expressed as a function of the potential difference at the junction:

$$w_p = \sqrt{\frac{2\epsilon_S V_{bi}}{q N_A (1 + \frac{N_A}{N_D})}} \quad (2.20)$$

$$w_n = \sqrt{\frac{2\epsilon_S V_{bi}}{q N_D (1 + \frac{N_D}{N_A})}} \quad (2.21)$$

The depletion region does not have to be symmetric around the junction. As it can be seen in Equations 2.20 and 2.21 it extends further into the lighter doped side. To ensure a continuous transition of energy bands across the junction, the band structure must be bent. In Figure 2.6 the junction and the energy band model of the junction are displayed.

The above described p-n junction does not provide a sufficient wide depletion region nor a strong enough intrinsic field for charge collection. This can be improved by applying an external reverse bias voltage  $V_{bias}$  of the same polarity as  $V_{bi}$  on the p-n diode. The total potential is increased and the depletion region increases. If the voltage applied is negative with respect to  $V_{bi}$  the diode is forward biased and the depletion region decreases according to Figure 2.7.

For the most common particle detectors the junction is formed between a thin highly doped p-layer and an n-doped bulk. Due to Equation 2.21 the thickness of the depletion layer is inversely proportional to the donor density and thus the depletion region extends much further into the n-bulk than into the p-type layer. Due to this the depletion width can be approximated by  $W$  and can be expressed for an external bias voltage to be

$$W = \sqrt{\frac{2\epsilon_S (V_{bias} + V_{bi})}{q N_D}} \quad (2.22)$$

The detector is fully depleted when the external voltage exceeds the *fully depletion voltage*  $V_{dep}$

$$V_{dep} = \frac{q}{2\epsilon_S} n_{eff} d^2 \quad (2.23)$$

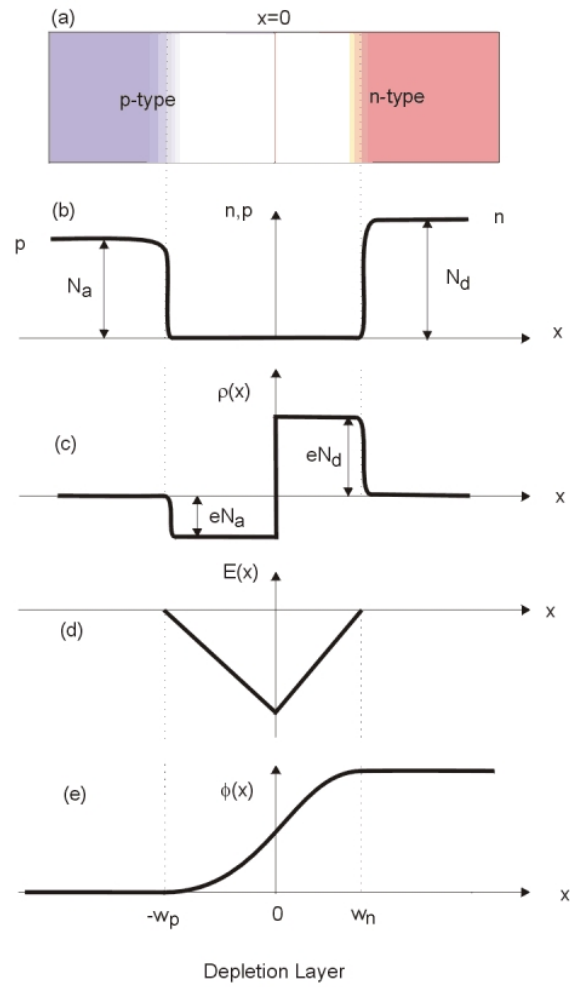


Figure 2.6: Schematic sketch of a p-n junction and its energy levels. (a) Abrupt p-n junction. (b) Concentration holes and electrons. (c) Space charge distributions and depletion region formed by the junction. (d) Electric field distribution. (e) Energy band diagram across the junction. [15]

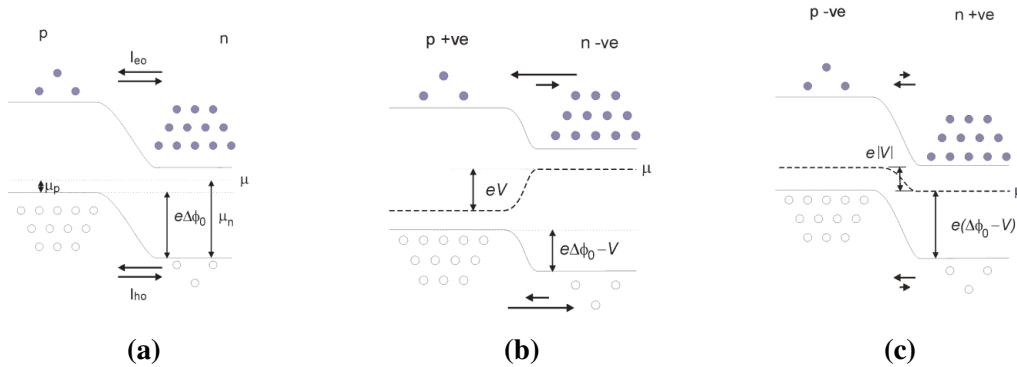


Figure 2.7: Schematic illustration of the effects of the bias voltage on the p-n junction: (a) no bias voltage; (b) forward bias and (c) reverse bias. [15]

where  $n_{eff}$  denotes the effective doping concentration and  $d$  the width of the detector active volume.

## 2.3 Hybrid Pixel Detectors

The general principle of the hybrid pixel detectors is to process the sensor pixel diodes and the readout electronics on different substrates. This way the sensor and the electronics can be optimised independently from each other. The sensor is a high resistivity silicon segmented in both directions to form a matrix. The charge carriers collected in the sensor volume are passed to the readout cells via the so called bump-bonds (see chapter 3.2.4).

The pixel cells on the readout substrate have the same size as the detector elements. Each readout cell accommodates analog and digital circuitry. The minimum pixel cell size is limited by the necessary surface for the readout electronics and the bump-bonds. Figures 2.8 and 2.9 illustrate the general principle of hybrid pixel detectors.

The electron-hole pairs generated in the silicon sensor will drift to the electrodes under the effect of the electric field present in the detector volume. The drift current in the detector induces a signal at the electrodes on the detector faces. The signal is a small and fast current pulse. It is too small to be transmitted over long distances and needs therefore to be amplified. With an amplifier and a shaper as the first elements in the readout cell the signal is increased and converted to a voltage pulse. Figure 2.10 illustrates this process.

The signal after the shaper is a continuous function with infinite number of points. While this analog information is exact and no loss of information occurred at this stage, the transfer of analog signals would result in huge amount of data. In order to reduce the amount of data, the signal can be converted to digital output. There are two possibilities to do so:

- **Binary readout:** A discriminator compares the amplitude with a set threshold value and

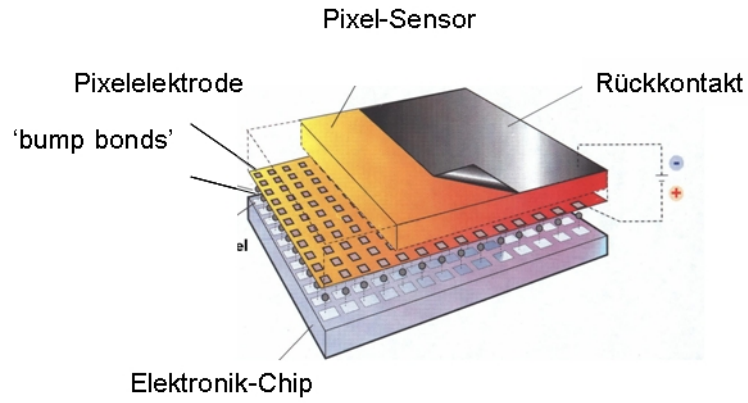


Figure 2.8: Schematic of a hybrid pixel detector with the sensor chip and the electronics chip connected with bump-bonds. [22]

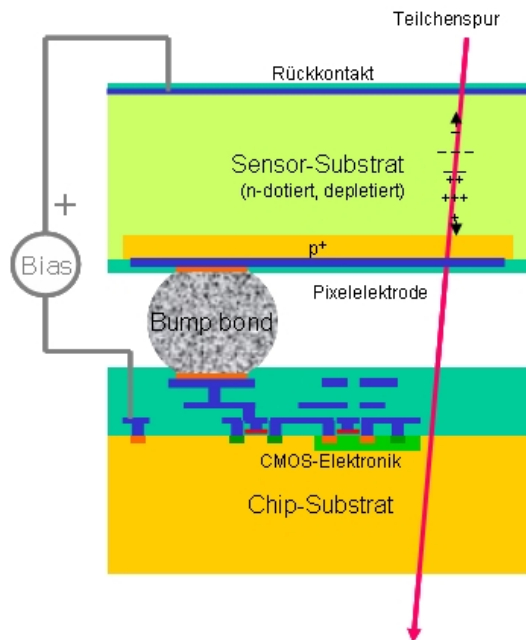


Figure 2.9: Schematic showing the principle of a pixel hybrid detector.

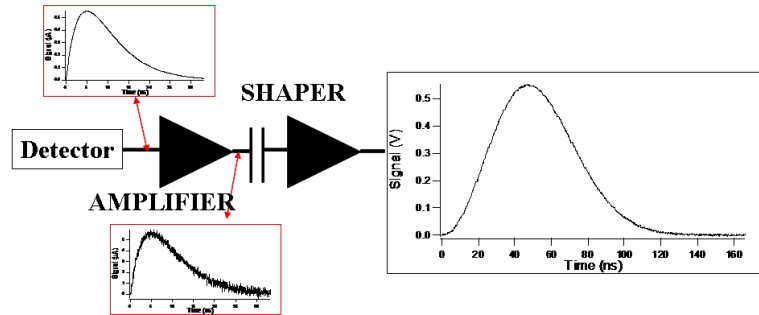


Figure 2.10: Schematic illustration of the signal amplification within the pixel cell. [23]

writes a logical 1 (hit) for a signal above and a logical 0 (no hit) for a signal below the threshold. This readout is simple and fast and only small amount of data needs to be transferred off the chip. However, the information from the hit is suppressed and threshold scans are needed to access the analog quantities of the chip (noise, threshold variations). The ATLAS and ALICE collaborations have chosen this kind of readout for their pixel detectors.

- **ADC readout:** An Analog to Digital Converter (ADC) is used to present the amplitude. The higher the number of bins in the ADC, the smaller the loss of information. The data is now digitized and therefore more robust for transfer, but the amount of data is still large.

### 2.3.1 Pixel Detectors at LHC

An important factor in the use of hybrid pixel detectors is the radiation tolerance. During the LHC program the radiation exposure of the inner layers of CMS and ATLAS is expected to be as high as 500 kGy resp.  $10^{15}$  n<sub>eq</sub>/cm<sup>2</sup>. This will have direct influence on the threshold voltages in the transistors and leakage current. Also, radiation induced bit errors, so called Single Event Upsets (SEU), will cause errors in the data stream. Applying deep submicron 0.25  $\mu$ m CMOS technologies, thinner oxide layers, enclosed gate electrodes, guard rings and redundant buffers in the readout electronics will make the electronics more radiation tolerant. [24]

Due to the bunch crossing time of 25 ns, the pixel detectors of ATLAS and CMS will employ parallel signal processing with 40 MHz for about  $\sim 10^8$  channels. The readout speed for the ALICE pixel detector will be 10 MHz due to a different bunch crossing rate in the heavy ion runs.

The Atlas pixel detector will use the ATLAS FE-13 readout chip. The chip is built in th 0.25  $\mu$ m CMOS technology with radiation tolerant design rules (annular NMOS transistors, guard rings, etc.). The pixel cell has a dimension of 450  $\mu$ m x 50  $\mu$ m arranged in 18 columns and 160 rows. The sensor is an n<sup>+</sup> in n substrate. 16 readout chips are flip-chip bonded <sup>2</sup> to a 2 x 7

<sup>2</sup>A detailed explanation of the flip-chip process can be found in the chapter 3

$\text{cm}^2$  Si-sensor. In total  $80 \times 10^6$  channels will cover a surface of about  $2 \text{ m}^2$ . The detectors will be placed as the first ATLAS layers in 3 barrels and  $2 \times 3$  disks around the beam pipe. Figure 2.11 shows the schematic setup of the ATLAS pixel system and a picture of the ATLAS pixel modules. [25]

The ATLAS FE-13 chip is readout binary with additional indirect information about the signal amplitude by measuring the pulse width of the comparator signal (ToT - Time over Threshold measurement). Each readout cell has around 700 transistors resulting in 3.5 millions transistors per chip. 8-bit and 10-bit segmented DACs provide  $\checkmark$ in-chip $\checkmark$  generation of bias (and calibration) voltages. After zero suppression the data is transferred to off-detector electronics. In order to achieve low noise levels, the threshold needs to be adapted individually for each pixel cell. The noise and threshold-variation amount to  $\sim 600 e^-$  at a threshold level of approx.  $3000 e^-$ . The time resolution is better than 20 ns for all signal amplitudes. The hit information can be buffered up to  $2.5 \mu\text{s}$ , waiting for the L1 trigger decision for hit selection.

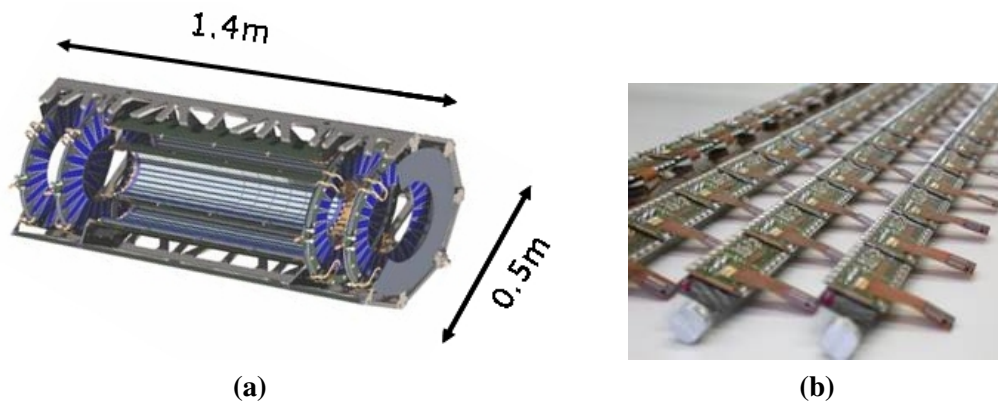


Figure 2.11: The ATLAS silicon pixel detector. [25]

The barrel module of the CMS pixel detector contains  $2 \times 8$  PSI46 V2.1 readout chips flip-chip bonded to a silicon pixel-sensor. Each readout chip will have pixel cells arranged in 52 columns and 80 rows. One pixel cell measures  $150 \mu\text{m}$  in the  $r\phi$ - and  $150 \mu\text{m}$  in the  $z$ -direction. The CMS pixel system will have two barrel layers built of about 800 modules in total and  $2 \times 2$  disk layers. In total  $33 \times 10^6$  channels will cover a surface of around  $2 \text{ m}^2$ . In Figure 2.12 a schematic illustration of the CMS pixel setup and a picture of the CMS disk modules is shown. [26]

The PSI46 V2.1 chip has an analog readout. The functional blocks are similar as for the binary readout of the ATLAS FE-13 chip. Additionally the chip contains buffers for the analog amplitude information. Due to analog readout the PSI46 V2.1 chip must deal with an enormous data rate. After zero suppression, the hit data must be buffered locally during the latency of the first level trigger. In order to keep the dead time of the detector low, a fast analog link is used. The analog output signal contains the pulse amplitude and column and row address coded in 6 analog levels. The signal is then transmitted electrically to the detector supply tube.

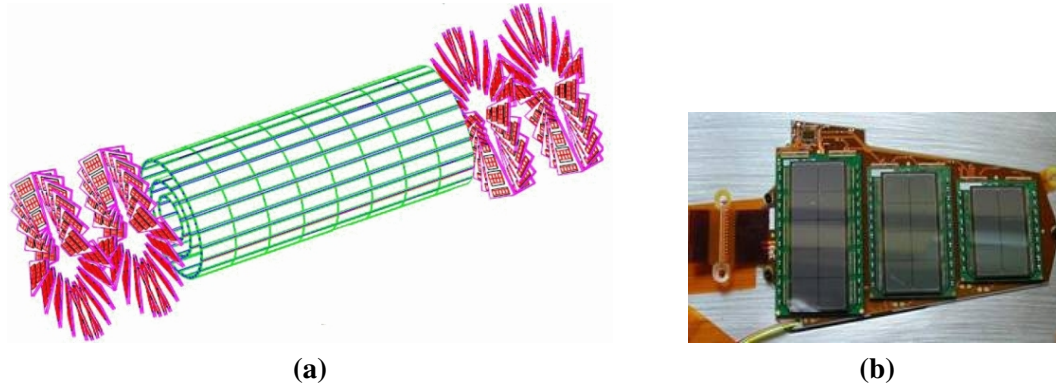


Figure 2.12: The CMS silicon pixel detector. [26]

In LHCb no silicon pixel detectors are used as vertex detectors, but similar readout chips as in ALICE provide the readout of the RICH subdetector. The ALICE SPD system will be explained in chapter 3.

### 2.3.2 Future Pixel Detectors

For the next generation accelerator, the ILC, the hybrid pixel detectors will not be adequate. In order to achieve the required spatial resolutions of a few  $\mu\text{m}$  the pixel cell sizes will have to be reduced to less than  $25 \times 25 \mu\text{m}^2$ . The material budget of around 0.1% will be a constraint, which the pixel hybrid detectors will not be able to fulfill. Therefore, the community is already working on novel detector technologies. In the following section, two of these new technologies will be briefly introduced.

In the so called Monolithic Active Pixel Sensors (MAPS) a thin epitaxial layer of low-resistivity silicon is used as a sensitive detector volume. The signal processing (amplification, noise subtraction, discrimination, digitization, etc.) is integrated on the detector substrate, which can be thinned to a few tens of  $\mu\text{m}$ . The charge generated in a few  $\mu\text{m}$  thin p-epitaxial-layer underneath the readout electronics is collected in an n-well through diffusion. At a rate of about 80 e-h pairs per  $\mu\text{m}$ , small signals in the range of  $\leq 1000 e^-$  are created by a charged particle. Due to small capacitances, the noise level is low allowing a signal to noise ratio in the order of 20 to 30. Very small pixel sizes ( $\leq 20 \times 20 \mu\text{m}^2$ ) and thus very good resolution ( $\sim 1.5 \mu\text{m}$ ) can be realized. Radiation hardness (not yet radiation hard beyond  $10^{13} \text{ n}_{\text{eq}}/\text{cm}^2$ ) and readout speed remain to be substantially improved before they match the demands of the future accelerators. [27] Figure 2.13 illustrates the working principle of MAPS and the achievable resolutions. Due to monolithic design, no interconnection to electronics, e.g bump-bonds, is needed. No depletion voltage is applied, but the potential is formed by different doping concentrations only.

The DEpleted Field Effect Transistor (DEPFET) combines particle detection and signal amplification jointly by integrating a field effect transistor into a fully depleted bulk. The silicon

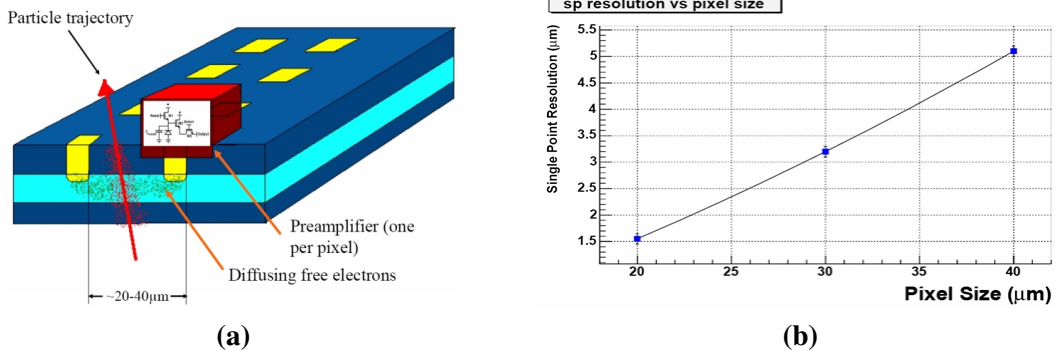


Figure 2.13: (a) Schematic of the working principle of the MAPS. (b) The resolution as a function of the pixel size. [28]

bulk is depleted by means of sideways depletion forming a potential minimum for electrons at the internal gate below the transistor, where all signal charges are collected. The potential of the internal gate and thus the transistor current is modulated by the collected charge. The amplification of charge occurs at the position of collection and due to the very low capacitance of the internal gate low noise operation ( $\leq 3 e^-$ ) can be obtained. With the charge generation in the complete thickness of the sensor very large signal to noise ratios can be achieved. Figure 2.14 explains schematically the working principle of the DEPFET and shows the achievable signal to noise ratio with a  $^{55}\text{Fe}$  spectrum taken with a linear DEPFET structure at room temperature with a  $10 \mu\text{s}$  shaping time. The general readout structure is similar to that of a CCD and therefore relatively slow.

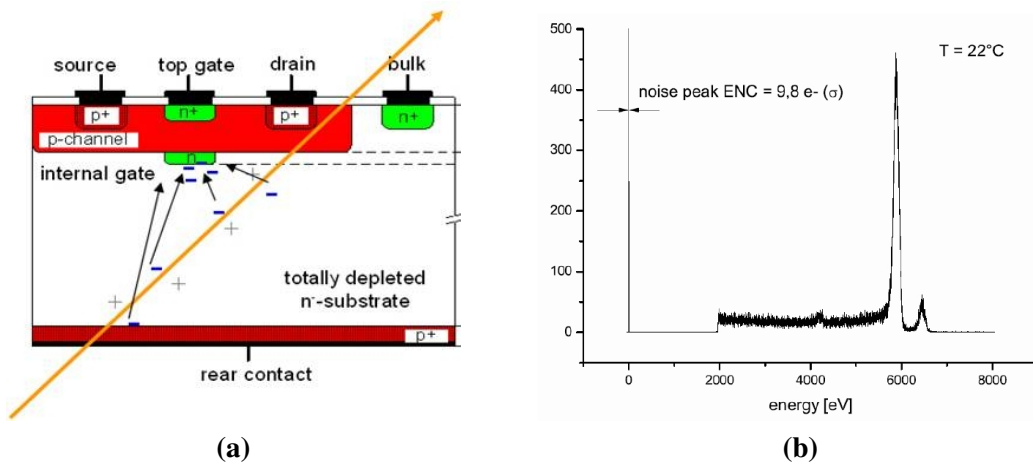


Figure 2.14: (a) Schematic of the working principle of DEPFET. (b)  $^{55}\text{Fe}$  spectrum taken with a linear DEPFET structure at room temperature with a  $10 \mu\text{s}$  shaping time. [29]

The pixel detectors allow a complex signal processing already at the level of the pixel cells. Zero suppression makes data reduction possible and buffers can store the hit events during the

L1 trigger latency. Through special design of the readout cells and the sensor volume high radiation tolerance can be achieved. And due to charge sharing and the small pixel dimensions the spatial resolution can be as small as  $10\ \mu\text{m}$ . The disadvantage of the pixel detectors is the high material budget and therefore the increased radiation length  $X_0$ . Due to services, cooling and the readout substrate the material budget amounts to  $2\%$   $X_0$  per layer for CMS and ATLAS and  $1\%$   $X_0$  for ALICE. Further, the flip-chip interconnection process causes an additional production complication, which can reduce the production yield. Many testing steps during the production process are therefore necessary.

Future HEP Experiments will make even more intensive use of silicon pixel detectors. The new generations of pixel detectors will have to be operated in higher radiation environment and at the same time have to cope with even more stringent material budget constraints than in the LHC environment. These new pixel detector concepts are still in their early development phases but offer new, promising possibilities once large production is mastered.

## Chapter 3

# The ALICE Silicon Pixel Detector (SPD)

### Contents

---

3.1	Introduction . . . . .	<b>34</b>
3.2	Components of the ALICE SPD . . . . .	<b>34</b>
3.2.1	The Readout Chip . . . . .	35
3.2.2	The Pixel Cell . . . . .	36
3.2.3	SPD Sensor . . . . .	38
3.2.4	Flip Chip Bonding of the SPD Ladders . . . . .	39
3.2.5	Front-end and Readout Electronics . . . . .	42
3.2.6	Half-Stave and Sector Assembly . . . . .	45
3.3	ALICE SPD Test Setup . . . . .	<b>50</b>
3.3.1	Readout Chain Architecture . . . . .	50
3.3.2	Test System Software . . . . .	51
3.4	Summary . . . . .	<b>52</b>

---

### 3.1 Introduction

The ALICE Silicon Pixel Detector (SPD) consists of two barrel layers (see Figure 3.1) of silicon hybrid detectors at radii 3.9 cm and 7.6 cm. It will cover the central region in the pseudorapidity range  $|\eta| \leq 1.98$  and  $|\eta| \leq 1.31$  respectively.

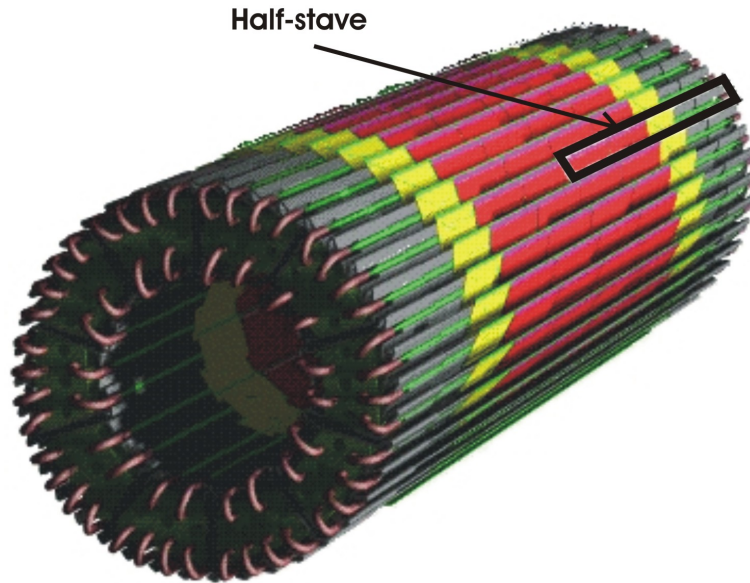


Figure 3.1: Schematic view of the two barrel layers of the ALICE SPD. [30]

The ALICE SPD is designed to provide precise position determination in the high track density environment in the region close to the interaction point. Together with the other two detector systems of the ITS a primary vertex resolution below  $100 \mu\text{m}$  can be reached. The pixel detector resolution in the  $r\phi$ -direction amounts to around  $12 \mu\text{m}$ . The SPD will contribute to the secondary vertexing and thus, to the detection of decays of strange, charm and beauty hadrons. In heavy ion collisions, the expected multiplicity per unit of rapidity amounts up to 8000. The ALICE SPD will operate in a relatively high radiation environment.

In the following chapter, the architecture and the individual components of the ALICE SPD are explained.

### 3.2 Components of the ALICE SPD

The SPD comprises  $9.8 \times 10^6$  pixel cells of dimensions  $50 \mu\text{m}$  ( $r\phi$ )  $\times$   $425 \mu\text{m}$  ( $z$ ) in 1,200 readout chips each containing a matrix of 8,192 pixels. The ALICE SPD has a total area of  $0.24 \text{ m}^2$ . Five readout chips are flip chip bonded to one silicon sensor forming one ladder, which is the basic building block of the ALICE SPD. In Figure 3.2 a picture of one ladder is shown. Two ladders are wire bonded to a flexible multilayer Al-kapton-bus and a Multi

Chip Module (MCM) to form a half-stave. The half-staves are mounted on a special developed Carbon Fiber Support Sector (CFSS) [31]. The CFSS has a thickness of  $200\ \mu\text{m}$  and is divided into 10 sectors forming the two barrel layers. In Figure 3.3 the schematic form of two sectors is shown. The CFSS has cooling tubes embedded in each sector.



Figure 3.2: Picture of one ALICE SPD ladder. 5 ALICE1LHCB readout chips flip-chip bonded to one silicon sensor are visible. The silicon sensor has full aluminum back-side metalization (see chapter 3.2.2)

The half-staves will be symmetrically arranged on the support structure with respect to the beam interaction point, i.e. 60 half-staves will be oriented to the right and 60 to the left (See Figure 3.1). Per sector, the inner layer will host 4 half-staves in the staggered mounting and the outer layer 8 in the windmill configuration (see Figure 3.3).

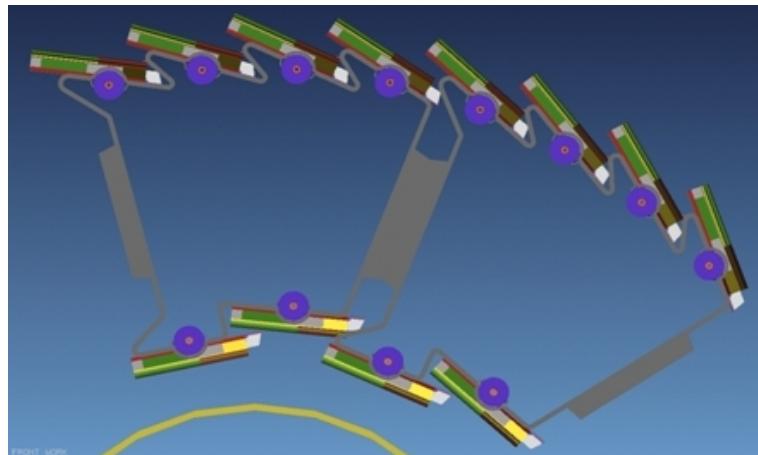


Figure 3.3: The schematic cross-section view of two sectors with the cooling tubes. Each side of the sector, hosts two half-staves on the inner layer in staggered mounting and four half-staves in windmill configuration on the outer layer. [31]

### 3.2.1 The Readout Chip

The ALICE1LHCB chip is fabricated in a commercial  $0.25\ \mu\text{m}$  CMOS process. This makes a high component density possible as well as the implementation of guard rings to prevent Single Event Latch-Up (SEL) [32]. The chips are produced on a  $200\ \text{mm} / 8\ \text{inch}$  silicon wafer with a thickness of  $725\ \mu\text{m}$ . In order to comply with the material budget requirements, the wafer is

thinned down to  $150\ \mu\text{m}$  after bump bond deposition. Figure 3.4 shows a picture of one readout wafer. 86 ALICE1LHCB readout chips are produced on one wafer.



Figure 3.4: Picture of one readout wafer containing 86 ALICE1LHCB readout chips.

The ALICE1LHCB readout chip is designed in dual mode architecture. Besides its application in ALICE SPD, it was also intended to use the chip for the readout of the RICH detector in LHCb. Each pixel cell will operate individually in ALICE mode, while 8 pixels (effective size  $425\ \mu\text{m} \times 400\ \mu\text{m}$ ) would have been grouped together in LHCb mode.

The chip is operated with a 1.8 V power supply and the power consumption per chip amounts to  $\sim 800\ \text{mW}$ . The total area of the chip is  $13.5\ \text{mm} \times 15.8\ \text{mm}$  [33] containing a matrix of 8192 pixel cells of  $425\ \mu\text{m} \times 50\ \mu\text{m}$  in the sensitive area and the internal DACs, the JTAG controller, the testing circuits and the contact pads in the chip periphery (see Figure 3.5). The pixel cells are arranged in 32 columns and 256 rows.

### 3.2.2 The Pixel Cell

The pixel cell is divided into an analog part and a digital part, as shown schematically in Figure 3.6. The analog part consists of a pre-amplifier and two shapers [34]. Both elements are differential elements, with detector signal on one line and a clean reference on the second. This is in order to minimize the digital switching noise. The shaping units tune the peaking time to 25 ns and are reducing the noise. The output of the second shaper is compared to the across the chip globally adjusted threshold by a discriminator. The output of the discriminator is first synchronized to the clock and then fed into the digital part of the pixel cell circuitry.

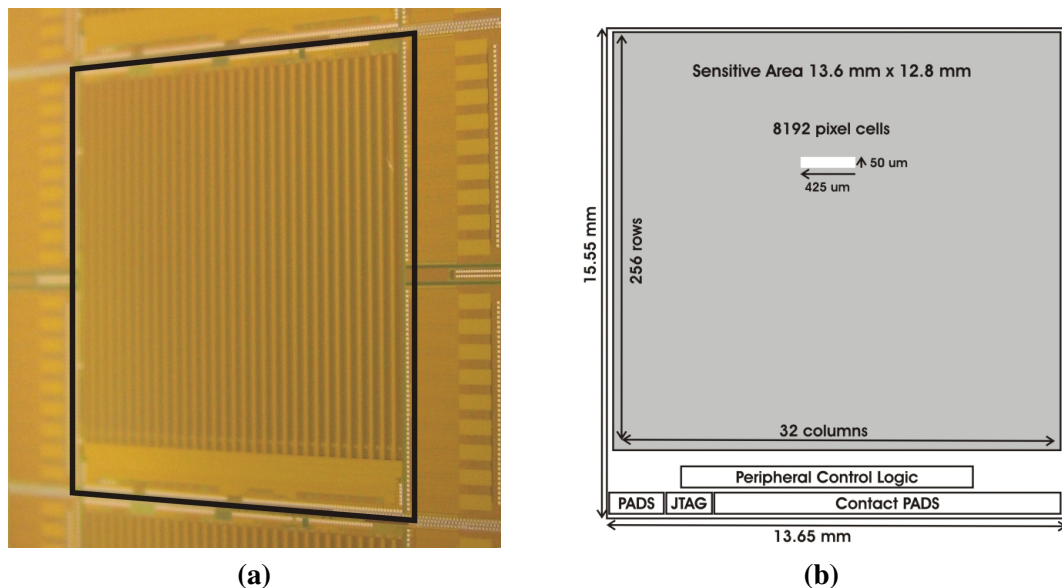


Figure 3.5: Picture (a) and the schematic floor plan (b) of the ALICE1LHCB chip.

The output of the discriminator also generates the FastOr signal in the pixel matrix, which can be used for self-triggering and is in discussion as a part of the L0-trigger of ALICE in proton-proton-collisions (see chapter 6.4.5). The signal coming out of the discriminator can be masked using a mask bit, allowing a deactivation of noisy pixel cells. A test pulse can be injected into the pre-amplifier and is controlled by a logic pulse generated externally. This makes a global threshold scan of the pixel matrix possible and is used in the production tests (see chapter 4). The global threshold can be set externally using an 8-bit threshold adjust and inside every pixel cell, the threshold can be fine tuned with three threshold adjust bits. Due to small threshold variation across the pixel matrix ( $\sim 300$  electrons), the fine-tuning of the threshold is not used in ALICE.

The digital part of the pixel cell consists of two delay units, each consisting of an 8-bit latch. The purpose of the delay units is to store a hit for the duration of the trigger latency. Whenever the first level trigger and the strobe are in coincidence a logical one is written into the next available cell of a 4-event First-In First Out unit (FIFO). Readout is initiated on arrival of the second level trigger YES signal.

### Periphery of the ALICE1LHCB readout chip

On the periphery of the ALICE1LHCB chip close to the I/O pads for the contacts of the wire bonds, 42 8-bit digital analog converters (DAC) are located (see refFloorplan(b)). DACs provide globally the voltage and current references to the analog front-end and the currents starved logic of each pixel cell. The DACs as well as the pixel matrix are controlled via the serial interface following the IEEE JTAG standard [35]. It allows both to write and read of the configuration

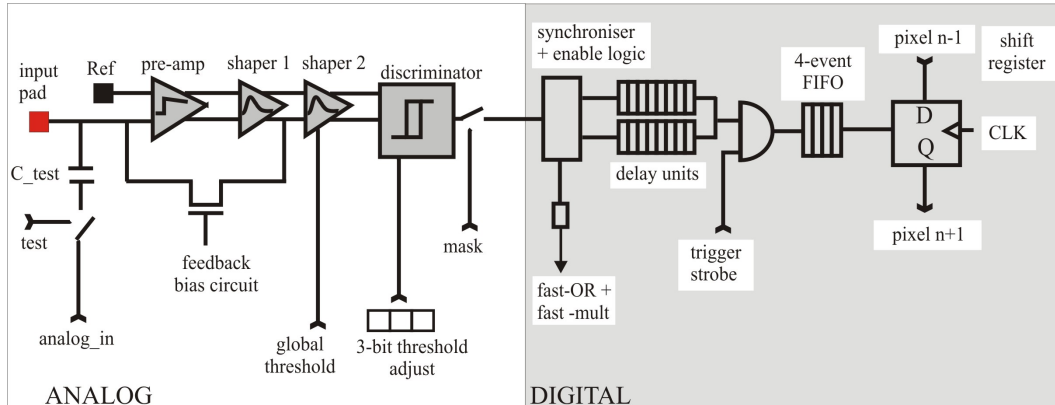


Figure 3.6: Pixel ASIC cell schematic (analog + digital) [34]

settings in the readout chip, including the test, mask and threshold-adjust of each pixel, as well as reading back of the analog levels generated by the digital-to-analog converters via an additional output line [34].

Due to the small width of the ALICE SPD half-staves, the lines available for signals are limited. Therefore, a single-ended standard has been adopted [36]. Gunning Transceiver Logic (GTL) [37] is used for all digital signals to and from the readout chip.

### 3.2.3 SPD Sensor

The ALICE SPD sensor is a p-in-n sensor and has an active size of 70.7 mm x 12.8 mm. The sensor contains a pixel matrix of 5 x (32 x 256) pixel cells (see Figure 3.7 (a)) to which 5 ALICE1LHCB readout chips are flip-chip bonded [38]. The pixel cells at the junction between two readout chips are elongated to 625  $\mu\text{m}$  to ensure coverage in the boundary region. The sensors are produced on 5 inch high resistivity n-type silicon wafers by CANBERRA<sup>1</sup>. The wafer has a thickness of 200  $\mu\text{m}$  to comply with the material budget constraints. In Figure 3.7 (b) the schematic view of the silicon wafer is shown. Each wafer contains 5 silicon sensors for ALICE SPD ladders and 13 single sensors, which could be used for ALICE SPD prototype detectors.

The diode, shown in Figure 3.8, is located on the front-side of the silicon sensor. The p<sup>+</sup>-implant is created through ion implantation. This allows a good control of the junction depth. The number of doped atoms amounts to  $\sim 10^{14}/\text{cm}^3$ , while the n-type silicon bulk has a doping in the order of  $10^{12}/\text{cm}^3$ . The implant is 20  $\mu\text{m}$  wide leaving 15  $\mu\text{m}$  to the cell boundary uncovered. An aluminum layer covers the p<sup>+</sup>-implant and overlaps it by 5  $\mu\text{m}$ . The edges of the implant and the Al-layer are rounded in order to avoid high electric fields. A SiO<sub>2</sub> passivation layer is deposited as a protection layer. The passivation layer covers continuously the complete Si-sensor except the openings with a diameter of 20  $\mu\text{m}$  in each pixel cell for the bump bond

<sup>1</sup>CANBERRA Semiconductor, B-2250 Olen, Belgium

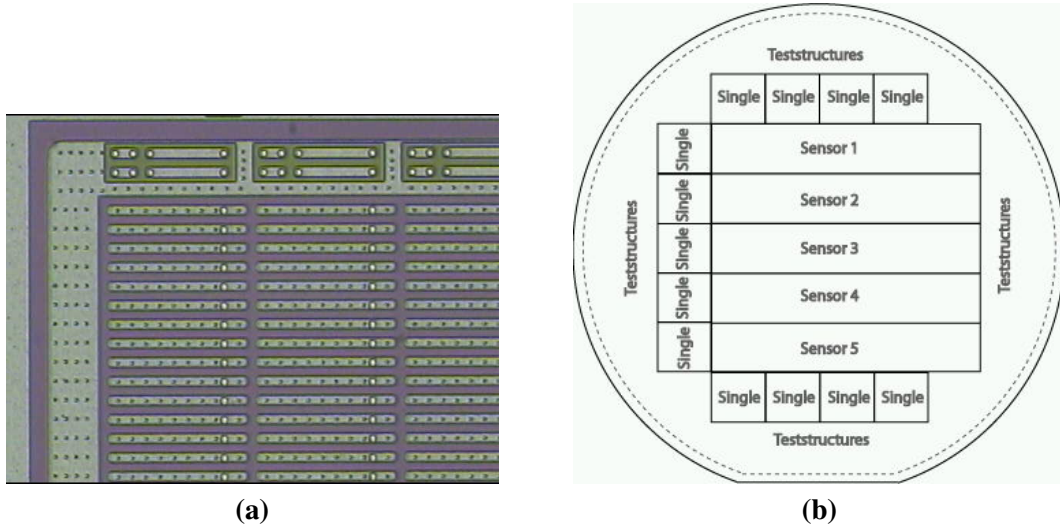


Figure 3.7: Picture of the front-side of the silicon sensor (a). Al-bump bonding pads and vias between Al and p<sup>+</sup>-implant are visible in each pixel cell. Schematic view of the silicon wafers (b).

contacts. Further, each pixel cell has 9 Al-vias from the p<sup>+</sup>-implant to the metalization layer through the thin oxide layer in order to ensure a better field homogeneity. On the back-side of the sensor, a thin n<sup>+</sup>-implant is created on which a layer of aluminum is deposited. The n<sup>+</sup>-layer serves as an ohmic contact between the aluminum and the substrate. Via the Al-layer bias voltage is provided to the Si-sensor. Technical details of the processing carried out by CANBERRA are shown in Table 3.1.

p <sup>+</sup> -implant: ND - NA	$\sim 10^{14}/\text{cm}^3$
n <sup>+</sup> -implant: ND - NA	$\sim 10^{12}/\text{cm}^3$
Wafer thickness	200 $\mu\text{m}$
Wafer diameter	120 mm

Table 3.1: Properties of CANBERRA processing for ALICE SPD silicon sensors [39].

### 3.2.4 Flip Chip Bonding of the SPD Ladders

A more detailed description of the flip-chip process can be found in [41]. One ALICE SPD silicon sensor is flip chip bonded to 5 ALICE1LHCB readout chips using Pb-Sn bump bonds. The flip chip bonding is carried out by VTT<sup>2</sup>. Figure 3.9 explains the basic steps of the bump deposition process. The bump bonds are deposited only on the whole wafers. Both, the readout and the sensor wafer will undergo the same process with the difference, that most of the solder

<sup>2</sup>VTT Information Technology, Centre for Microelectronics, P.O. Box 1208, Tietotie 3, Otaniemi, Espoo, FIN-02044 VTT, Finland

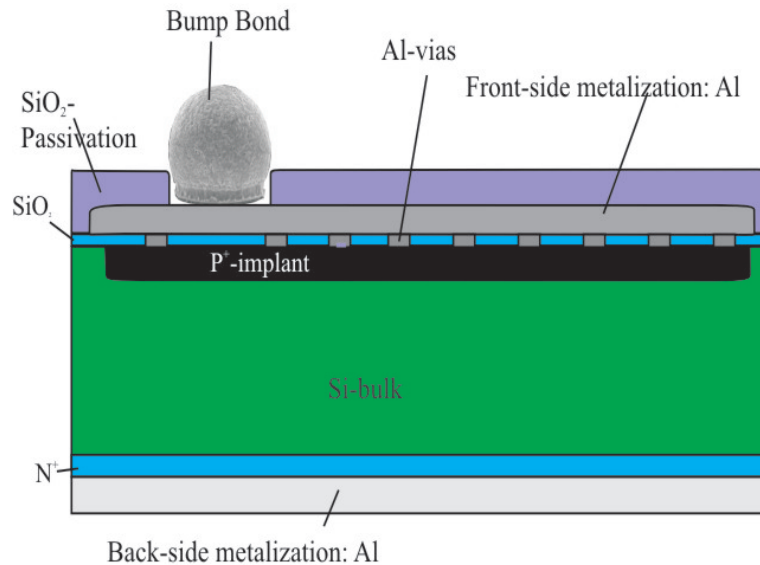


Figure 3.8: Schematic view of the profile layout of one pixel cell of the silicon sensor. The figure does not scale.

alloy will be placed on the readout wafer, while the sensor wafer will be coated only with a thin layer. As the first step, the field metal, in case of ALICE SPD it is a layer of TiW and a layer of Cu, is deposited on the contact metal (aluminum). A photo resist is exposed and developed as the next step leaving only the bump bond location accessible to the next layer. This is done in order to protect the rest of the front-side of the readout and the sensor wafer. A layer of under bump metallurgy (Ni) is electroplated on top of the field metal in a Ni-bath. As the last deposition step, the solder alloy (Pb-Sn) is electroplated. The different metal layers are necessary to ensure a good adhesion of the bump bond. After the removal of the photo resist, the field metal is etched away and the solder is heated in the reflow process. In Figure 3.10 (a) a SEM picture of one bump bond is shown. The bump bond has a diameter of  $25 \mu\text{m}$  prior to flip chip bonding, after that it is compressed to around  $12 \mu\text{m}$ .

As stated in chapter 3.2.1, the readout wafer is thinned down to  $150 \mu\text{m}$  after the bump bond deposition. Both wafers are then diced to get single readout chips and silicon sensors. For this a photo resist layer is spun on the front-side of the wafers protecting the surfaces from the silicon dust. Figure 3.10 (b) shows a picture of a readout wafer being diced at VTT. An UV-sensitive dicing tape is used for easy picking of the readout chips and sensors. After dicing, the protection layer of photo resist is removed.

Only Known Good Die (KGD - see chapter 4) are chosen for the flip chip process. The readout chip and the sensor are preliminary aligned ( $x$ ,  $y$  and  $\theta$ ) with an optical auto collimator and then heated to the tacking temperature. The softened bonds are bonded through thermocompression [40]. The hybridized assemblies are moved to the reflow oven, where the wetting and the self alignment takes place (for illustration see Figure 3.11).

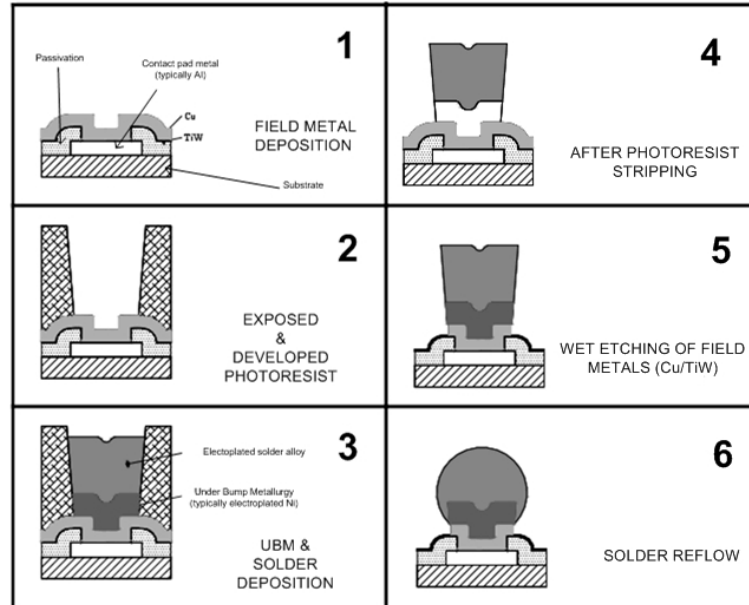
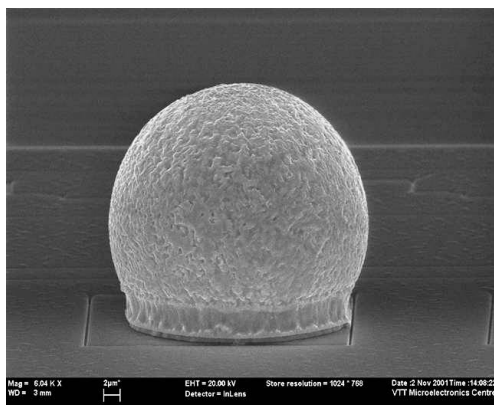


Figure 3.9: Schematic illustration of the bump deposition process [41]



(a)



(b)

Figure 3.10: SEM picture of one Pb-Sn bump bond on the readout wafer (a). Dicing process of one readout wafer at VTT (b). [41]

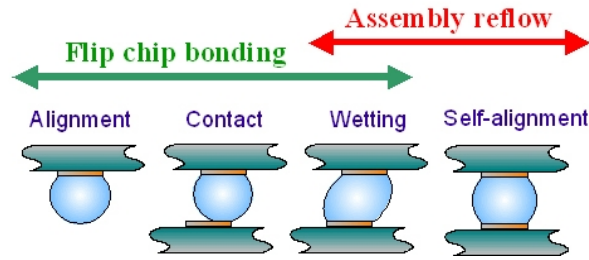


Figure 3.11: Assembly reflow process [41]

### 3.2.5 Front-end and Readout Electronics

#### Front-end Electronics (On-Detector)

The readout and control of the pixel readout chips is performed with the Multi Chip Module (MCM - see Figure 3.12), which is placed on the outer end of each half-stave. Three radiation tolerant ASICs developed in a commercial  $0.25\ \mu\text{m}$  CMOS design are located on the MCM: PILOT2003 (Digital Pilot), ANAPIL (Analog Pilot) and the GOL (Gigabit Optical Link) chip. The total height of the MCM with the ASICs is limited to 2 mm due to mechanical constraints. A lid glued on top of the MCM provides a protection against mechanical stress.

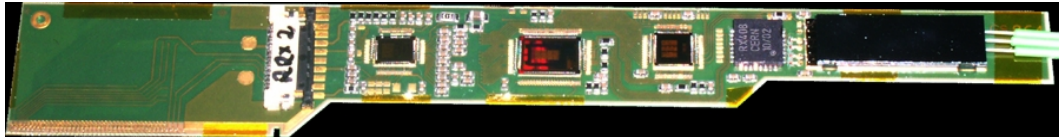


Figure 3.12: The ALICE SPD MCM. The ANAPIL, PILOT2003, the GOL and the optical package can be seen from left to right [42].

The Digital Pilot [43] transmits the clock, the signals and configuration commands received from the control room to the readout chips on the half-stave. It performs the readout of the pixel chips and formats and sends the readout data without zero-suppression via the GOL. The GOL serializes the data to an 800 Mb/s G-Link compatible stream [42] and controls the laser in the optical module. The Analog Pilot provides reference voltages to the pixel chips with 6 8-bit DACs and monitors the currents and voltages coming from the pixel chips and the temperature of the half-stave by a 10-bit ADC [44].

For the communication with the off-detector electronics the MCM contains an optical transceiver (a custom development of STmicroelectronics<sup>3</sup>), with three optical fibers using an 800 Mb/s communication protocol. The optical module has two O/E diodes and one

<sup>3</sup>STmicroelectronics, GENEVA Worldwide Headquarters, 39, Chemin du Champ des Filles, C. P. 21, CH 1228 Plan-Les-Ouates, GENEVA, Switzerland

1300 nm laser diode housed in a silicon package. Due to the tight space constraints, the optical module is limited to a volume of  $1.2 \times 17 \times 5.5 \text{ mm}^3$ .

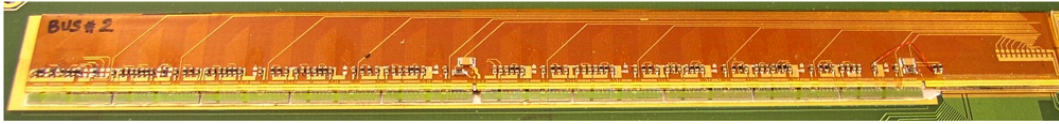


Figure 3.13: Picture of one pixel bus mounted on ladders [45].

The transmission of data and control signals from the MCM to the 10 pixel chips and the voltage supply is performed via an aluminum/polyimide multilayer laminate, the so called pixel bus (Figure 3.13). The connections to the pixel chips on one side and to the MCM on the other side are realized by  $25 \mu\text{m}$  thick aluminum wire bonds. In order to comply with the material budget constraints, the 5 conductive layers of the pixel bus are made out of aluminum. The bus technology development and full production has been done in the CERN TS-DEM. In total, the bus has a thickness of  $\sim 250 \mu\text{m}$ . Two layers are used for the voltage supply ( $50 \mu\text{m}$  thick), while three layers carry the data and control signals ( $10 \mu\text{m}$  thick). The layers of the pixel bus are arranged in a staircase configuration allowing access to each layer for the wire bonds, see Figure 3.14 and Figure 3.17. On top of the pixel bus, several SMD components are placed: The GTL-signal coming from the readout chips is read-out via the pull-up resistors and a PT1000 unit is used as a temperature sensor.

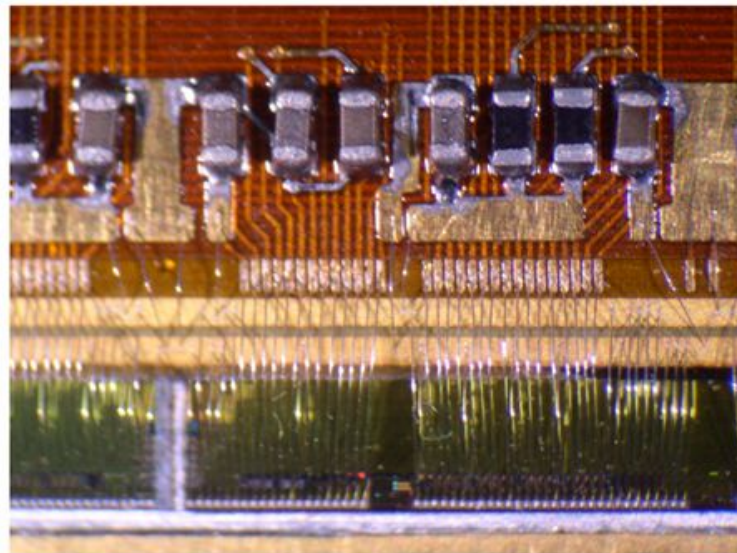


Figure 3.14: Image of the pixel bus connected via the wire bonds to the pixel chip [45].

### Readout Electronics (Off-Detector)

The readout chain is illustrated in Figure 3.15. At L1 trigger arrival the digital pilot chip on the MCM generates the strobe signal storing the hits waiting in the delay line into the FIFOs in the pixel cells. At a L2 YES trigger signal, the pixel chips are read out one after the other. The data from the 256 rows of one pixel chip are read out sequentially column by column with a 100 ns clock. This way, the 10 chips of one half-stave are read out within 256  $\mu$ s. The data from 10 pixel chips of each half-stave are transferred via the MCM and the optical fibers to the link receivers in the control room. The MCM itself does not perform any operations on the data, it just transmits data. At arrival of a L2 NO trigger, the data is discarded from the FIFOs.

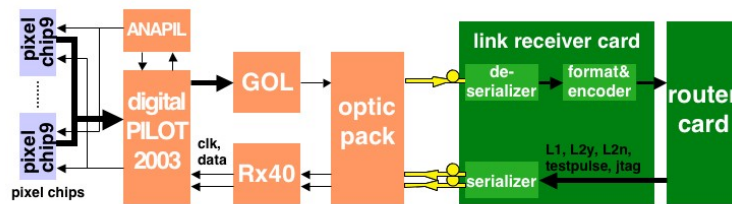


Figure 3.15: The readout chain of the ALICE SPD [46].

A link receiver card in the control room has the function to collect the data from two half-staves. One commercial FPGA is located on the link receiver, which checks the received data for format errors and performs the zero suppression on the data. The 32-Bit word coming from one row in one pixel chip is a sequence of logical 1s and 0s, where a logical 1 marks the hit position. It is transformed into a 5-Bit word giving the position of each logical 1 in that sequence and attaches the chip and row number to the entry.

Three such receiver cards are connected to one 9U VME [47] Module, called router [48]. The data from the three link receiver cards are transmitted to the event buffers on the router, where they are merged into a data block, which complies with the ALICE Data Acquisition (DAQ) format. The data block is then transferred via a detector data link DDL [49] to the ALICE DAQ. The router transmits the trigger commands from the ALICE TTC system [50] to the 3 link receiver cards. 20 router boards in the control room with 60 link receiver cards will serve 120 half-staves.

The ALICE SPD will receive the trigger from the Central Trigger Processor (CTP) through a standard interface, i.e. a TTC partition in the Local Trigger Crate (LTC). The CTP will synchronize all information from the triggering subdetectors and send the trigger signals to the other subdetectors. The purpose of the TTC unit is to receive the trigger signals from the CTP in an internal format and generate the trigger signals required by the subdetectors. A TTC unit consists of one Local Trigger unit (LTU) and two modules (TTCvi and TTCex) required for TTC signal generation. The trigger signals for the SPD will be sent from the TTC unit to the Router, where they are distributed via the Link receiver cards to the half-staves. A detailed description of the ALICE Trigger System, DAQ and DATE can be found in [51].

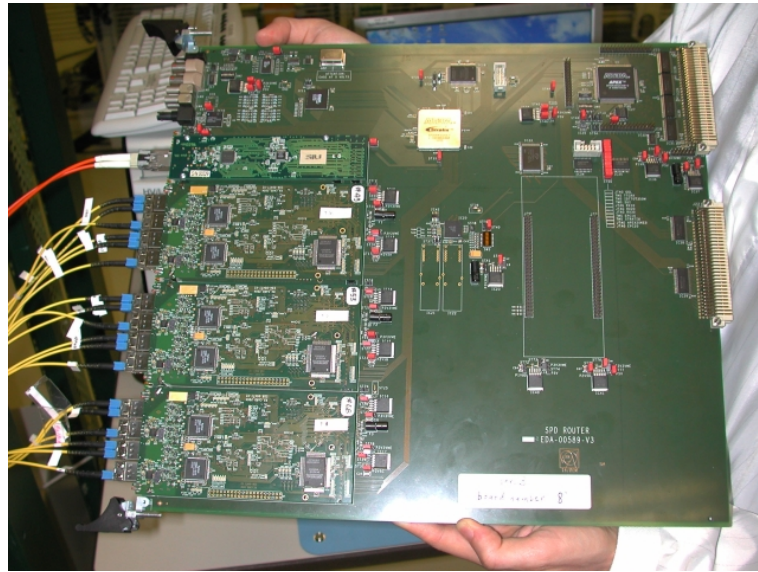


Figure 3.16: Image showing a router and three link receiver cards with the optical fibers connecting to the half-staves. The card above the link receiver card is the DDL unit.

### 3.2.6 Half-Stave and Sector Assembly

#### Half-Stave

The half-stave is the basic detector unit of the ALICE SPD. Two ladders are connected to one MCM via the pixel bus. The connections from the readout chips to the pixel bus and on the other side from the pixel bus to the MCM are realized through  $25\ \mu\text{m}$  thick aluminum wire bonds. The pixel bus is glued onto the sensors of the two ladders, leaving a  $300\ \mu\text{m} \times 100\ \mu\text{m}$  large window for the contact of the wire bond providing the bias voltage.

Each readout chip will dissipate  $\sim 800\ \text{mW}$  of power. In order to maintain the required temperature stability in the ALICE ITS the CFSS has cooling tubes made of  $40\ \mu\text{m}$  thick PHYNOX (Co-Cr-Ni alloy) tubes with  $2.6\ \text{mm}$  diameter flattened to  $0.6\ \text{mm}$  embedded. A two-phase evaporative cooling system based on  $\text{C}_4\text{F}_{10}$  is used to reach a stable optimum temperature of  $24\ ^\circ\text{C}$  [31]. Thermal grease is applied between the readout chip and the cooling tube. A view (not the scale) of the cross-section through the planes is shown in Figure 3.17. Due to the very small clearance ( $\sim 5\ \text{mm}$ ) between the SPD inner layer and the beam pipe the total thickness of the half-stave is limited to  $3\ \text{mm}$ .

#### Half-Stave Assembly

The half-stave assembly is one of the fundamental processes in the production of the ALICE SPD. The assembly involves several alignment steps and two gluing steps. A careful procedure

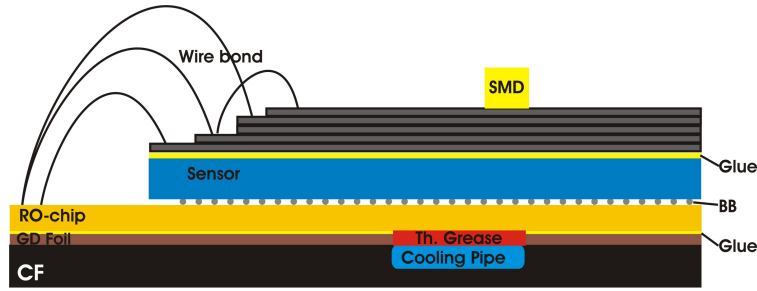


Figure 3.17: Drawing of the cross-section of the half-stave showing schematically the different layers and the connections between them

was developed [52]. As first step, two ladders are positioned and aligned to each other using a MITUTOYO<sup>4</sup> precision table. Electrically non-conductive glue is deposited on the grounding foil and the two ladders are placed on top of the grounding foil. Next, the MCM with optical fiber and extender busses is aligned with respect to the ladders and also glued onto the grounding foil. Then, the pixel bus is aligned with respect to the ladders and the MCM using as reference the wire bonding pads of the ten readout chips and the MCM. The same glue, as used in the first step, is deposited on top of the sensor back-sides and the pixel bus is placed onto the ladders.

After that, the half-stave is kept for 24 hours on a vacuum chuck to allow the glue to polymerize. Then, the alignment markers are checked and the pixel bus extender located above the MCM is soldered to the power layers of the pixel bus. In the last step, the signal lines of the pixel bus are wire-bonded to the pads on the readout chips and the MCM. In total  $\sim 1000$  wire bonds are needed for the construction of one half-stave. The assembly process can be seen partly in Figure 3.18 (schematic).

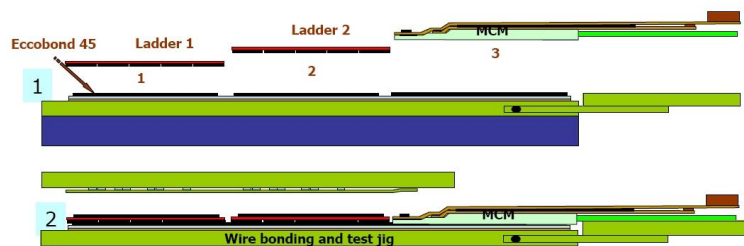


Figure 3.18: Assembly process of one SPD half-stave [52].

A precise gluing of both the grounding foil and the pixel bus is very important for the following wire-bonding step. A proper distribution of the glue, especially below the pixel bus, is crucial. Further, it has to be ensured that the glue does not flow on the contact pads on the readout

<sup>4</sup>MITUTOYO, Japan

chips and the MCM. Figure 3.19 shows a schematic view and Figure 3.20 an image of one SPD half-stave. After the assembly, the half-stave is tested electrically and using a radioactive source in order to ensure an errorless functioning.

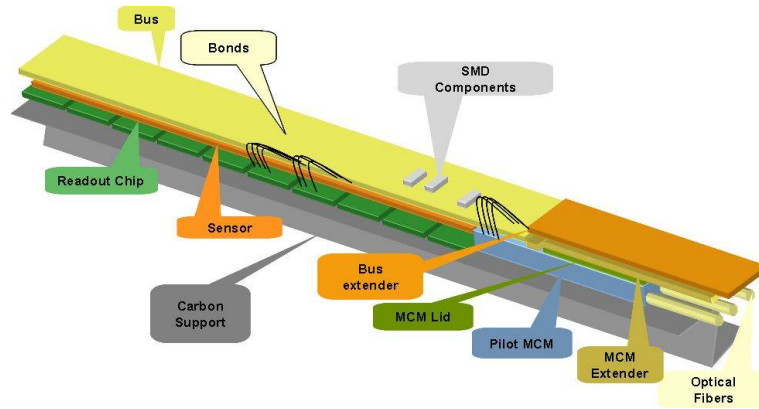


Figure 3.19: Schematic view of one SPD half-stave [53]

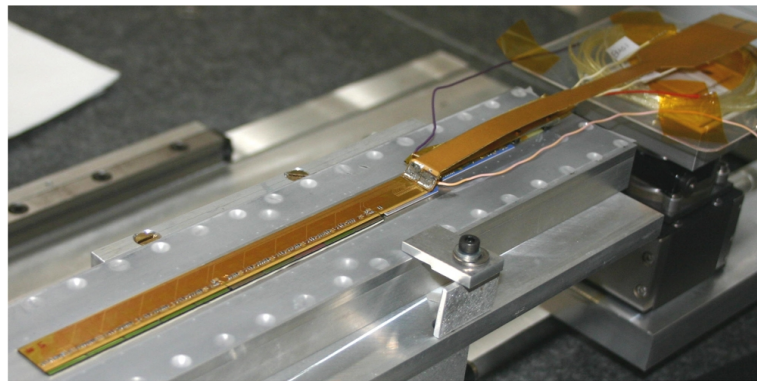


Figure 3.20: Image of one SPD half-stave. [54]

### Sector Assembly

The half-staves are mounted onto Carbon Fiber Support Sectors (CFSS). A detailed description of the sector assembly process can be found in [55]. The assembly procedure is as follows: The CFSS, already equipped with the cooling tubes, is aligned to the reference frame. Thin pads ( $\sim 150 \mu\text{m}$ ) of thermal grease are then deposited onto the CFSS. The pads have a rectangular form and correspond to each of the readout chips. The thermal grease ensures a good thermal contact between the half-staves and the cooling tube. Then two half-staves are aligned with respect to the reference plane and placed on their location of the CFSS using a vacuum chuck. Droplets of UV curable glue placed onto the CFSS hold the half-staves in position, while they

are being fixed with carbon fiber clips.

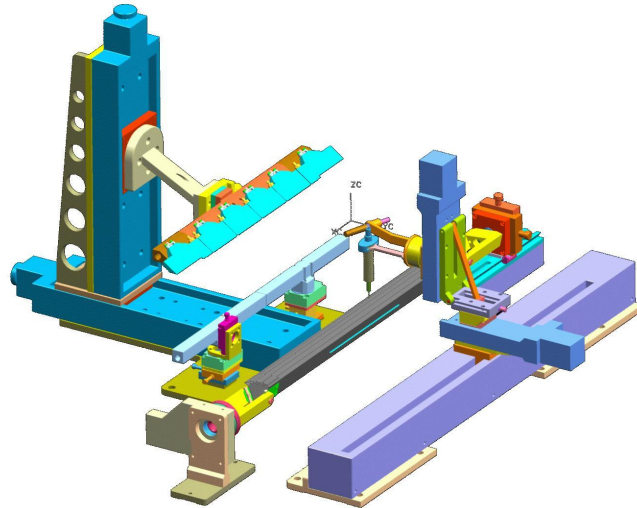


Figure 3.21: CAD view of the SPD Barrel Sector Assembly System (BSAS) [55].

In order to perform the sector assembly, a Barrel Sector Assembly System (BSAS) has been developed and built by the Padova group. A CAD-view of the BSAS can be seen in Figure 3.21. Its components are:

- The Rotating Sector Support (RSS), which is used to align and rotate the CFSS with respect to the reference plane.
- The Stave Alignment System (SAS), which adjusts the relative distance and the planarity of the two half-staves.
- The Stave Jig Tower (SJT), that picks up the stave from the SAS using a vacuum chuck. It transfers the stave to its position on the CFSS and holds it there during the gluing phase.
- The Grease and Glue Tower (GGT), which presents the main part of the BSAS. It distributes the thermal grease onto the CFSS. It also deposits the UV glue to fix the half-staves to the CFSS. Further, it carries a UV light source to cure the UV glue.

The movements of these components are mostly automated.

Six staves are mounted on one CFSS, 2 on the inner and 4 on the outer layer. Ten such CFSSs are connected to each other to form the SPD barrel. A picture of the half barrel with 5 CFSSs is shown in Figure 3.22. In Figure 3.23 the picture of the first assembled sector (sector Nr. 0 with  $\sim 1$  million pixel cells) is shown.

The half-staves on the inner layer are oriented in such a way, that the pixel bus faces the beam pipe, while the half-staves on the outer layer are oriented away from the beam pipe.

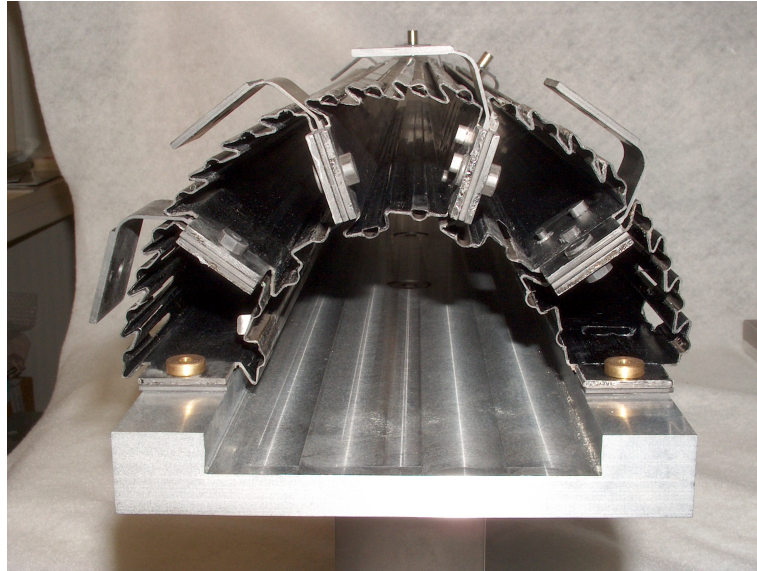


Figure 3.22: Image of the half barrel system used for the geometrical qualification. [31]

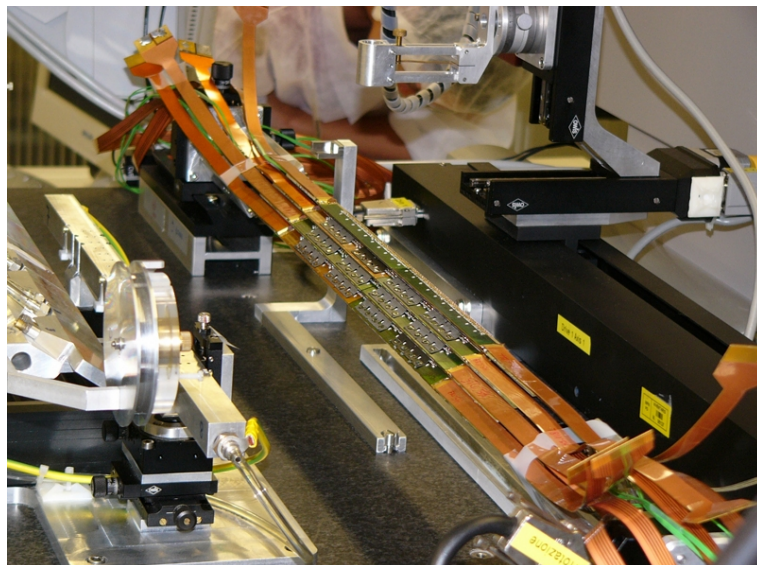


Figure 3.23: Image of one SPD sector. Power supply connections (extenders) on the left and right; the 4 outer staves visible in the middle. [31]

### 3.3 ALICE SPD Test Setup

The ALICE SPD Pixel Test System (PTS) was designed for two main reasons. First, it is used in SPD production tests (readout wafers and ladders). And secondly, the SPD prototypes used in beam tests 2002 and 2003 were read out and controlled using this system (see chapter 5). The PTS was reproduced several times and successfully installed in the collaborating institutes for production test purposes. In this chapter the PTS and the test system software are described.

#### 3.3.1 Readout Chain Architecture

The purpose of the test readout setup is to supply the necessary voltages and to carry out the DAQ. The system is based on LabVIEW and the connections between the hardware and the PC is realized via a National Instruments MXI-interface [56]. A schematic view of the SPD test setup can be seen in Figure 3.24 and a picture of the VME crate housing the four cards is shown in Figure 3.25. A VME-crate hosts the MXI-interface and three in house developed modules: the readout-Controller (PILOT module), the JTAG controller and the trigger card (SEPP). Via a DAQ adapter board (called MB card) [57] the connections are made to the probe card, which itself contacts the pads on the readout chip using tungsten needles with a tip radius of  $\sim 5 \mu\text{m}$ . In case of the SPD single chip assemblies as used in the beam tests or the laser setup (see chapter 5 and 6), the pixel carrier board, which accommodates the SPD assembly, is connected directly to the DAQ adapter. A more detailed description of the PTS can be found in [58].

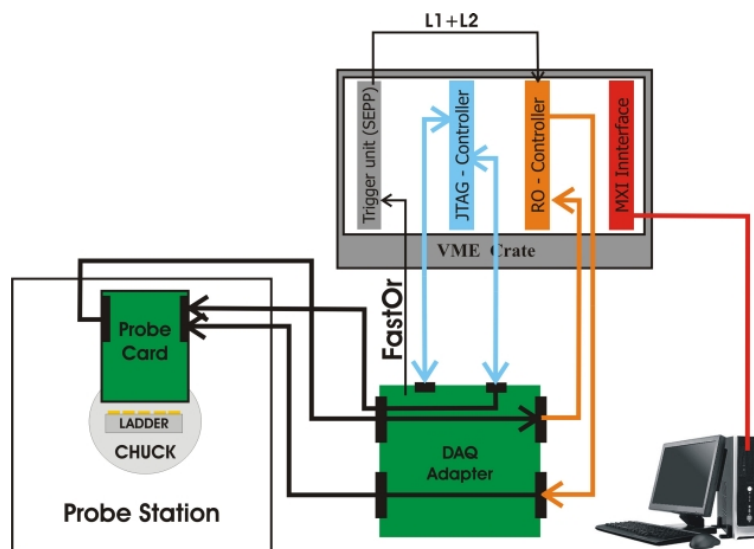


Figure 3.24: The layout of the SPD test setup.

The PILOT module was designed to control the readout of the pixel readout chips. It generates all signals necessary to perform the readout of the pixel chip. It can be triggered either by external L1- and L2-trigger signal or by commands sent from the PC software via the VME

bus. It also receives the data coming from the readout chip and performs zero suppression and hit encoding. The data is stored in built-in buffers on the card and is then sent to the DAQ.

The purpose of the JTAG controller is to configure and control the pixel readout chip. This involves the writing and reading of control signals, the masking of the pixel cells, generating a test pattern and threshold-adjust of each pixel cell. The chip internal DACs are controlled by the JTAG as well. The JTAG module also controls the DAQ adaptor board and uses for this purpose a second signal channel.

The trigger card receives the FastOr signal from the pixel readout chip via the DAQ adapter board and generates the L1 and L2 trigger. The trigger signals are sent to the PILOT module from where the readout of the pixel chip is controlled. The trigger card can be set to send a defined number of triggers.

The DAQ adapter board is located between the VME-crate and the pixel readout chip. It serves as a LVDS (Low Voltage Differential Signal) to GTL level adaptor. The Gunning Transceiver Logic (GTL - see chapter 3.2.1) signal is needed for the pixel bus connection. It is first translated to a TTL signal and afterwards to LVDS. Voltage supplies to the pixel chip are generated via the MB-card using three 5 V lines.

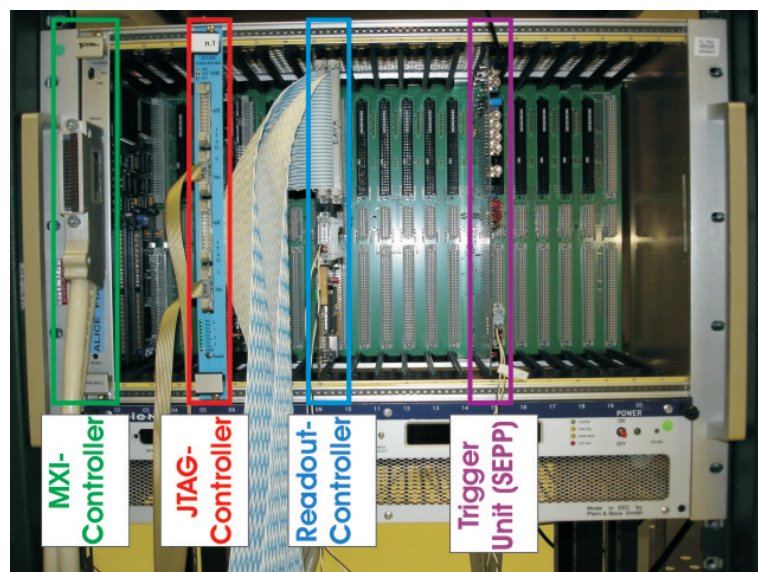


Figure 3.25: Picture of the VME-crate with the four modules. From left to right: VME-interface, JTAG card, RO-controller and trigger unit.

### 3.3.2 Test System Software

The PTS uses National Instrument's LabVIEW in connection with the Microsoft Windows operating system. CERN's package ROOT performs the offline analysis of the log files. The architecture of the PTS software is shown in Figure 3.26. The industrial standard Virtual Software

Architecture provides the interface to the hardware (VME). The drivers are used to communicate with the hardware. The connection between the driver layer and the services is realized through fixed protocols, what makes the PTS flexible with respect to hardware modifications. Specially developed database [60] allows an upload of all test results including pictures of the silicon sensor metalization.

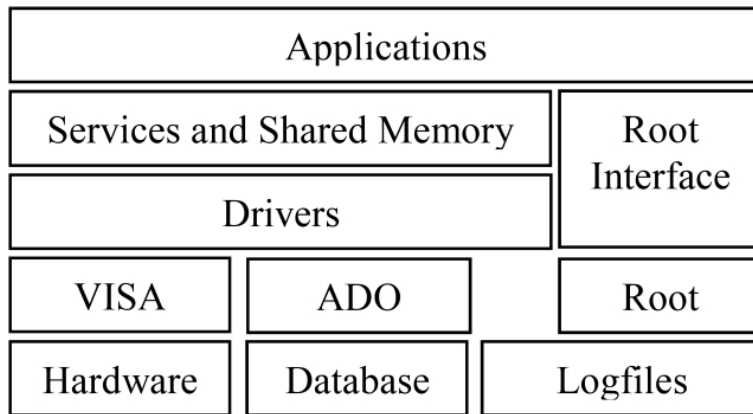


Figure 3.26: The architecture of the PTS software [58].

The main role of the services in the PTS architecture is data checking. The data coming from the pixel readout chips are checked for consistency. Problems at this level will be signaled to the application. Further, this layer takes care of the data flow. A simultaneous access to one hardware module by two processes is blocked here. Shared memory simplifies the communication between the different modules. The highest layer of the PTS is divided into applications and control panels. Each hardware unit has its own control panel, via which the unit can be configured, but also its status inquired. The applications fulfill the test tasks like JTAG integrity checks, DAC and threshold scans over the whole pixel matrix, but also masking and setting of the DAC values.

### 3.4 Summary

In this chapter a detailed description of the components of the ALICE SPD and the detector electronics is given. The SPD is the most inner part of the ITS tracking system of ALICE. It has 9.8 million pixel cells arranged in 10 sectors, each consisting of 12 half-staves. In order to limit the amount of data transferred off-detector, the readout of the SPD is binary. A two-shaper stage compares the signal height with the global set threshold. A logical one is written if the threshold is exceeded and a FastOr signal is generated, which is brought to off-detector electronics without further delay. The data is transferred via the MCM on optical fibers to the link receivers in the control room, where zero suppression and data formatting are performed.

The SPD planes have to comply with tight material budget constraints in order to have as small as possible influence on the traversing particles. In the design and production process,

these constraints were followed to the point. The sensor and the readout chip have a total thickness of only 350  $\mu\text{m}$  and the production of the full aluminum pixel bus turned out to be very challenging.

The half-stave assembly and the sector mounting have been explained. Assembly systems including several alignment and gluing steps were developed. Due to the small size of the components and the stringent alignment requirements the procedure has to be very precise.

The SPD test system described in this chapter has been duplicated and installed in several collaborating institutes. It has proven to be very reliable, but also flexible and is used for the testing of the SPD components (RO-wafers and ladders), as the DAQ- and control-system in beam tests 2002 and 2003 and in the laser setup. The PTS is very stable and can be easily adjusted to new requirements.



# Chapter 4

## Test Protocols in Production - Results

### Contents

---

4.1	Introduction . . . . .	<b>56</b>
4.2	ALICE SPD Probe Station . . . . .	<b>56</b>
4.3	Readout Chip Wafer Testing . . . . .	<b>58</b>
4.3.1	Test Procedure and Criteria . . . . .	58
4.3.2	Results - Readout Chip Yield . . . . .	61
4.4	Ladder Testing . . . . .	<b>63</b>
4.4.1	Ladder Test Procedure and Test Protocol . . . . .	63
4.4.2	Measurements and Results . . . . .	65
4.5	Sensor Tests . . . . .	<b>68</b>
4.5.1	Visual Inspection . . . . .	68
4.5.2	Study of the Back-Side Aluminum Adhesion . . . . .	71
4.5.3	Wire Bond Tests . . . . .	72
4.6	Metrology Measurements on Sensor Wafers and Ladders . . . . .	<b>74</b>
4.7	Summary . . . . .	<b>76</b>

---

## 4.1 Introduction

The construction of the ALICE SPD requires many testing steps during the production process. Each of the components (readout chip and the active sensor) are qualified prior to the bump-bonding process. The final detector module (ladder) is again tested to assure that no damages to the components occurred during the flip-chip bonding process. The development of the test procedures and the quality assurance criteria for to the testing of the SPD components is presented in this chapter.

## 4.2 ALICE SPD Probe Station

The test setup includes a SUSS<sup>1</sup> probe station and the SPD test system as explained in Chapter 3. A CCD camera connected to a microscope with 4 different lenses (magnification factors 2x, 10x, 25x, 50x) is used for visual inspection of the ladder. A picture of the probe station is shown in Figure 4.1.

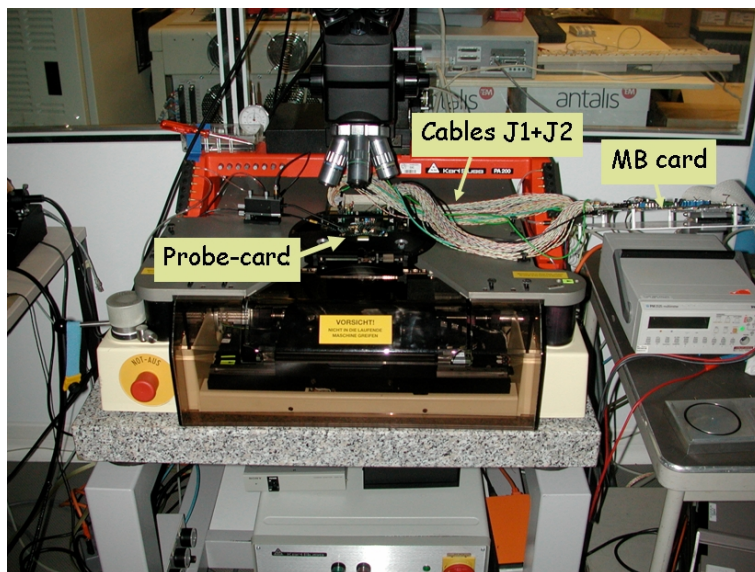


Figure 4.1: Image of the SUSS probe station at CERN. The probe card is connected via cables J1 + J2 to the DAQ adapter board. The voltage supply to the chip is provided via the DAQ adapter board, which is connected to a Gossen power supply (3 x 5 V).

The connection of the readout chip to the test system is provided via a specially developed probe card. The pads for the wire bonds in the periphery of the readout chip are contacted with probe needles coming from the probe card. In order to leave as small contact marks as possible on the pads, the tips of the needles have a tip radius of  $\sim 30 \mu\text{m}$ . The probe card was connected

<sup>1</sup>SUSS MicroTec Testsystems GmbH, Süß Str. 1, D-01561 Sacka Dresden, Germany

via flat cables to the DAQ adapter board, which then was connected to the test readout and control system.

Figure 4.2 shows the contacting of the pads. Utilizing the microscope and the CCD camera, the needles are aligned with respect to the pads. By decreasing the distance between the needles and the pads and observing the procedure under the microscope, the contact is made. The contact position can be stored, so that the contact procedure needs to be performed only for the first chip. Two pre-defined distances between the pads and the needles, which were set at  $500\ \mu\text{m}$  and  $1000\ \mu\text{m}$  above the contact height, can be used to separate the needles from the chip. In order to test the next chip, the chuck, on which the readout wafer or the ladder is positioned and held by vacuum, is moved so that the next chip can be connected to the probe needles.

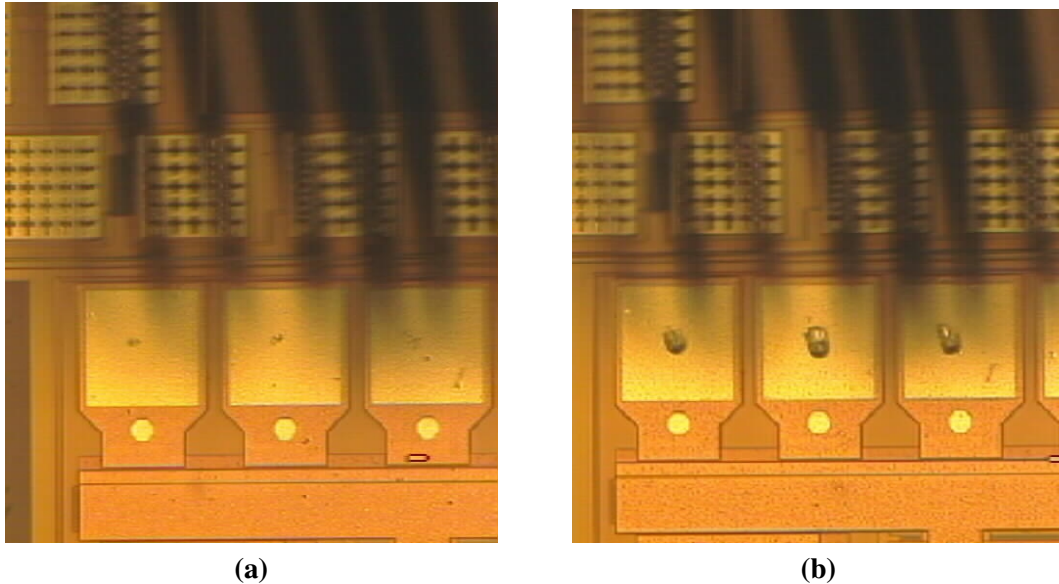


Figure 4.2: Pictures of the contact procedure: (a) First contact, marks are visible; (b) For a good contact the height of the chuck has to be increased by  $\sim 50\ \mu\text{m}$ .

In the following chapter, an overview of the production test criteria and the procedures is given. The results of these tests and the yield gained during the tests are displayed. Further, additional studies on surface structure of the sensors performed with a Scanning Electron Microscope (SEM) and metrology measurements, which became necessary due to different problems occurring during the production phase are explained.

## 4.3 Readout Chip Wafer Testing

### 4.3.1 Test Procedure and Criteria

After the positioning and alignment of the readout wafer, chip by chip are contacted and tested. The following test procedure is applied in order to select the readout chips for bump-bonding (see chapter 3.2.4) and to determine the Known Good Die (KGD) map [61]:

1. Measurements of the analog and digital current consumptions at 1.8 V.
2. JTAG functionality test: Three different logical patterns are sent to each pixel cell. The test is passed if the output from the pixel cells is identical to the sent pattern.
3. Internal DAC functionality: Each of the 42 8-bit DACs is scanned and the output is recorded. The speed and the step size can be varied during this test. The resulting DAC output curves are examined for the linearity and overall behavior.
4. Minimum threshold measurement: The global minimum threshold DAC setting is determined by varying the threshold and observing the output of the pixel matrix. The setting at which not a single pixel is firing is set as the minimum threshold.
5. Measurement of the mean minimum threshold and rms: The global threshold is set to the found minimum threshold value and a test pulse is applied to the pixel cells row by row. The test pulse is decreased from 60 mV to 0 V in steps of 2 mV and at each step 100 test pulses are sent to each pixel cell in the scanned row. The number of hits per pixel cell is recorded for each test pulse step in a file. The file is afterwards analyzed with a root macro. The mean threshold is calculated for each single pixel cell as the test pulse value at which half of the 100 test pulses are recorded (see Figure 4.3). Then, a histogram (see Figure 4.4), in which the test pulse is plotted on the x-axis, is filled with the corresponding number of pixel cells. The mean value of the fitted Gaussian curve will give the mean minimum threshold of the matrix.
6. Mean noise and rms: Using the same file recorded during the test pulse scan, the mean noise can be calculated. For each pixel cell the noise level is determined as one sigma of the width of the corresponding S-curve (see Figure 4.3). The noise value for each pixel cell is then and filled in a histogram giving the mean noise. An output example can be seen in Figure 4.5

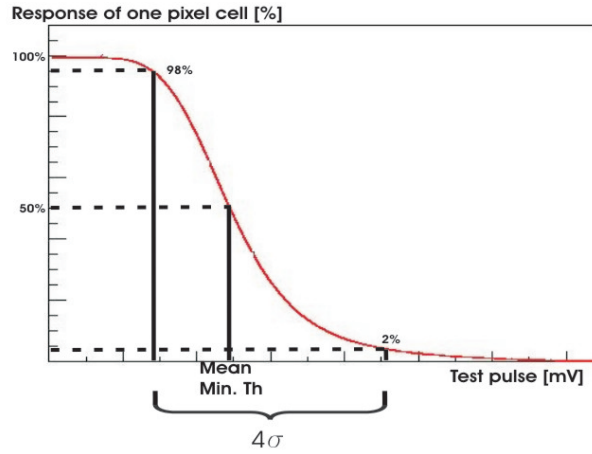


Figure 4.3: Illustration of the calculation of the mean threshold and the noise of one ALICE1HCB pixel cell using the response to an applied test pulse (Scurve)

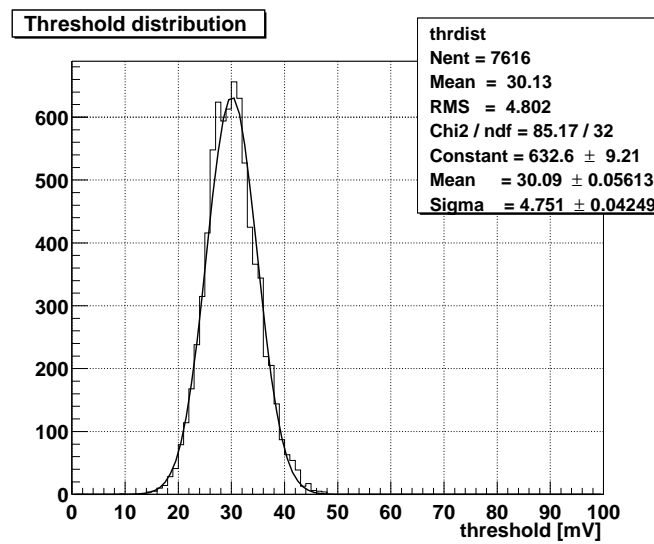


Figure 4.4: Histogram displaying the mean minimum threshold of a readout chip plotted for the height of the test pulse in mV.

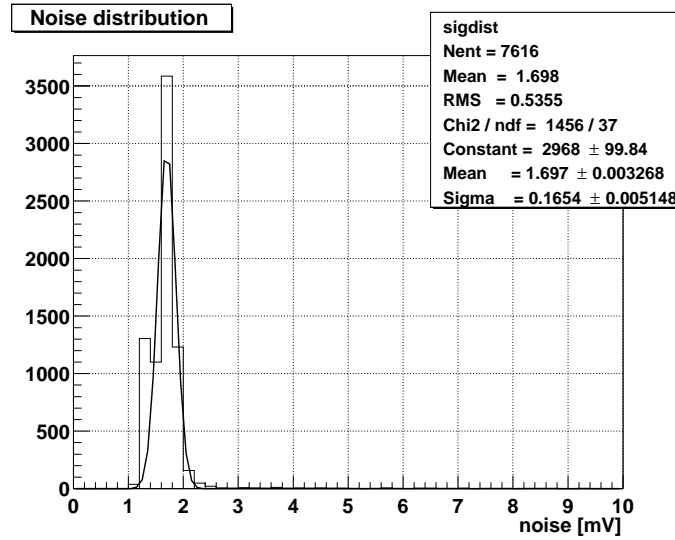


Figure 4.5: Histogram displaying the mean noise of a readout chip plotted in mV.

Table 4.1 summarizes the qualification criteria for the readout chips:

<b>Class I Chips for Bump Bonding</b>	<b>Class II Chips with Minor Defects</b>	<b>Class III Chips with Major Defects</b>
<p><b>Requirements:</b>            JTAG and DAC test passed.</p> <p><math>I_{\text{analog}} \leq 350 \text{ mA}</math></p> <p><math>I_{\text{digital}} \leq 270 \text{ mA}</math></p> <p>The mean threshold is less than 30 mV</p> <p>Less than 1% (82) missing or defect pixels are detected in threshold scan</p>	<p><b>Requirements:</b>            JTAG and DAC test passed.</p> <p><math>I_{\text{analog}} \leq 350 \text{ mA}</math></p> <p><math>I_{\text{digital}} \leq 270 \text{ mA}</math></p> <p><b>Allowed defects:</b>            mean threshold is higher than 30 mV</p> <p>Parts of a column or one or more columns are missing</p> <p>More than 1% of pixel are missing or defect</p>	<p><b>Defects:</b>            JTAG test not passed</p> <p>DAC test not passed</p> <p><math>I_{\text{analog}} \geq 350 \text{ mA}</math></p> <p><math>I_{\text{digital}} \geq 270 \text{ mA}</math></p> <p>Masking error occurs during the threshold scan</p> <p>No minimum threshold found</p> <p>There is no digital output</p>

Table 4.1: Classification criteria for the ALICE1LHCB readout chip [61]. These criteria are in use since 2002. They are based on the first wafer probing tests carried out in July and August 2001.

The class I chips are fully functional and only these chips are used for detector production. Class II chips are fully functioning, but show a less good performance in mean threshold and functioning pixel cells. These chips can be used for lab tests. Finally, class III chips show severe defects in their functionality and are not used for electrical tests.

All results from the readout wafer testing are stored in a common ALICE pixel database based on MySQL [60].

### 4.3.2 Results - Readout Chip Yield

Up to now 53 readout readout wafers have been tested. The average number of class I chips per readout wafer amounts to  $\sim 44$  chips with an rms spread of  $\sim 8$  chips.  $\sim 8.5$  chips have been classified as class II (RMS spread of  $\sim 3.5$  chips) and  $\sim 33.44$  as class III (rms spread of  $\sim 8$  chips). In Figure 4.6 the number of class I chips is plotted for each tested wafer and in Figure 4.7 the average yield per readout wafer.

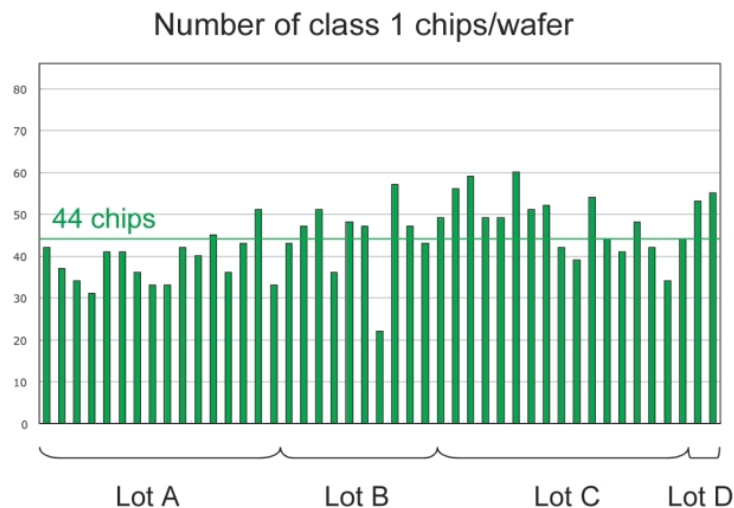


Figure 4.6: The diagram displays the number of class I chips per readout wafer. In average  $\sim 44$  chips are classified as class I. [62]

For each wafer a KGD map has been created. It was sent together with the wafer to the bump bonding site. The chips classified as class II or III show an X on the map in order to avoid mistakes when the chips are chosen for flip chip bonding. In Figure 4.8 the KGD map of the readout wafer L4293VT is shown.

As the FastOr signal<sup>2</sup> will contribute to the L0 trigger decision<sup>3</sup>, a threshold test on the FastOr signal was introduced as a qualification criteria. The minimum threshold for the FastOr signal,

<sup>2</sup>For a detailed explanation of the FastOr signal see chapter 3

<sup>3</sup>In chapter 6.6, a more detailed explanation of the Pixel Trigger (PIT) can be found



i.e. the threshold at which the FastOr signal is not observed any more, is found and noted. Chips showing no minimum threshold for the FastOr signal, are classified as class II. This test should determine and reject readout chips showing a noisy FastOr signal, which would make the use as a part of the trigger decision more difficult. In Figure 4.9 the result of the minimum threshold for the FastOr signal for each readout chip of the RO-wafer L4293VT is compared to the global minimum threshold. It can be observed, that in average the threshold for the FastOr signal lies about 10 DAC settings below the global minimum threshold. This is partially due to the long cables which were used at the prober. Similar tests on half-staves show a much smaller difference.

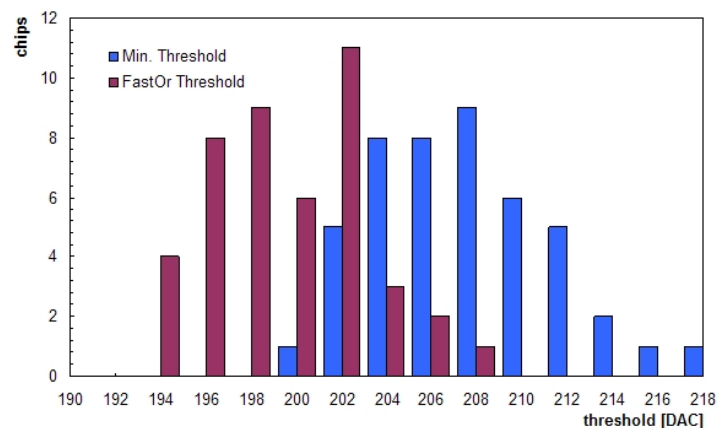


Figure 4.9: Diagram showing the minimum global threshold and the FastOr threshold for the RO-wafer L4293VT.

## 4.4 Ladder Testing

### 4.4.1 Ladder Test Procedure and Test Protocol

The ALICE SPD ladders are tested at the same probe station with the same test system as the SPD RO-wafers. The test procedures though had to be adapted to the testing requirements. The contact of the readout chips of the ladders are performed in the same way as in case of the wafers. Additionally, the ladders have also to be supplied with the sensor bias voltage. For this reason, the aluminum layer on the sensor back-side is contacted with a needle, which is connected to a Keithley<sup>4</sup> power supply. The bias needle is supported by a manipulator, which can move the needle in x, y and z-direction. The manipulator is also providing the connection to the ground coming from the probe card via a coax cable. In Figure 4.10 the setup providing the bias voltage is illustrated and in Figure 4.11 an image showing the contacting of a ladder is

<sup>4</sup>Keithley Instruments, Inc., 28775 Aurora Road, Cleveland, Ohio 44139

shown. The Keithley power supply measures also simultaneously the total leakage current of the detector.

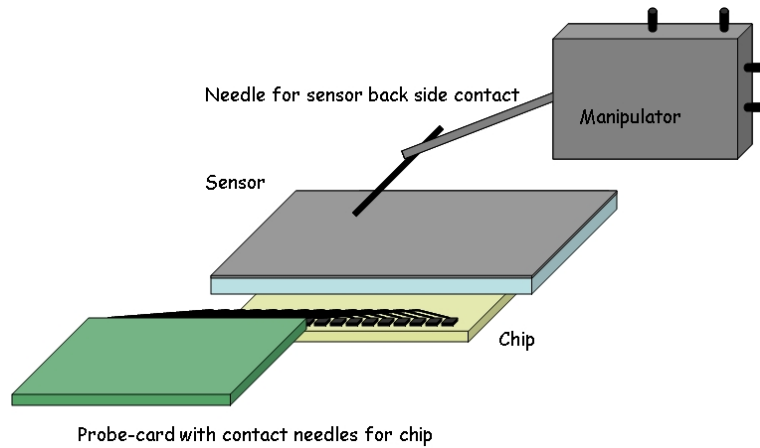


Figure 4.10: Illustration of needle contacts to the SPD ladder and measuring of the leakage current [63]

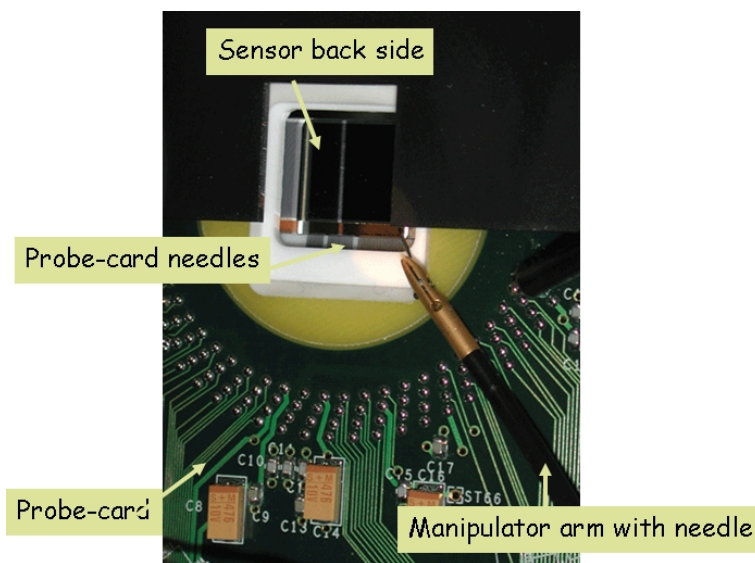


Figure 4.11: Picture showing the contacting of a ladder [63].

Since a change in the internal DAC functionality of a readout chip during the flip-chip bonding process was not expected and in the first ladder tests not observed it was decided to leave it out in the SPD ladder test procedure. An additional step in the test procedure was introduced to identify missing bonds. A radioactive source ( $^{90}\text{Sr}$   $\beta$ -source) illuminates the sensor above the chip under test. The complete test procedure for the SPD ladders, which otherwise is similar to the readout wafer tests, is listed below:

1. The sensor back-side of each SPD ladder is inspected visually utilizing the microscope and the CCD camera. The damages in the aluminum layer or on the edges are photographed and noted on the test sheet.
2. The leakage current of the ladder is tested up to a bias setting of 100 V in 10 V steps. The bias voltage is for the rest of the procedure set to 50 V, if the leakage current permits this.
3. Measurements of the analog and digital current consumptions at 1.8 V chip voltage.
4. JTAG functionality test.
5. Minimum global threshold and FastOr signal threshold are determined.
6. Measurement of the mean threshold and noise by means of a test-pulse scan.
7. Radioactive source test: The FastOr signal of the SPD is used to generate the L1 and L2 trigger signal. The resulting hit map is saved as a dat-file and analyzed giving the positions of defect (dead, in-, overefficient or noisy) pixels. During the source test, the FastOr DACs (Fast\_cgpoll, Fast\_compref and Fast\_convpoll) are scanned to optimize the uniformity of the response of the pixel matrix. The optimum FastOr DACs settings are noted on the test sheet.

In Table 4.2 the qualification criteria for the SPD ladders are presented:

#### 4.4.2 Measurements and Results

Up to now 211 ladders including the prototype modules have been produced by the bonding foundry VTT. The first 20 ladders were used for tests and will not be used for the half-stave assembly and are not discussed in this thesis. From the 191 production ladders, 156 ladders have been tested until now. In Figure 4.12 the classifications of the ladders is presented. About 66% of the ladders fulfilled the requirements for half-stave mounting.

In total, 103 ladders have been tested to be class I and as such will be used for half-stave production. 21 class II ladders have been found, out of which 14 had more than 1% but less than 3% defect bump-bonds and 7 ladders had a leakage current between 2 and 5  $\mu\text{A}$ . 32 ladders showed major defects and were tested as class III due to the following requirements:

- 10 ladders had a leakage current exceeding 5  $\mu\text{A}$
- 5 ladders had dead or not responding chip
- 6 ladders had more than 3% defect bump-bonds
- 6 ladders showed on or more noisy, not maskable pixels
- for 4 ladders no minimum threshold for the FastOr signal in one of the chips could be found

<b>Class I used for HS<sup>5</sup> mounting</b>	<b>Class II backup for HS mounting</b>	<b>Class III not used for HS mounting</b>
<b>Requirements:</b> JTAG test passed.  $I_{\text{analog}} \leq 350 \text{ mA}$  $I_{\text{digital}} \leq 270 \text{ mA}$  Minimum threshold exists  FastOr min. th. exists  Mean threshold is less than 50 mV ( $\sim 3000 e^-$ )  Noisy Pixel can be masked  Less than 1% defect pixels in threshold scan and source test  leakage current stable and $\leq 2 \mu\text{A}$ at 50 V	<b>Requirements:</b> JTAG test passed.  $I_{\text{analog}} \leq 350 \text{ mA}$  $I_{\text{digital}} \leq 270 \text{ mA}$  Minimum threshold exists  FastOr min. th. exists  Mean threshold is less than 50 mV ( $\sim 3000 e^-$ )  More than 1% but less than 3% defect pixels in threshold scan and source test  leakage current stable and $\geq 2 \mu\text{A}$ but $\leq 5 \mu\text{A}$ at 50 V	<b>Defects:</b> $I_{\text{analog}} \geq 350 \text{ mA}$  $I_{\text{analog}} \geq 270 \text{ mA}$  JTAG test failed  Minimum threshold does not exist  Mean threshold $\geq 50 \text{ mV}$  Noisy pixel can not be masked  FastOr minimum threshold does not exist  More than 3% defect pixels in threshold scan and source test  leakage current instable or $\geq 5 \mu\text{A}$ at 50 V

Table 4.2: Classification criteria for the ALICE SPD ladders [61].

- and finally, for 1 ladder no global minimum threshold could be found in one readout chip.

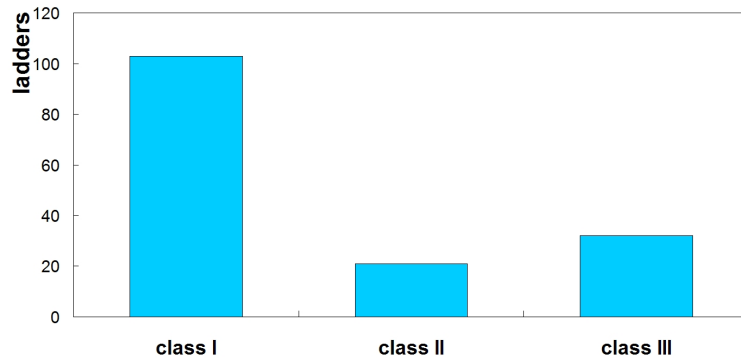


Figure 4.12: Yield of the ladder production [61].

Most of the 825 chips showed excellent bump-bonding yield with less than 1% (82) defect pixels. In Figure 4.13 the missing bond per chip for each of the tested ladders is presented. The average number of missing bonds per chip amounts to 6.5. The position of the chip in the ladder did not have a significant effect on the pixel defects.

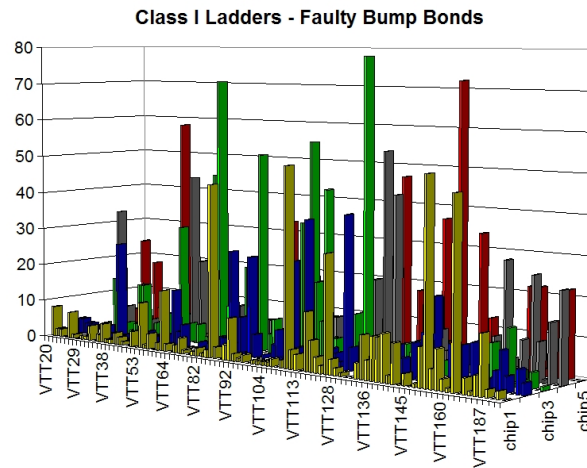


Figure 4.13: Defect pixels per chip and per class I SPD ladder [61].

In total 17 ladders had to be rejected due to the leakage current, which after the bump-bonding yield, was the second most often reason for a ladder not to be classified to class I. Figure 4.14 shows the number of ladders as a function of the leakage current.

Ladders, which were rejected due to defects in only one chip, have been chosen for rework at the bonding foundry. The first results seem to be very promising, but since the sample size of

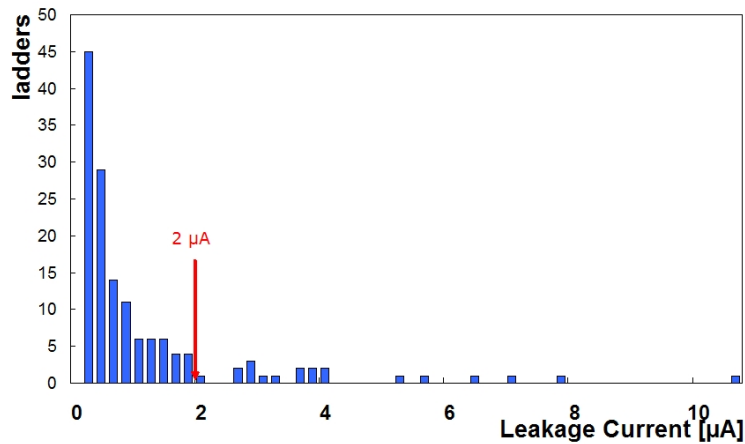


Figure 4.14: Distribution of the leakage current for all tested SPD ladders [61].

the reworked ladders up to now is not very large, no serious statistics can be given. However, reworking of ladders should raise the overall yield in the ladder production.

The hitmap as the response to an illumination of a SDP ladder with a strong  $^{90}\text{Sr}$  source ( $\sim 36$  MBq nominal) is shown in Figure 4.15. The distribution is Gaussian in both directions due to the collimator of the source support and the response of the pixel matrix is uniform. In Figure 4.16 the uniformity of the response is bad. The columns in the middle are overefficient with respect to the rest of the pixel matrix. The Sr-source used for this measurement was weaker (below 2 MBq nominal) and no Gaussian distribution can be seen due to a large collimator of this source support. Adjusting the FastOr DACs restored the uniformity of the pixel matrix, as it can be seen in figure 4.17. In the upper right corners of the hitmaps presented, the shadowing effect due to the bias needle can be seen.

## 4.5 Sensor Tests

The sensors are prior to the bump-bonding tested by means of visual inspection, electrical tests, and sample measurements utilizing metrology inspections and a scanning electron microscope (SEM). In Appendix A the functionality of the SEM is explained.

### 4.5.1 Visual Inspection

In the visual inspections, the alignment of the different layers is tested by checking of the position markers. Further, the deposition of the aluminum on the front- and back-side is examined. Figure 4.18 shows images taken during the visual inspections. In the image to the left a good separation of the aluminum layers covering the  $\text{p}^+$ -implant on the front-side of the sensor can

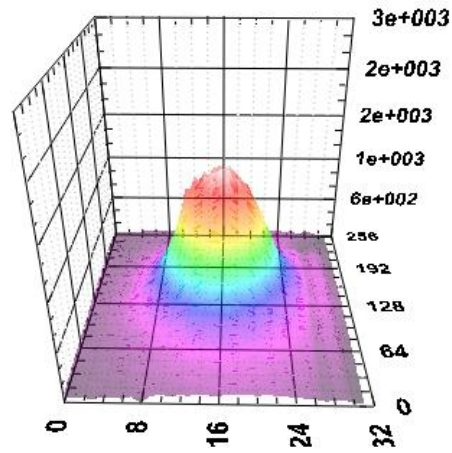


Figure 4.15: Hitmap of the ladder 75 after illumination with a strong  $^{90}\text{Sr}$  source.

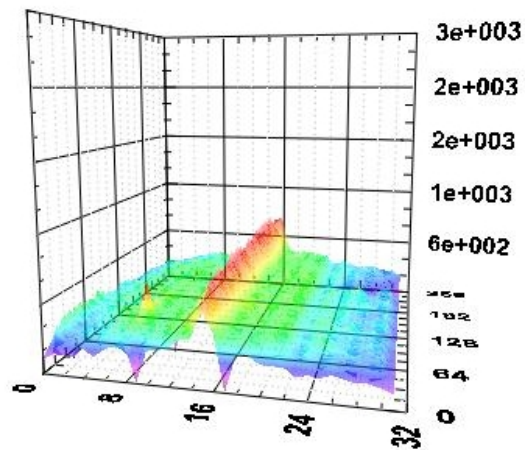


Figure 4.16: Response of the pixel matrix of the ladder 150 to the illumination with the weaker  $^{90}\text{Sr}$  source. The FastOr DACs are not adjusted, which results in a non-uniform response of the pixel matrix.

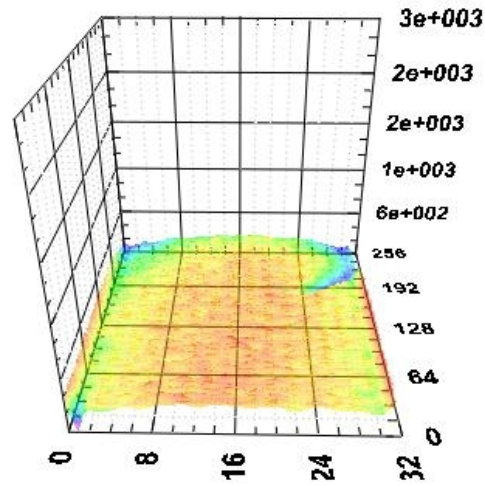


Figure 4.17: Hitmap of the ladder 150 after the adjustment of the FastOr DACs. The response is now uniform over the whole pixel matrix.

be seen. The guard ring and the bump-bond positions are visible. In the image to the right, a position marker is shown. The different layers above each other are well aligned.

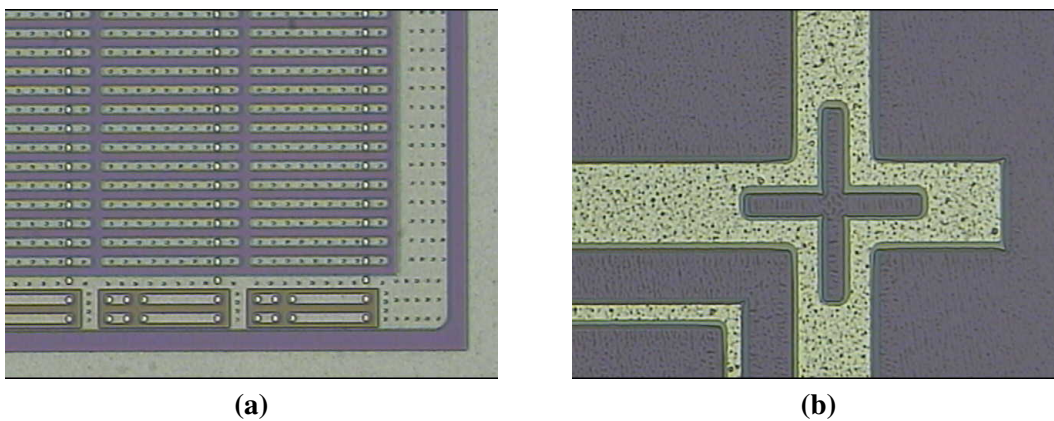


Figure 4.18: Microscope view of the front-side of the sensor wafer 56226.

All sensor wafers have been examined before the flip-chip bonding process and the data has been recorded.

### 4.5.2 Study of the Back-Side Aluminum Adhesion

Until 2003, the passivation of sensor wafers, which are produced at CANBERRA, was done with polyimide (PI). Since the bonding company VTT in Finland observed difficulties with bump bonding due to the PI-passivation, the  $\text{SiO}_2$ -passivation was tried out. The first reworked sensors showed very good bump bonding results and so it was decided in 2004 to use  $\text{SiO}_2$  passivated sensor wafers for the ALICE-SPD. In March 2004, five sensor wafers with an open back side for laser tests and  $\text{SiO}_2$ -passivation were used for assembly. On the backside of the produced ladders delamination of the Al-ring appeared. In Figure 4.19 the delamination can be observed.

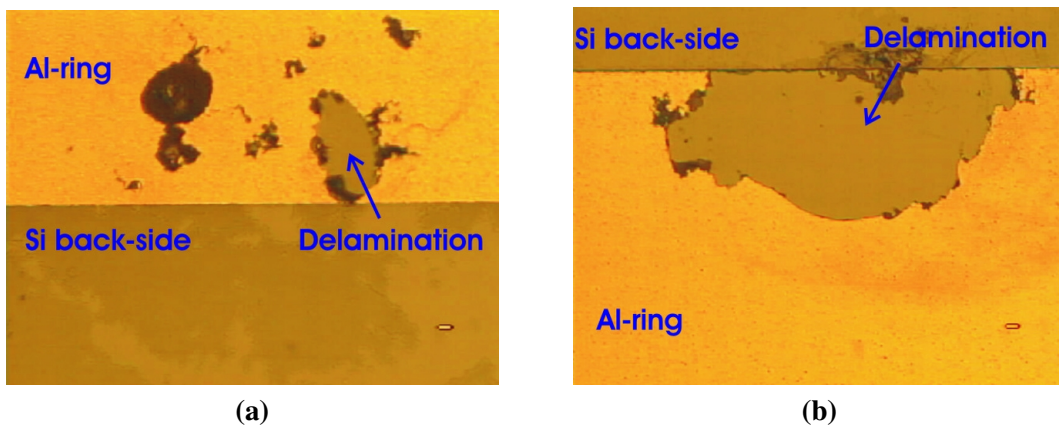


Figure 4.19: Microscope view of the delamination spots on the sensor backside of the ladders 25 (left) and 24 (right) taken with a magnification factor 2 and 10.

Therefore many ladder-sensors were rejected already at VTT before bump bonding. The ladders and singles produced were delivered to CERN and examined visually, using a SEM, aging test and wire bonding tests. Taking in account the 10 years of runtime for the ALICE experiment, these problems needed to be investigated. In particular the stability of the remaining Aluminum on the backside is a matter of interest.

The backside of the singles was inspected with a SEM with the goal to display the exact shape of the delamination spots and look for some abnormalities in the surface of the aluminum and the silicon as well as to look for surface impurities. The investigation showed a sharp edge of the remaining Aluminum layer with the foreseen thickness of around  $1 \mu\text{m}$  as can be seen in Figure 4.20. These results would indicate a rather stable remaining Al-layer with no further delamination to be expected.

To study this problem more carefully further production deliveries of sensor wafers were put on hold and CANBERRA started a series of specially processed wafers. The first delivery of test wafers consisted of 4 sensor wafers. Two of them were reworked old wafers. For one of the reworked wafers an extra cleaning step was included. For the other two test wafers a different processing step to deposit the aluminum layer was used. The results of these measurements are

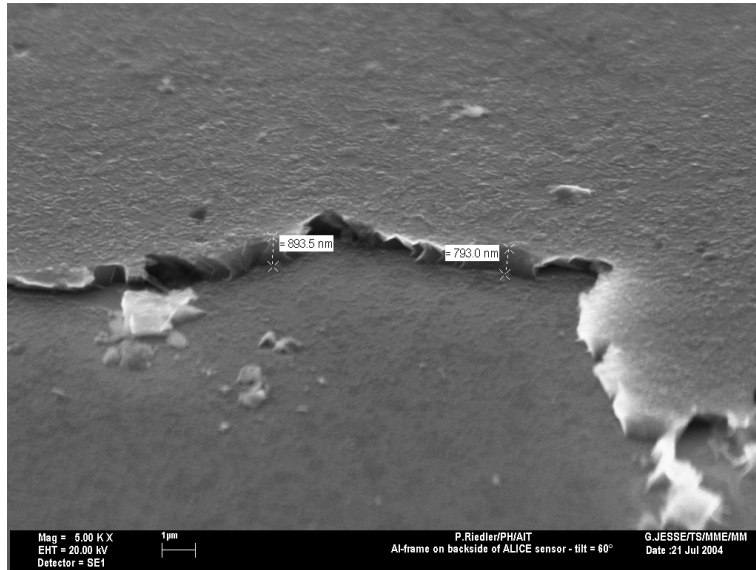


Figure 4.20: SEM-view of a delamination spot. The picture was taken at a tilt angle of  $60^\circ$  with a 20 kV e-beam.

presented in [65].

### 4.5.3 Wire Bond Tests

With the occurrence of aluminum delamination on the back-side of the silicon sensor, it became necessary to examine the stability of the wire bonds to the aluminum. These wire bonds are the connections for the bias voltage to the silicon sensor and thus their stability is very important. Wire bonds were placed on the Al-ring of one of the singles showing Al-delamination problems. The wire bonds were placed close to one delamination spot. Pull tests on those wire bonds showed no instability of the Al-layer. A force of 12 to 13 g was necessary for a 15 g wire, which is a comparable result to previous pull tests on sensors showing no delamination. In Figure 4.21 the remaining feet of the wire bonds can be seen as well as the delamination spots.

These pull-tests were repeated on several SPD assemblies. All the tests showed a good stability of the wire bonds, even in the close vicinity of delamination spots in aluminum. The usual force needed to break a placed wire bond amounted to about 11 to 13 gram.

In case of one sensor, the remaining wire bond feet were examined utilizing a SEM in order to examine possible resulting delamination of the aluminum layer. The feet of 8 placed wire bonds can be seen in Figure 4.22. Each of the bond feet was then examined in more detail at a higher magnification.

While some of the bond feet were removed completely, most of them, were still present after

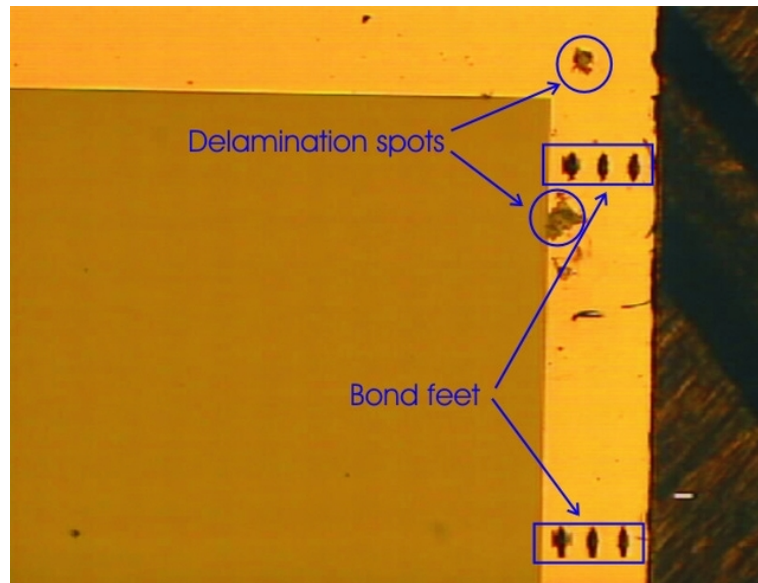


Figure 4.21: Microscope view of the backside of a single showing delamination spots and the wire bonds feet taken with a magnification factor 2.

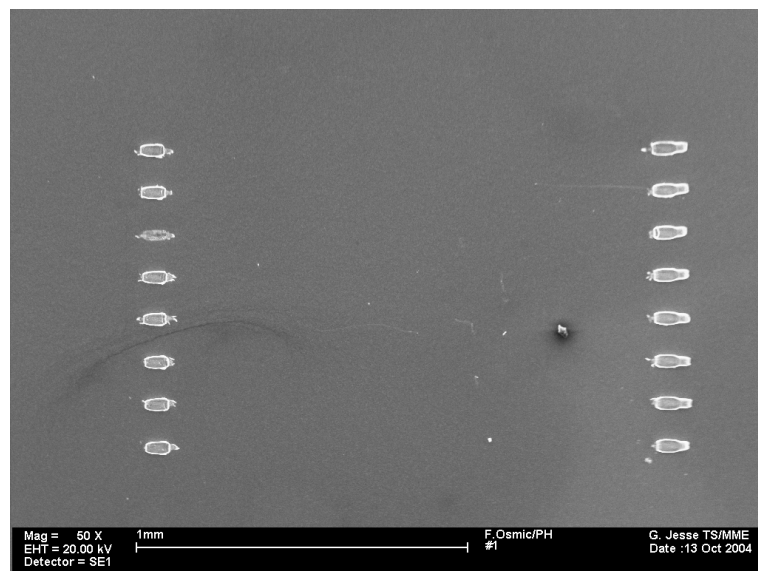


Figure 4.22: SEM-view of the bond feet, which remained after the pull-tests, on the aluminum layer on the back-side of an SPD assembly. The picture was taken at a magnification x50 with a 20 kV e-beam.

the pull-tests. Figure 4.23 shows the traces of two different bond feet in the case of the complete removal. While in the image to the left, the aluminum at some spots was taken completely away and the bare silicon surface below can be seen, in the image to the right the aluminum layer is still continuous although damaged. In both cases, the remaining aluminum seemed to be very stable, since no larger delamination of the aluminum layer occurred during the pull-tests. The results were therefore very encouraging.

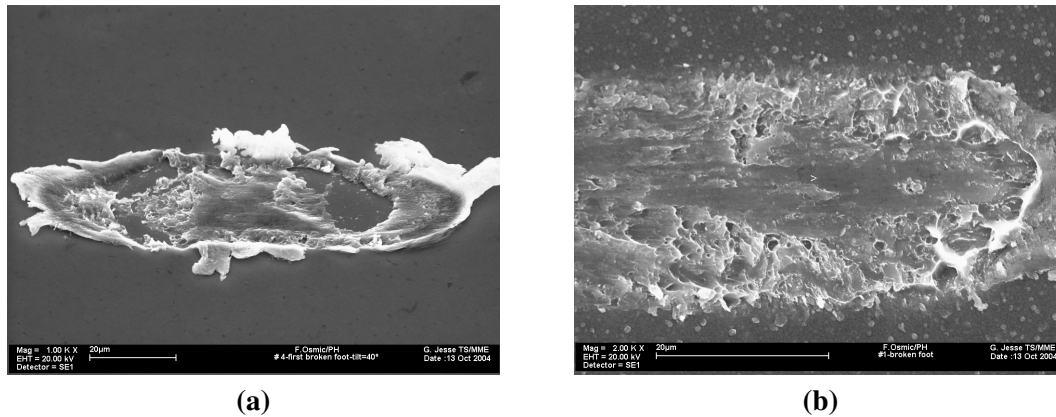


Figure 4.23: A closer SEM-view (magnification x1000) of the bond feet. The electron energy was set to 20 keV.

Improvement of the delamination was only found in the case of an additional cleaning and protection step before the Al deposition on the back side. However, small holes remained. The novel protection cleaning procedures in the wafer processing have been established based on these results and lead to a solution of this problem.

## 4.6 Metrology Measurements on Sensor Wafers and Ladders

During the tests of the ladders 118 to 124 open contacts were observed in chip corners of the ladders. Each chip of the mentioned ladders showed from 20 to 70 missing bond contacts in the corners. In order to study this defect in more detail, it was decided to investigate the ladder 122 by means of a metrology measurement, carried out with the help of the TS-MME group.

This measurement uses a laser system and a calibrated table. The distance to different points on the ladder is recorded with respect to the calibrated table. The data is then stored and analyzed. In Figure 4.24 the conducted measurements on the back and the front side of the ladder are illustrated and in Figures 4.25 and 4.26 the results of these measurements are shown. In [66] the measurements and the results are presented.

Metrology of ladder 122 shows a sensor bow of  $\sim 45 \mu\text{m}$  and a chip bow (bowl shape) of  $\sim 6 \mu\text{m}$ . Same measurements were repeated on the ladder 133, which showed no open contacts. The sensor bow for this ladder amounted to  $\sim 55 \mu\text{m}$  and the chip bow to only  $\sim 2\text{-}3 \mu\text{m}$ . This

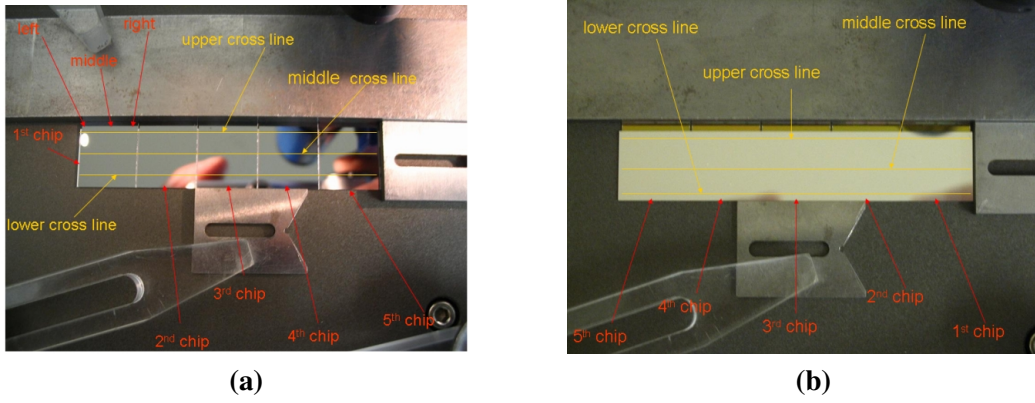


Figure 4.24: Images of the ladder 122 during the metrology measurements. The directions of the measurements are illustrated. [66]

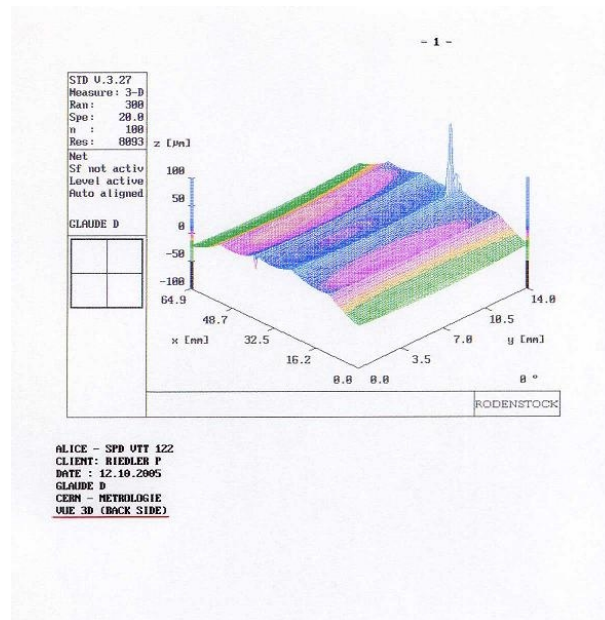


Figure 4.25: The results of the metrology measurements of the chip side of the SPD ladder 122.

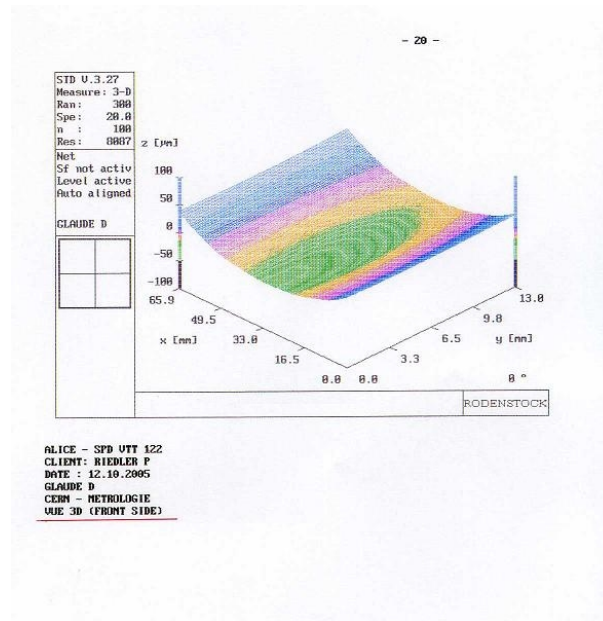


Figure 4.26: The results of the metrology measurements of the sensor side of the SPD ladder 122.

result indicates that the open contacts in the chip corners seem to depend more strongly on the chip bow.

Up top now only ladders (8 in total) containing chips from one RO-wafer were concerned with the open contact problem in the corners of the chips. Tests at the bonding foundry showed that during the reflow the chips and sensor relax into their natural (bowed) state and the bump-contacts can open in case of a too strong bow. This effect might have been caused during the thinning process. The stress relief after thinning might have been incomplete in some areas of the chip. Another cause could be due to mechanical stressing of the readout chips during the dicing process. The feedback from these measurements has been given immediately to the bonding foundry and this effect has not occurred since.

## 4.7 Summary

This chapter deals with the quality assurance and testing procedures of the readout wafers and the SPD ladders. During the last years I have significantly contributed to the development and fine tuning of the quality assurance criteria. At the probe station at CERN I have tested two readout wafers and the first modules of every new delivery batch of SPD ladders in order to be able to give a fast response to the bonding foundry. In collaboration with cooperating institutes in Bari, Padova and Catania, up to now, 53 readout wafers, corresponding to 4558 ALICE1LHCB chips, and 165 production ladders have been tested and qualified. The tests of the readout chips show good yield in the order of 52% class I chips on average. The SPD

ladders show an average yield of 66% with a very good bump bonding yield of less than 1% defect pixels for most chips.

I participated in the study of a temporarily occurring adhesion problem of the aluminum layer on the back side of the sensor. Introducing an additional cleaning and protection step in the sensor wafer production has lead to the solution of this problem. None of the sensors delivered afterwards was affected.

Chips from one readout wafer showed a bowl like shape resulting in open bond-contacts in the corners. I observed this defect during ladder tests and performed metrology measurements in collaboration with the CERN TS-MME group. A fast feedback to the bonding foundry avoided further occurrence in the subsequent production.



## Chapter 5

# Beam Tests and Analysis

### Contents

---

5.1	Beam Test 2003 . . . . .	<b>80</b>
5.1.1	Experimental Setup . . . . .	80
5.1.2	Results . . . . .	83
5.2	Combined ITS Beam Test 2004 . . . . .	<b>93</b>
5.2.1	Experimental Setup . . . . .	94
5.2.2	Offline Analysis within the AliRoot Framework . . . . .	98
5.2.3	Cluster Study - Comparison BT 2003 and 2004 . . . . .	100
5.3	Summary . . . . .	<b>103</b>

---

## 5.1 Beam Test 2003

The ALICE SPD collaboration carried out a beam test from Oct 22 to Nov 8, 2003 on the H4 beam line at the CERN SPS. Two different kind of beams were used to illuminate the SPD modules. A fully stripped In-beam with 158 GeV/A beam energy was extracted onto a 4 mm thick Pb/Sn target, in order to study the tracking with high energetic particles in a high multiplicity environment. And a proton beam with an energy of 120 GeV/c was used to directly illuminate the SPD planes. The aim of this experiment was the study of the tracking precision of the SPD under different conditions (threshold and inclination angle). During this beam, also a full readout chain connected to two ladders (PCI 2002 - Pixel Chip Interface) was investigated for the first time in a particle beam. The analysis described in this chapter is mainly based on the data taken during the proton beam runs.

### 5.1.1 Experimental Setup

In the beam area a solid granite/metal experimental table could be moved on rails and was fixed centrally with the beam pipe. On this table all planes including the PCI 2002, scintillators and the target were mounted. For position and angle scans the middle plane was mounted on a remotely controlled XY-table. It could change the position of the assembly horizontally and vertically and the tilt could be varied from  $0^\circ$  to  $45^\circ$ .

#### Modules

The basic configuration during the beam test was to use four reference planes (0, 1, 3 and 4) to define the tracks and then project the found tracks into the middle plane (2) which was the plane under study. Each two of the tracking planes were connected in parallel to each other to form a doublet and were read out with one Pilot Module. An additional plane (PCI2002) was introduced that contained a full prototype readout chain of two ladders. The reference planes carried single chip assemblies with either 200 or 300  $\mu\text{m}$  thick sensors. The plane under study itself had a 300  $\mu$  thick sensor.

One purpose of the beam test 2003 was to study the tracking of secondaries and the behavior of the SPD assemblies in higher multiplicity environment. This was done by introducing a target during the heavy ion runs in front of the SPD planes and by choosing a beam-off alignment as indicated in drawing 5.1. This adjustment was changed several times with the aim to improve tracking and correlations between the different planes. In Appendix B all geometrical setups are shown. The average multiplicity amounted to around 8 tracks in the SPD planes per event.

For the  $p^+$ -beam all planes were put directly into the beam without a target. The aim of these measurements was to compare with the results obtained in beam test 2002, when the plane under study had a 200  $\mu\text{m}$  thick sensor. Further, by configuring the two doublets used as tracking planes in the crossed geometry, an improvement in the resolution also for the direction with

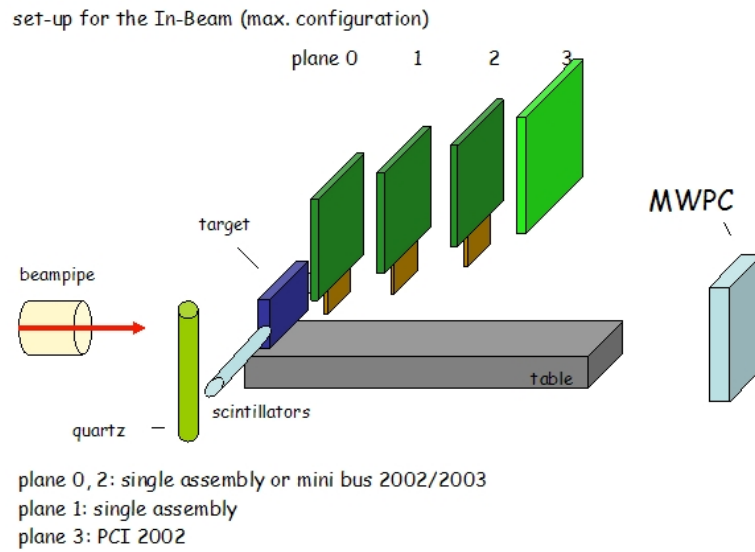


Figure 5.1: An illustration of the experimental setup for the heavy ion beam runs [68]

the larger pixel cell width was hoped to be obtained. The two axes of each doublet were set at  $90^\circ$  with respect to each other, as it can be seen in Figure 5.2. With this configuration, a good tracking precision was obtained ( $\sim 10 \mu\text{m}$  both in x and y direction, see chapter 5.2.2).

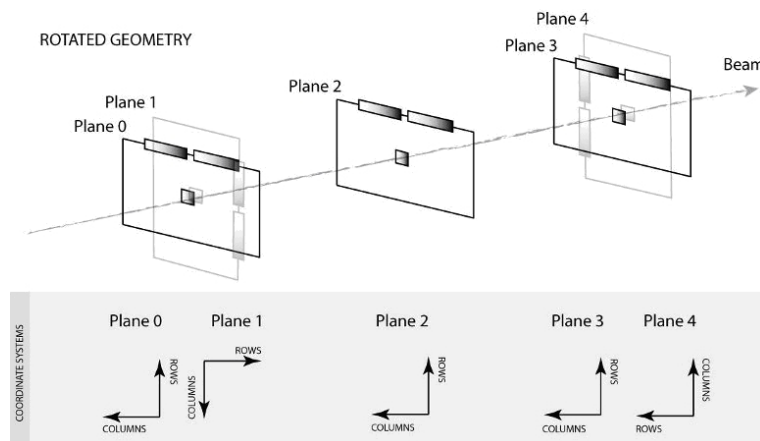


Figure 5.2: Crossed geometry for the proton beam with the offline nomenclature (plane 0 to 5 instead of plane 0 to 3) [69]

## Trigger

The trigger system for the heavy ion runs was built out of a quartz counter, which was positioned into the beam in front of the target. The trigger signal was generated in coincidence with a 2 cm x 2 cm scintillator, which was registering secondaries coming from the target. Figure 5.1 shows the positions of these modules. In order to avoid the spreading of the beam, the quartz counter was installed some 20 to 30 meters upstream, where it could be moved with an XY-table. In this way, the triggers were only generated by parallel incoming particles. After the setup a MWPC (Multi Proportional Wire Chamber) provided the information for beam steering.

In the proton run configuration, the target was removed and the scintillator was positioned centrally into the beam to provide the trigger signal in coincidence with the quartz counter.

## PCI2002

For the first time a full read-out chain (PCI 2002) was tested in a particle beam. PCI 2002 also used its own VME-crate as it was not possible to implement it in the main crate due to a different card design. Because the data it creates has a different format, special software had to be created to be able to merge it with the data from the other three planes. This could be performed successfully and track correlations have been observed. Figures 5.3 and 5.4 represent a picture of the PCI 2002 and the hitmap visualized on the screen by the data taking software.

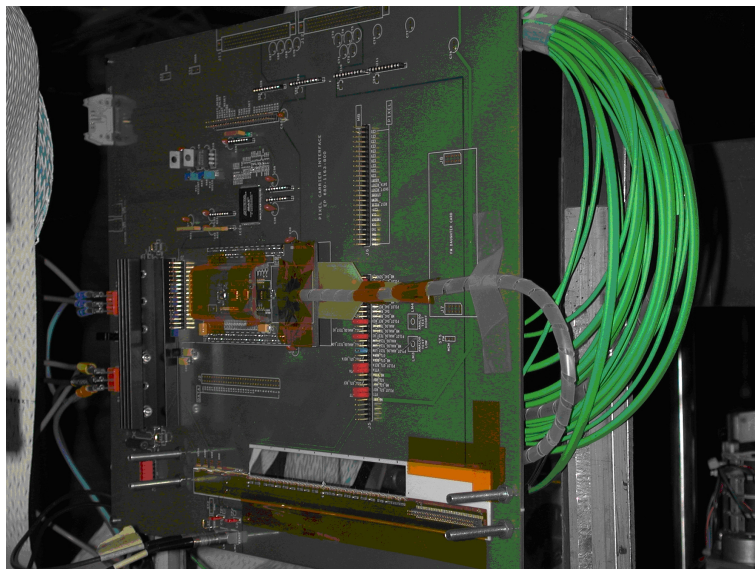


Figure 5.3: Picture of the PCI 2002. The half-stave and the MCM can be seen.

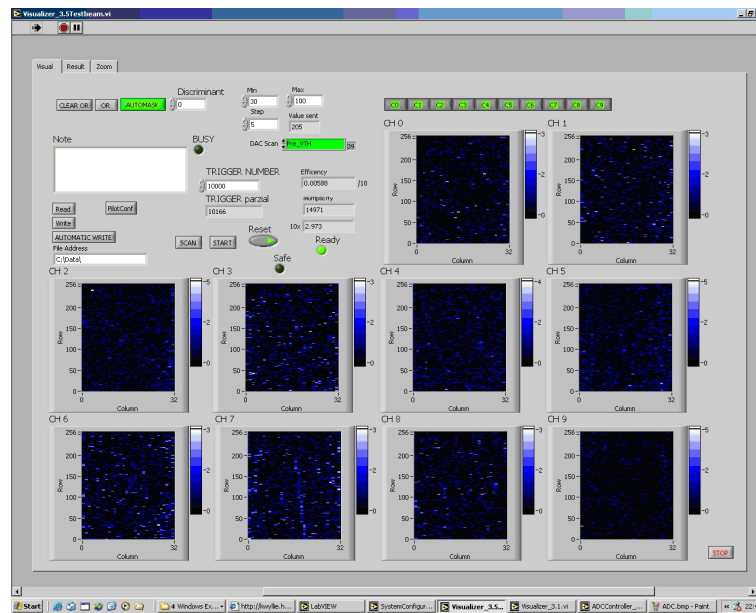


Figure 5.4: Hitmap of all 10 chips of the PCI2002 visualized with the online monitoring software.

### 5.1.2 Results

In the data format from the ALICE SPD DAQ system the hits were written in words containing the hardware address and column and row number. The raw data are processed offline to produce a ROOT-tree with event based information. The analysis software is a complete stand-alone C++ package. The decoding and the analysis part of the converting software are decoupled. This was done for two reasons: First, the decoding part of the software, involving event sorting, noisy pixel removal and clustering, only needs to be done once, and second, the tracking, performed in the analysis part of the software, could be performed in an extra routine allowing an more flexible study of the alignment. A cluster is by definition either a single fired pixel or a group of fired pixels, each of them being adjacent to at least another one. For each event, the cluster finding algorithm computed the number of clusters in each plane, the cluster size and the dimension in the X and Y direction.

In the case of the proton beam the track reconstruction was very simple since no target was used and the tracking planes were placed directly in the beam. One event usually consisted of a single particle traversing the setup, leaving a low probability for any ambiguities.

### Data Quality Checks

A systematic study of the data and of the different geometry configurations used during the beam test was performed. A method based on correlation functions was developed to evaluate

the residual misalignment of the 5 pixel planes. The principle of this method is to assign the row and column of a single hit from one plane to another. A straight line, as shown in Figure 5.5 will indicate correlation between two planes. Using this method the data could be qualified in terms of possible tracking.

Due to problems with the buffer in the pilot modules, which occurred during the proton beam runs, the data from different planes were event shifted. This means that hits from different planes were not written in the same event. Using the correlation method, this effect could be found and corrected if the event shift happened in between two runs. An event shift occurring in the middle of the file could not be cured and the data could not be used for further analysis ( $\sim 5.5\%$ ). In Figure 5.6, such an event shift is visualized as the residual of the projected to the real hit in plane 2 in the X and Y direction. The event shifts were calculated for all files and have been made available on the homepage for the SPD offline community.

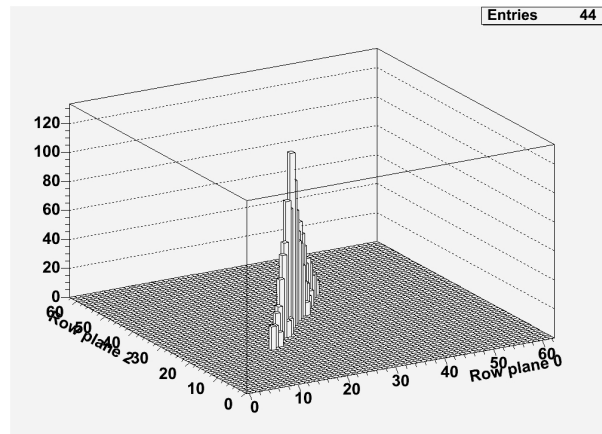


Figure 5.5: The straight line indicates correlation between the planes 2 and 0 in the focused proton beam runs. A cut was performed on the data requiring at least two entries in the correlation histogram.

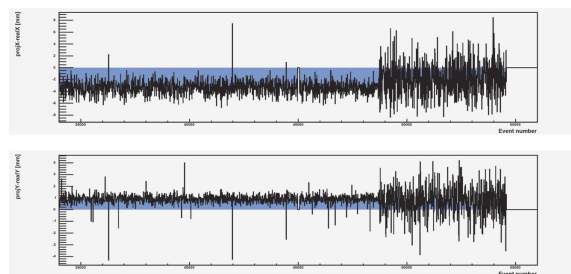


Figure 5.6: Histogram showing the occurrence of event shifts in the middle of one file.

## Alignment

During the proton beam runs, two different beam settings were used to illuminate the SPD planes. On the first day, the wide beam setting was used, while on the second day, the beam was focused to an ellipsoid cone with the first diameter of around 5 mm and the second diameter if around 3 mm. For the focused beam, the alignment of the planes was performed using the center of the beam profile. In the wide beam setting, this method could not be used and for this reason an new alignment algorithm taking the tilt and the azimuthal angle into account was developed. For the alignment procedure the raw data was converted to the global coordinates system showing the plane and the X and Y values of each hit with respect to a reference point.

During the data conversion, a cut on the data requiring only one hit per tracking plane was performed to allow a better tracking. Using special trigger conditions (see chapter on trigger), only parallel tracks were selected allowing thus a more precise tracking.

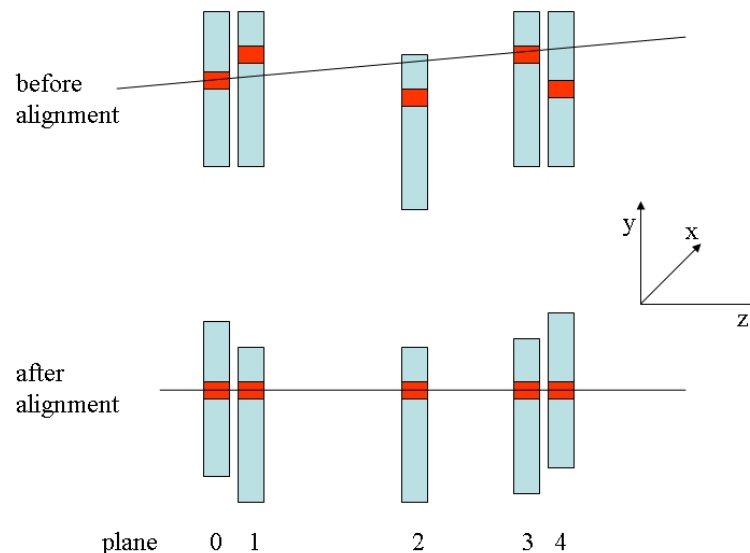


Figure 5.7: Illustration of the offline alignment procedure of the 5 SPD planes.

The alignment of the planes is illustrated in Figure 5.7. In order to align the planes to each other, the planes were aligned preliminary without tilt and azimuthal correction to allow tracking and calculation of the resolution on the plane 2. For this, the plane 0 was set fixed and the coordinates of the hits in this plane were set to zero. Due to same geometrical orientation as in the plane 0, the plane 3 was chosen to be the second fixed point (see Figure 5.2). The residual of the hits in X and Y direction between the planes 3 and 0 for each single event was plotted in an histogram to calculate the offset of the plane 3 with respect to plane 0. While the residuals in the Y direction of the 3<sup>rd</sup> plane follow a Gaussian distribution and can be easily fitted, the residuals in the X direction do not due to the longer pixel cell length and such less fine segmentation. The residuals of the plane 3 in both directions are plotted in Figure 5.8 and the calculated offset

was used to correct the hit coordinates in the plane.

In the next step, the offset of the planes 2 and 4 were calculated in the same manner and the planes were aligned accordingly. In the last step, all 4 tracking planes were aligned and used for the tracking to project a hit into the plane under study (plane 2). By projecting a reconstructed track into the middle plane and then searching for the nearest hit, the widths of the residual distributions could be evaluated.

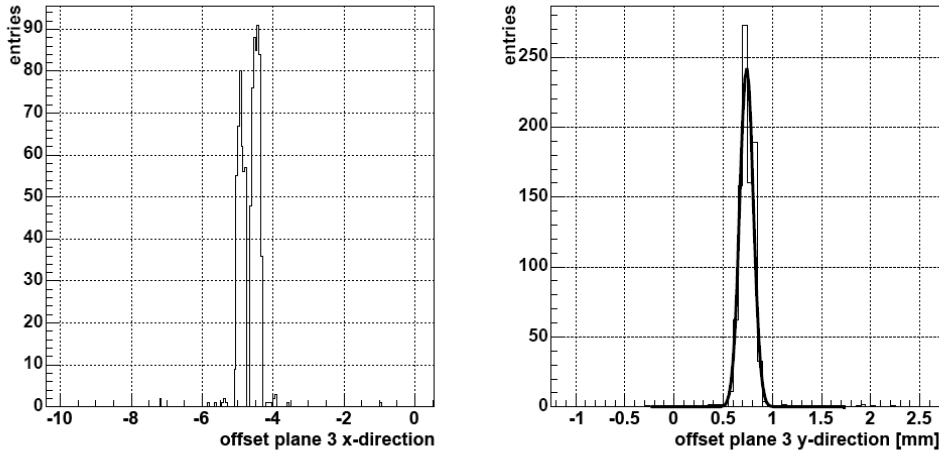


Figure 5.8: Results of the calculation of the offset for the plane 3. The residuals in Y direction were fitted with an Gaussian to give the mean offset with respect to plane 0. The double peak in the X-direction is due to different global coordinates in the case of hits with cluster size 1 and 2.

Utilizing this preliminary alignment and the width of the residual distribution, a possible azimuthal rotation was studied. For this the azimuthal angle was scanned from  $-0.1$  to  $0.1$  rad in steps of  $0.01$  rad. The hits in the scanned planes were corrected for each azimuthal step using the rotation matrix:

$$\begin{pmatrix} x' \\ y' \end{pmatrix} = \begin{pmatrix} \sin & \cos \\ \cos & -\sin \end{pmatrix} \cdot \begin{pmatrix} x \\ y \end{pmatrix} \quad (5.1)$$

In the first scan, only the azimuthal angle for the planes 3 and 4 was scanned. The planes 3 and 4 were treated simultaneously since they were mechanically fixed to each other in a doublet. In the next step the azimuthal angle of the plane 2 was scanned. At each step the resolution of the tracking in plane 2 was recorded and the results are plotted in Figure 5.9. This way, the azimuth angle at which the smallest width of the residual distribution in plane 2 could be found and the planes could be corrected for this azimuthal orientation. The planes 0 and 1 were set fixed with respect to the azimuthal angle. The results of the azimuthal angle scan are shown in Table 5.1. Only the planes 3 and 4 were rotated with respect to the plane 0. For the plane 2 no azimuthal

orientation could be found.

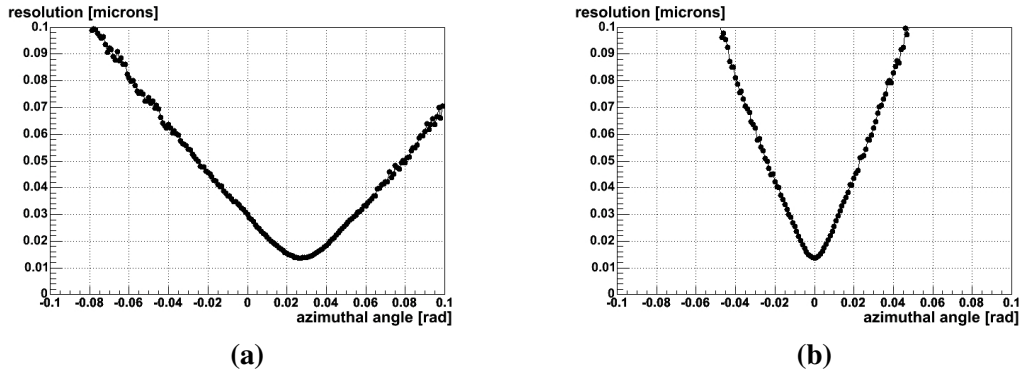


Figure 5.9: (a) The width of the residuals in the plane 2 are plotted for different azimuthal angle corrections of the planes 3 and 4. (b) After the azimuthal correction of the planes 3 and 4 the azimuthal angle of the plane 2 was scanned to find the minimum residual.

tilt angle - plane 2	azimuthal angle for plane 3(4) [rad]
0°	0.027
10°	0.029
20°	0.028
30°	0.024
40°	0.023

Table 5.1: Results of the azimuthal angle scan for the planes 2 and 3(4).

The tilt angle of the planes 2, 3 and 4 with respect to the plane 0 and 1 could be calculated directly. This was done by plotting the residuals of the plane in X and Y direction against the X resp. Y coordinate of the plane 0. An existing tilt angle would cause a change of the residual of the hit position between two planes depending on the X resp. Y coordinate of the hit in one of the planes. Figure 5.10 illustrates this method. The residuals of each single event is filled in an histogram resulting in an linear distribution, which is then fitted. Using the slope  $k$  of the fit the tilt angle could be calculated using the following formula:

$$k = \cos \varphi \quad (5.2)$$

Since the planes 1, 2 and 3 had the same geometrical orientation, the tilt of the planes 2 and 3 was calculated with respect to the plane 0. The planes 3 and 4 were treated as one due to the mechanical connection to a doublet and therefore the tilt of the plane 4 was set to the calculated value of the plane 3. In Figure 5.11 the output of the tilt angle calculation is shown for the plane 3 and in Table 5.2 the calculated tilt angles of the planes 2 and 3(4) are shown for different run conditions (inclination of the plane under study).

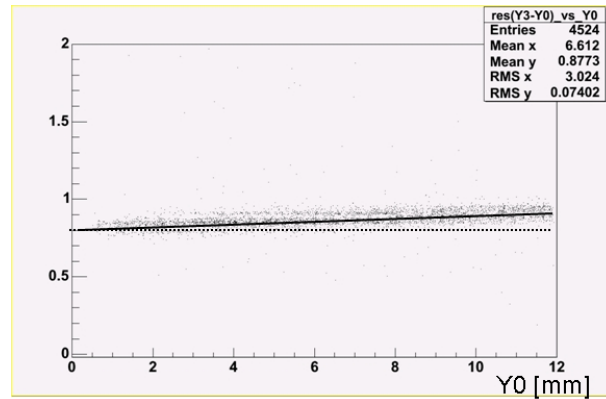


Figure 5.10: Illustration of the tilt angle effect on the residuals. Depending on the coordinate of the hit position in the pixel matrix, the residual between the planes changes.

### Hit position difference in X and Y direction

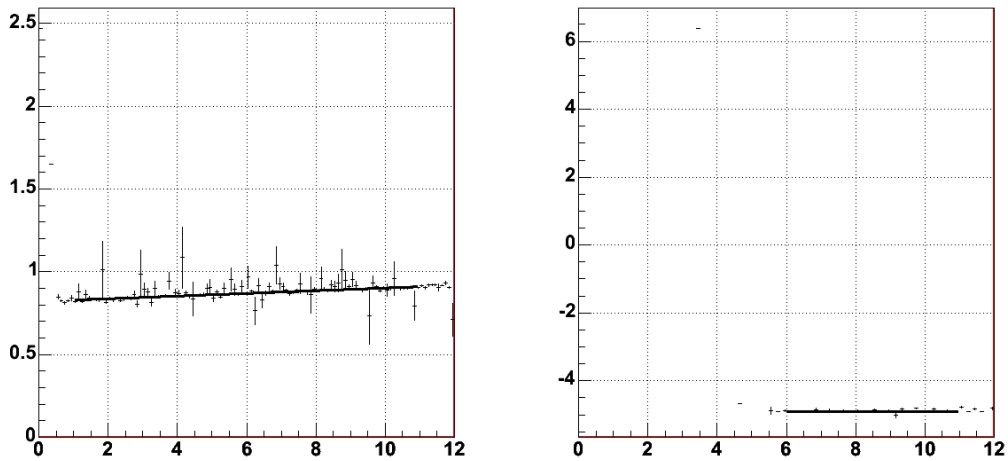


Figure 5.11: Result of the tilt angle calculation for the plane 3 with respect to the plane 0.

tilt angle plane 2	tilt angle for plane 2 [rad]	tilt angle for plane 3(4) [rad]
0°	0.138	0.35
10°	10.127	0.204
20°	20.222	0.313
30°	29.914	0.425
40°	39.588	-0.082

Table 5.2: Results of the tilt angle calculation for the planes 2 and 3(4).

Using the results from the azimuthal and tilt angle calculation of the planes 2 and 3(4), the final alignment could be obtained. For this, the coordinates of the hits in the planes 2 to 4 are corrected for the azimuthal angle and tilt rotation. The alignment procedure is performed in the same way as for the preliminary alignment. The results of the plane alignment in X and Y direction is shown in Figure 5.12.

### Resolution Study

After plane alignment, the resolution of the plane under study could be calculated. For this, the beam track is reconstructed with a best fit method through the space points in the tracking planes (the two doublets). The position errors of the hits include multiple scattering in the different layers of the 5 planes. By projecting the reconstructed track into the middle plane and then searching for the nearest hit, the widths of the residual distributions could be evaluated. The residuals are partly due to the intrinsic detector resolution and partly due to the precision of the reconstructed track. To give an order of magnitude, we expect in the case of binary readout with hits of cluster size one, that  $\sigma_x = 425 \mu\text{m}/\sqrt{12} \approx 122.7 \mu\text{m}$  and  $\sigma_y = 50 \mu\text{m}/\sqrt{12} \approx 14.4 \mu\text{m}$ . In reality  $\sigma_y$  will be less due to charge sharing, while this is less likely in the longer pixel direction. Clusters in the test plane are then tagged as belonging to the track if they are within a radius of  $100 \mu\text{m}$  of the projected hit, corresponding to  $\approx 7 \sigma$  of the binary resolution. Figure 5.13 shows the total residual distributions for both directions of the SPD assembly under study. The tracking error on a linear track fit is given by calculating the inverse matrix which has as components the second derivatives of the least square function with respect to the track parameters. To facilitate the problem, the tracking lanes was set at  $z = 0$  and thus the estimate of the tracking error reduces to estimating the error in the fit parameter  $b$ :

$$\sigma_{tracking} = \sigma_b \quad (5.3)$$

Using the defining coefficients of the least square fit method from [70]:

$$A = \sum_i \frac{x_i}{\sigma_i^2} \quad B = \sum_i \frac{1}{\sigma_i^2} \quad C = \sum_i \frac{x_i^2}{\sigma_i^2} \quad (5.4)$$

the error in the parameter  $b$  is given by:

$$\sigma(b) = \frac{C}{BC - A^2} \quad (5.5)$$

Figure 5.13 shows the total residual distribution for both directions of the plane under study. The tracking error was calculated to be  $10.19 \mu\text{m}$ . The intrinsic resolution of the detector can be obtained by subtracting quadratically the tracking resolution from the  $\sigma$  of a Gauss fit to the residual distribution:

$$\sigma_{intrinsic}^2 = \sigma_{residual}^2 - \sigma_{tracking}^2 \quad (5.6)$$

This formula holds exactly in the case of convolution of two Gauss functions and is due to the flat distribution of the tracking resolution, only an approximation. The intrinsic resolution

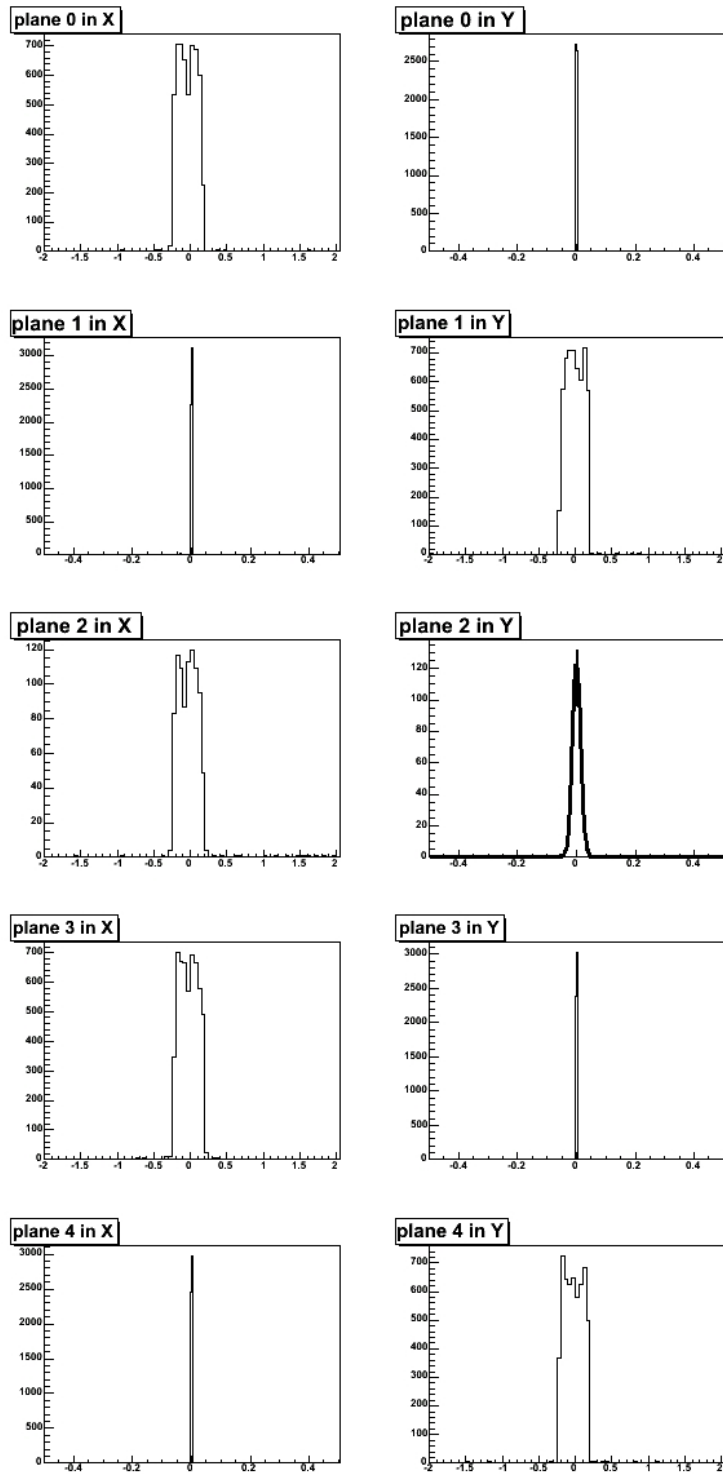


Figure 5.12: Results of the alignment procedure. The histograms to the left show the alignment in X and the ones to the right in Y direction. The units of the histograms are as follows: plotted in X-axis, the mean difference of the corrected and projected hits and in the Y-axis the entries.

### Spatial resolution of the plane under study in X and Y

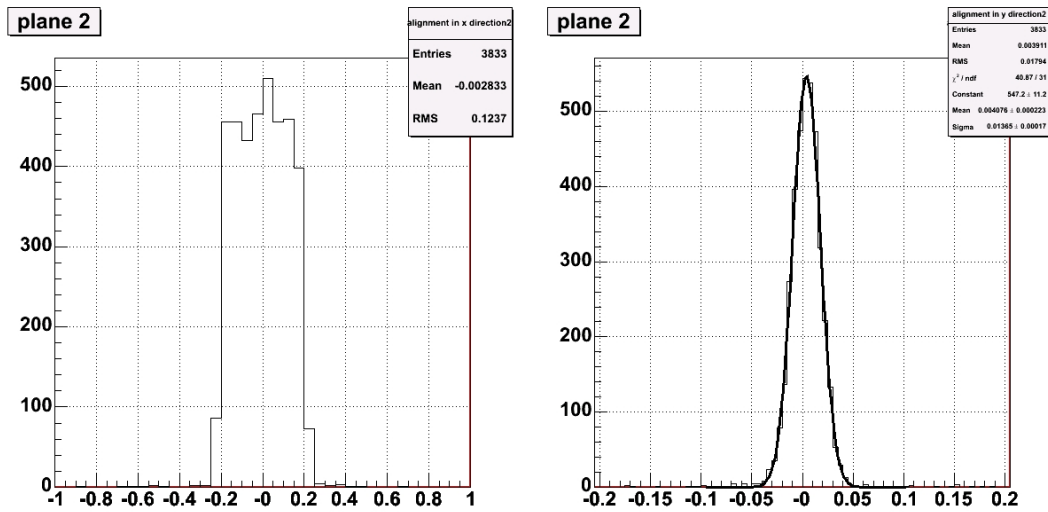


Figure 5.13: Obtained spatial resolutions after the alignment for the plane under study (plane 2) under a tilt angle of 0. The resolution amounts to  $135.5 \mu\text{m}$  in X-direction (left) and  $13.95 \mu\text{m}$  in Y-direction (right).

can be such calculated and amounts to  $8.3 \mu\text{m}$ , which is in good agreement with the estimate obtained in [64]. There, the intrinsic resolution is calculated for the 1-pixel cluster ( $8.9 \mu\text{m}$ ) and for two pixel clusters ( $8.2 \mu\text{m}$ ).

The quality of the tracking is reflected in Figure 5.14, where the  $\chi^2$ -distributions in both projections are shown. Moving one reference plane slightly affects the  $\chi^2$ 's dramatically. This would suggest a good alignment and thus, small contribution from the alignment error to the tracking error.

In Figure 5.15 the development of the resolution in Y direction ( $50 \mu\text{m}$  pixel length) is plotted for different threshold settings at 0 tilt angle of the plane under study. At higher thresholds (close to DAC setting of 150) the sensitive area of the pixel cell becomes very small and such the charge sharing becomes less probable. This results in a higher resolution in the case of 1-pixel clusters. With a lower threshold, the charge sharing increases and the resolution for 1-pixel clusters decreases. The resolution in the case of 2-pixel clusters increases at very low thresholds (DAC setting of around 200) due to the increase of the charge sharing area and such the increase of the effective pixel size. Combining the two main pixel cluster topologies one obtains a minimum in the resolution curve at threshold DAC setting of 200 (Figure 5.16), which corresponds to approx. 2700 electrons (see chapter 6).

In Table 5.3 the resolutions for different track incident angle on the plane under study are shown for the wide and focused beam settings. The higher resolution at track incident angle of angle 10 can be explained with the particular geometry of the  $300 \mu\text{m}$  thick sensor. The optimal

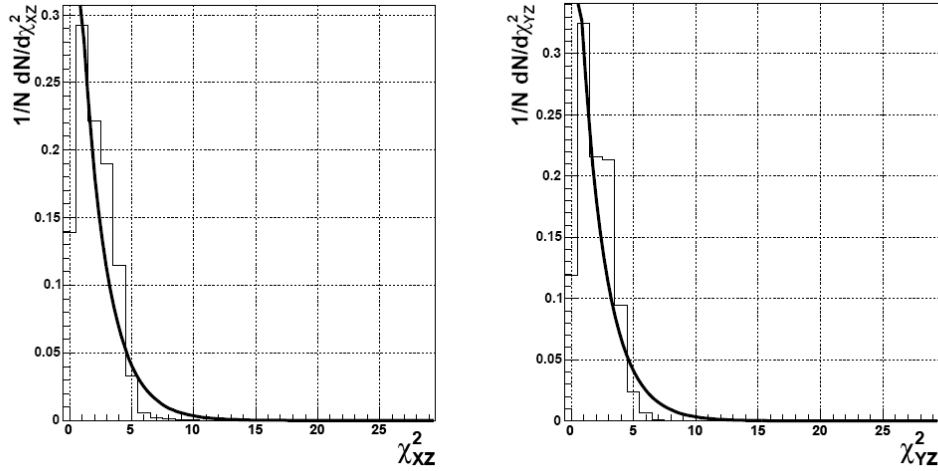


Figure 5.14:  $\chi^2$ -distributions in X (left) and Y-direction (right) respectively. The laid in functions are the theoretical  $\chi^2$ -distributions for the two degrees of freedom.

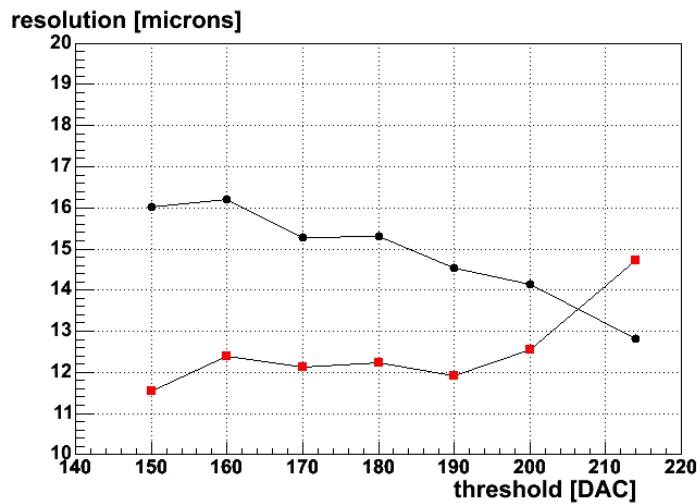


Figure 5.15: The resolution along the Y coordinate for normal track incidence angle samples as a function of the threshold and separately for cluster topology 1 (squares) and 2 (discs). The connection lines are to aid the eye.

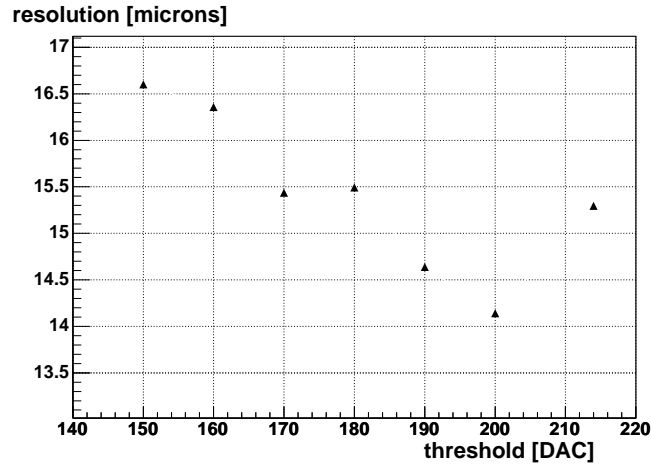


Figure 5.16: Resolution of the two main cluster topologies combined as a function of the threshold. Increasing DAC setting corresponds to decreasing threshold.

precision for this angle is reached at a DAC threshold setting of 160, which is far away from the region of interest (see [71]). The other resolution values do not differ much from each other and the agreement is within the errors.

tilt angle plane 2	defocused beam]	focused beam
0°	13.64	14.41
10°	16.52	16.51
20°	14.6	14.88
30°	15.53	14.87
40°	15.91	16.04

Table 5.3: Results of the tilt angle calculation for the planes 2 and 3(4).

## 5.2 Combined ITS Beam Test 2004

The Inner Tracking System (ITS) of the ALICE Experiment, including the subdetectors Silicon Pixel Detector (SPD), Silicon Drift Detector (SDD) and the Silicon Strip Detector (SSD), performed an joint beam test in the north hall of the CERN SPS accelerator from Oct 29th to Nov 15th 2004. Mainly a positive beam (55%  $\pi^+$ , 40% p, 5%  $K^+$  at production) with a 3 days negative beam ( $\sim 100\%$   $\pi^-$ , fraction of  $K^-$  at production) was used to illuminate the ITS planes. The momentum of the beam amounted to 120 GeV/c and the beam profile was almost Gaussian

with a base of about 2 - 3 cm in x and y. The beam focus was set a few meters downstream of the setup.

### 5.2.1 Experimental Setup

Figure 5.17 shows the setup of the joint beam test. The first two planes seen from the beam direction were two half-staves of the SPD followed by two units of the SDD and the SSD.

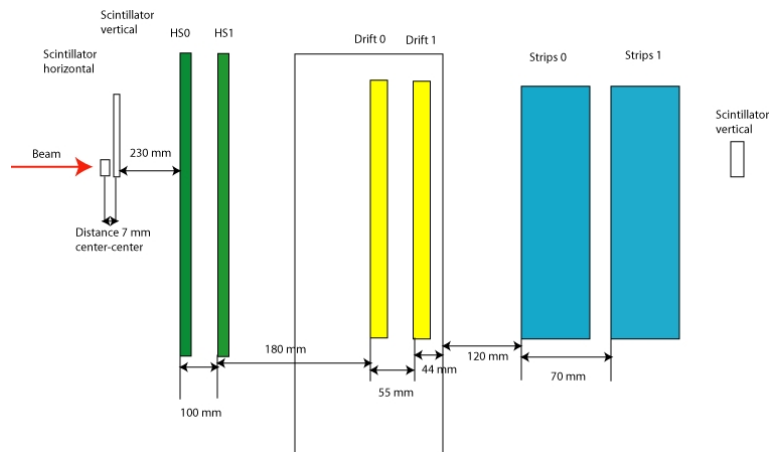


Figure 5.17: The geometrical setup used during the joint beam test 2004. [72]

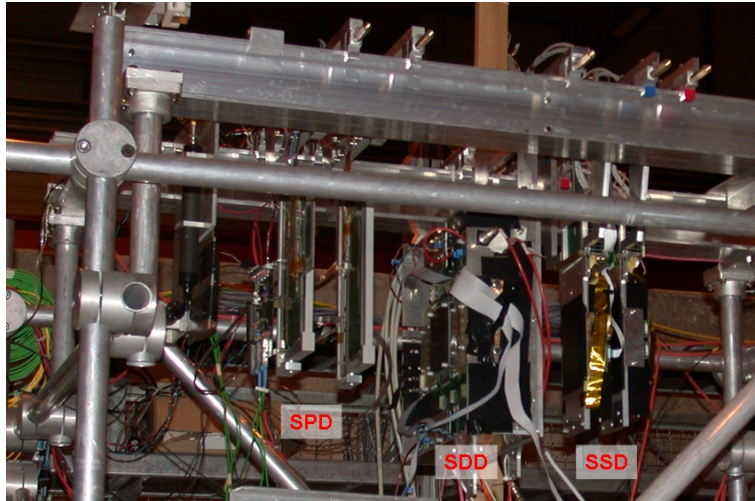


Figure 5.18: Picture of the experimental setup in the joint beam test 2004. [73]

The motivation for the joint beam test was to investigate for the first time the final DAQ- and control-chain of the ITS subdetectors. After the installation in the beam area, the first beam

steering took place. Following this, the SPD planes were aligned mechanically to show the first beam spots. Due to initial problems with the DAQ no data could be written in the first few days. But since the online software was working properly, SPD stand alone runs could be performed allowing noise runs, runs with beam and delay scans. All the data from the initial phase had to be taken in the single event mode due to problems with the multi-event buffer in the SPD-Link-receivers. This problem has been solved later in the beam test.

### ITS Modules

Each subdetector was represented with 2 planes put in the same order as in the final experiment. The SPD used two half-staves in the final configuration as they will be used in the ALICE experiment (see Figure 5.19 (a)). Each half-stave consists of two ladders readout via an MCM. One SPD Router with two link-receivers merged the data and sent it through the Digital Data Link (DDL). A more detailed description of the final SPD readout and control chain can be found in chapter 3.

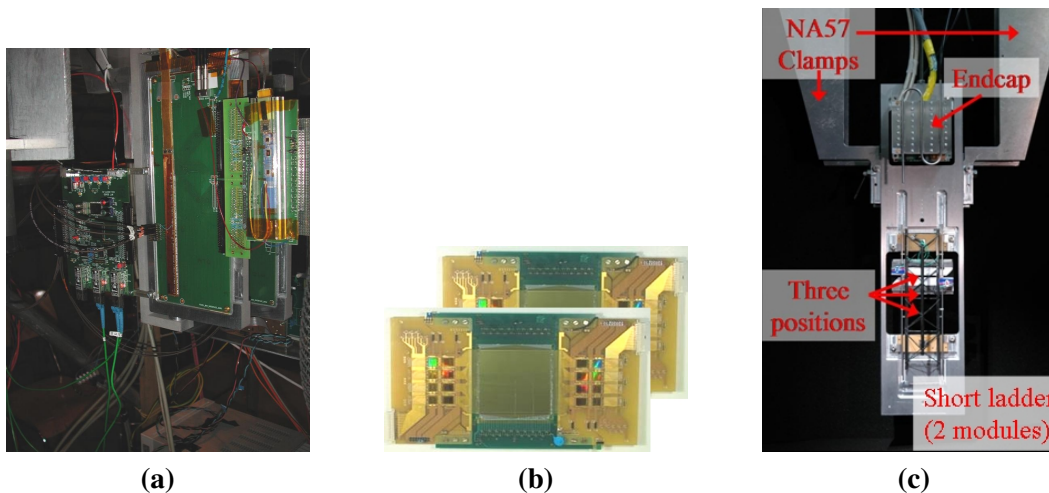


Figure 5.19: (a) The two SPD half-staves used in the joint beam test 2004. (b) The two SDD planes used in the joint beam test 2004. (c) The SSD module with the endcap. [73]

For the SDD planes, two production detectors fully equipped with four PASCAL (front end electronics) and AMBRA (event buffer) chips were used for the beam test [73] (see 5.19 (b)). The low voltage power was supplied via an AremPRO unit. The readout was performed via the so called CARLOSrx chip, which together with the trigger unit TTCrm was embedded in the CARLOS box. In forefront of the beam test, the SDD readout chain has been tested in an 16 hours run with the DDL and trigger system producing no errors in the data (in single buffer mode).

The SSD modules used in this beam test consisted of two short ladders with 2 modules each. The readout was performed via 2 endcaps connected to the readout system via the prototype

patchpanel. A VME based unit called FEROM served as the interface to the DAQ, the trigger and the DCS. All parts of the SSD system were according to the final design. While the channel noise of the SSDs was in acceptable range, the common mode noise was too big. This affected the zero-suppression and was investigated independently after the beam test.

### Data Acquisition System

During the common beam test, the data could be written in a standalone mode for individual detectors. This was essentially important for the startup of the beam test in order to simplify the debugging process. For this, the data was taken with independent triggers and independent control without event building. In the common runs, the data for all 3 subdetectors or any combination of two subdetectors was taken with a common trigger system. The event building was performed based on orbit counter and bunch crossing event identification. All data recorded was stored on a local disk and later transferred to the CASTOR system at CERN.

The DAQ system was built up as follows: Once triggered, each subdetector would send the data via the Detector Data Link (DDL) to its Local Data Concentrator (LDC). The LDCs receive the data via the PCI boards called ReadOut Receiver Cards (RORC). At this beam test two different versions of RORC were used: D-RORC (d standing for DAQ) for the SPD and pRORC (p meaning PCI) for the SDD and SSD. The function of the RORC is to perform concurrent and autonomous DMA transfer into the PC's memory with minimal software supervision. The LDC transforms the fragmented data from different RORCs into subevents and ships them via a fast ethernet connection to the Global Data Collector (GDC). The GDC performs the event building and stores the data on local disks. On an independent control machine 4 DAQ run control processes were running permanently: one for each subdetector and one for the global DAQ. The access to the machine could be gained by using interface panels from any DAQ machine. The resolution of the access conflicts was managed by the Experimental Control System (ECS) on this machine.

DATE v5.0 (Data Acquisition and Test Environment) was used to perform the data acquisition activities. It was controlled by the ECS running on the GDC. It allows multiple parallel Data Acquisition tasks. For the first time the subdetectors could be read out using the same version of the readout. The event building was based on information taken from the Common Data Header. DATE allowed the operator to centrally control the operation of all the machines involved in the data acquisition. For this, an interactive program could be run at the LDC and GDC level. The operating system for all the detectors had to be Linux.

The SPD modules could also be controlled and monitored by a LabVIEW based software running on an independent Windows-PC. The communication with the SPD modules was performed through a VME bus. A separate computer was used for the Detector Control System (DCS) providing the low and high power supply to the modules. A schematic setup of the independent SPD control and monitoring system and the SPD trigger is shown in Figure 5.20 (b).

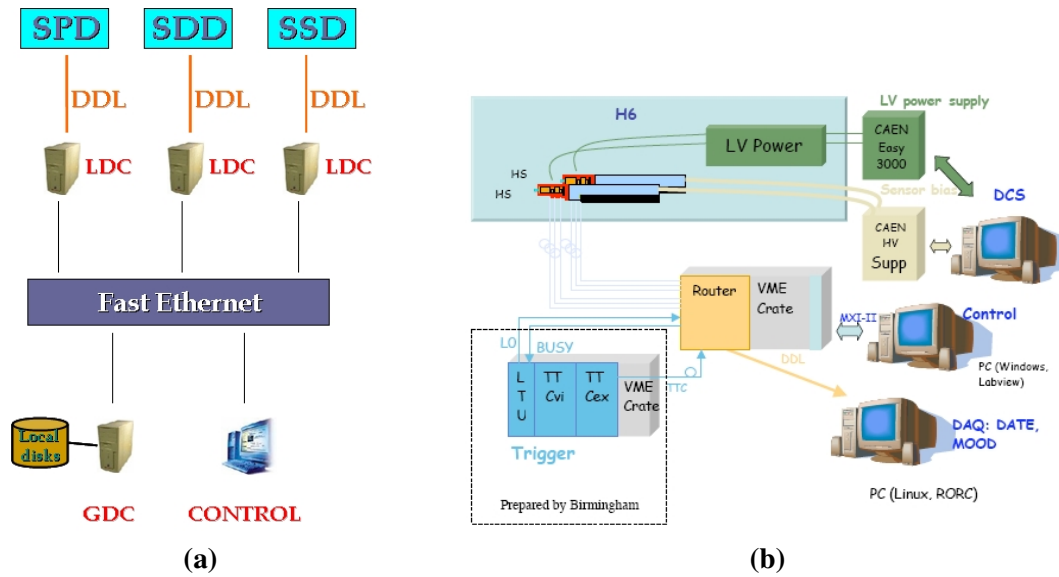


Figure 5.20: (a) Schematic layout of the DAQ used in the joint beam test 2004. [73] (b) Schematic layout of the SPD DAQ and the detector control setup. [74]

## Trigger

One of the purposes of the joint beam test 2004 was also to investigate the implementation of the final trigger system into the DAQ process. As the default trigger, the coincidence between two crossed scintillators ( $1 \times 1 \text{ cm}^2$ ) located upstream and one downstream scintillator ( $2 \times 2 \text{ cm}^2$ ) was used. Part of the data has been taken with a steel-Cu target placed just before the first SPD plane. For this configuration, the downstream scintillator was replaced by a  $20 \times 20 \text{ cm}^2$  one in order to cover the diffracted tracks. For the most of the target program the trigger was provided by the FastOr signal from the SPD planes (instead of the upstream scintillators) in coincidence with the signal from the downstream scintillator. The positions of the scintillators are illustrated in Figure 5.17.

The coincidences coming from the scintillators were passed to the Local Trigger Units (LTU), where the trigger signals were generated. Three LTUs (one unit per each subdetector) were placed in the local trigger crate (see Figure 5.21 (a)). A simplified block diagram of the LTU is shown in Figure 5.21 (b). The LTU software allowed to switch from a common (triggering of the readout of all three subdetectors) to a standalone mode without any recabling. Activating the BUSY2 signal in one of the LTUs, would make this LTU master and the others slaves.

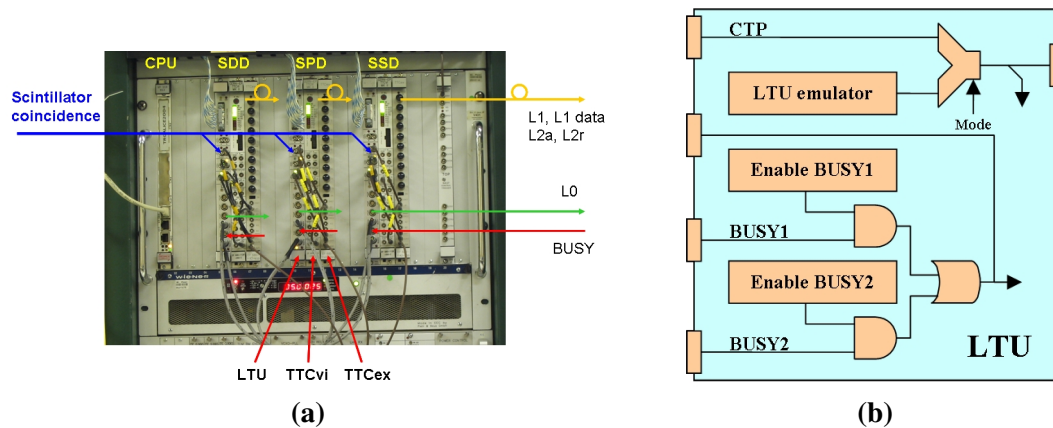


Figure 5.21: (a) Picture of the local trigger crate with the three LTUs. The in- and outgoing signals are illustrated. (b) Simplified block-diagram of the LTU. [73]

### 5.2.2 Offline Analysis within the AliRoot Framework

AliRoot is the ALICE Off-line framework for simulation, reconstruction and analysis. It uses the ROOT<sup>1</sup> system as a foundation on which the framework and all applications are built. Except for large existing libraries, such as GEANT3.21 and Jetset, and some remaining legacy code, this framework is based on the Object Oriented programming paradigm, and it is written in C++. [75] The general scheme of the AliRoot architecture is shown in Figure 5.22.

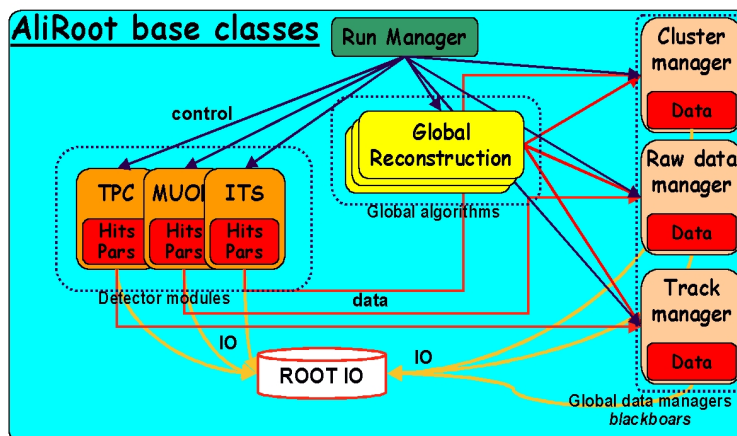


Figure 5.22: General schema of the AliRoot architecture. [75]

The complete beam test analysis from three different stand-alone codes (as used by SPD, SDD and SSD in previous beam tests) was moved to the AliRoot Framework. Thus, a successful

<sup>1</sup><http://root.cern.ch/>

tests of the AliRoot offline software could be performed for the whole ITS. The framework could already be used during the beam test to check for data formats and correlations between the different planes. In Figure 5.23 (a) the correlation between the SPD and the SDD planes is clearly visible, while in 5.23 (b) the correlation is not any more present revealing multievent buffer problem of the SDD. In order to be able to convert the raw data as written by DATE to digits, new classes had to be added to the AliRoot framework. These classes provide for example the geometry of the beam test or algorithms for clustering and removal of the noisy channels. The histogram in Figure 5.24 illustrates the removal of the noisy pixels in the SPD plane.

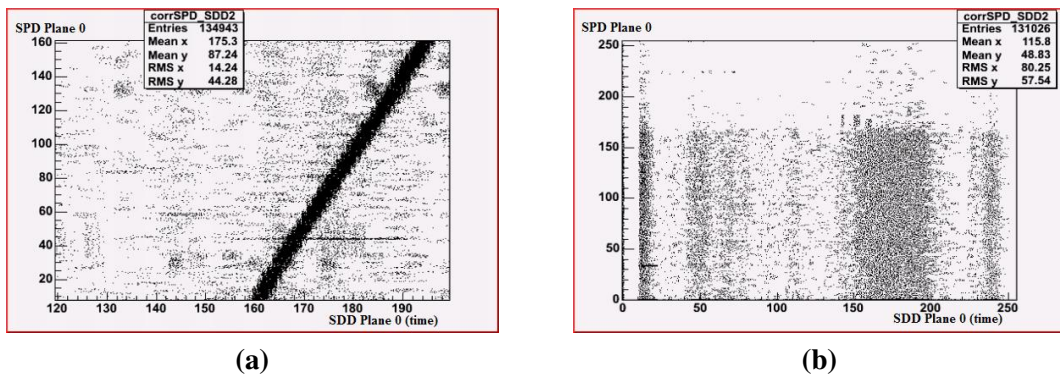


Figure 5.23: (a) Clear visible correlation between the SPD and SDD planes. (b) No Correlation due to multievent buffer problem of the SDD.

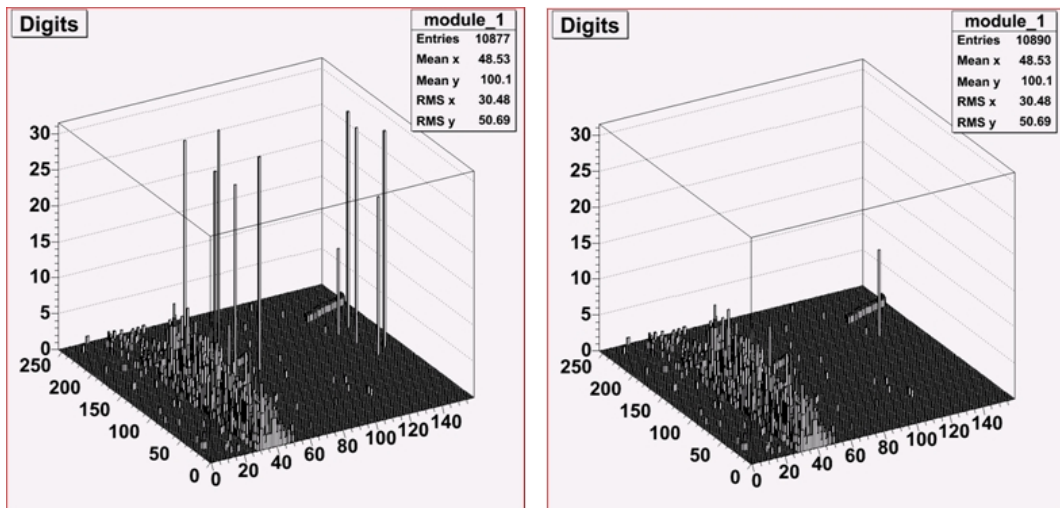


Figure 5.24: Histogram illustrating the noisy channel removal. In (a) the noisy channels are clearly visible, while they are not anymore present after the removal (b). The limited statistics in the noisy pixel histogram is intended to enhance the visibility of the real hits. [76]

The conversion of the raw data to event sorted hit coordinates was done in several steps. With AliITSBeamTest.C the run manager providing the geometry of the different planes was created in the first step. This also created the file galice.root, where the run info was stored (number of events, event header info, pointer to Digits file name). Afterwards the data was converted to root format and with DigitizeBeamTest.C a digits tree was created. In the last step the clustering is performed with TestClustering.C. This will create a root file containing clusters sorted by events. Each cluster will have the size in x and y direction as well as the general size stored in the event branch. This root file was then used for further analysis.

### 5.2.3 Cluster Study - Comparison BT 2003 and 2004

The dependence of the SPD performance as a function of the beam incidence angle has been studied for both beam tests. In the 2003 beam test data samples were taken at 0, 10, 20, 30 and 40 degrees incidence angle with DAC threshold settings of 160, 180 and 200 and in 2004 the SPD planes were tilted to 0, 10, 16, 20 and 30 degrees for 180 and 200 threshold. While in the beam test 2003, the plane under study had a  $300\ \mu\text{m}$  thick sensor, the half-staves used in the joint beam test 2004 were in final configuration ( $200\ \mu\text{m}$  thick sensor). In Figure 5.25 the effect of the detector thickness on the average cluster size in the y direction is schematically shown. As the pixel cells are traversed by a track at three different incidence angles the charge carriers are shared among more pixel cells in case of the  $300\ \mu\text{m}$  sensor resulting thus in larger cluster sizes.

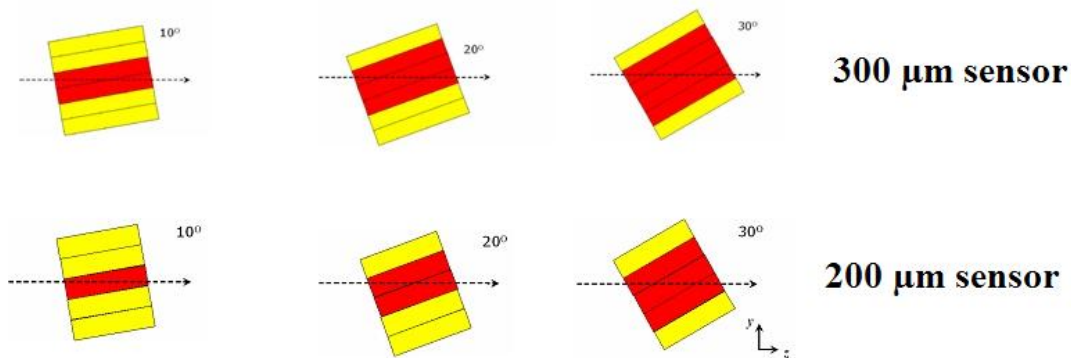


Figure 5.25: Schematic pictures of pixel planes crossed by tracks at different angles in the yz plane for both sensor thicknesses. Pixel cells traversed by the track are shown in red. [71]

The effect of the sensor geometry on the cluster size could be studied in detail using the data taken during the two beam tests. In Figures 5.26 and 5.28 the average cluster size is plotted for different incidence angles and different beam conditions in the beam test 2003. The sensor thickness amounted to  $300\ \mu\text{m}$  in case of all three plots. The first plot shows the average cluster size of the defocused beam and the second and third plot show the average cluster sizes of the focused beam in two corners of the pixel matrix. The three plots do not show a difference in

the average cluster size what indicates a uniform response across the complete pixel matrix. In Figure 5.29 the average cluster size obtained from the beam test data 2004 is plotted as function of the incidence angles. While at  $0^\circ$  the average cluster size is about the same for both detector thicknesses, the difference becomes more obvious with the increasing tilt angle of the planes. In case of the  $300\ \mu\text{m}$  thick sensor, the average cluster size is increasing faster than with  $200\ \mu\text{m}$  as expected from the geometry considerations.

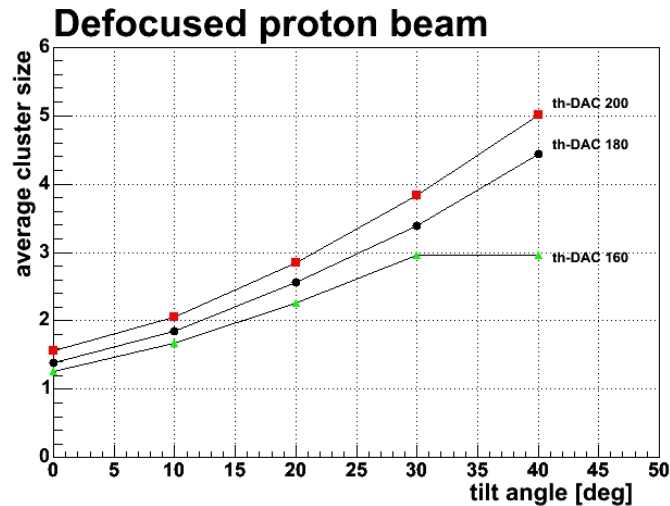


Figure 5.26: Average cluster size as function of the track incidence angle at different threshold settings for the defocused beam in the beam test 2003 ( $300\ \mu\text{m}$  thick sensor).

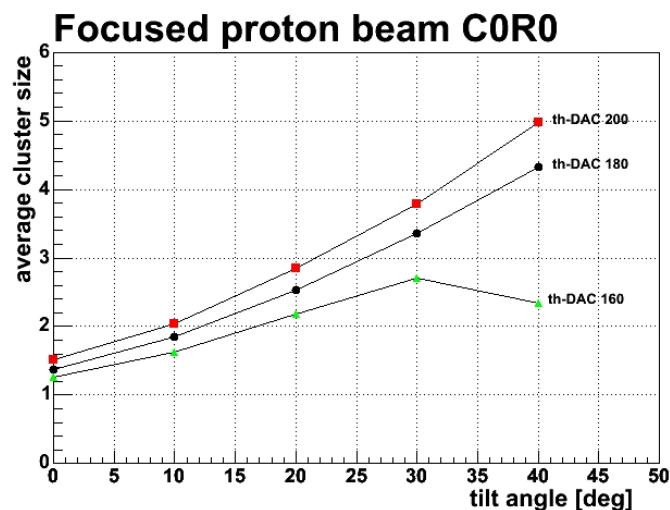


Figure 5.27: Average cluster size as function of the track incidence angle at different threshold settings for the focused beam (corner column 0 row 0) in the beam test 2003 ( $300\ \mu\text{m}$  thick sensor).

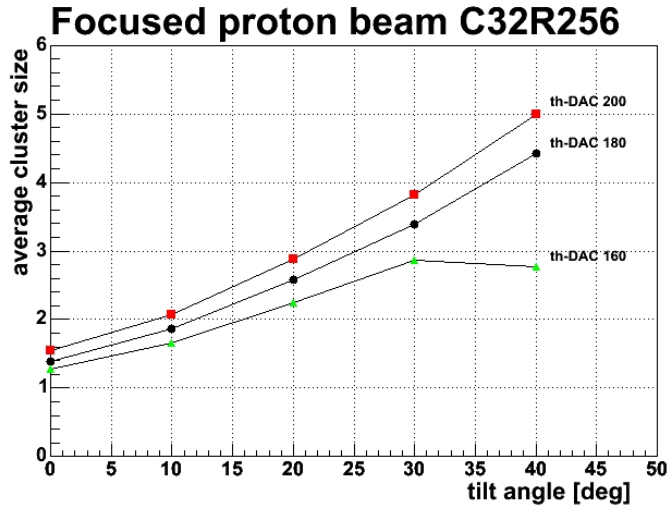


Figure 5.28: Average cluster size as function of the track incidence angle at different threshold settings for the focused beam (corner column 31 row 255) in the beam test 2003 (300  $\mu\text{m}$  thick sensor).

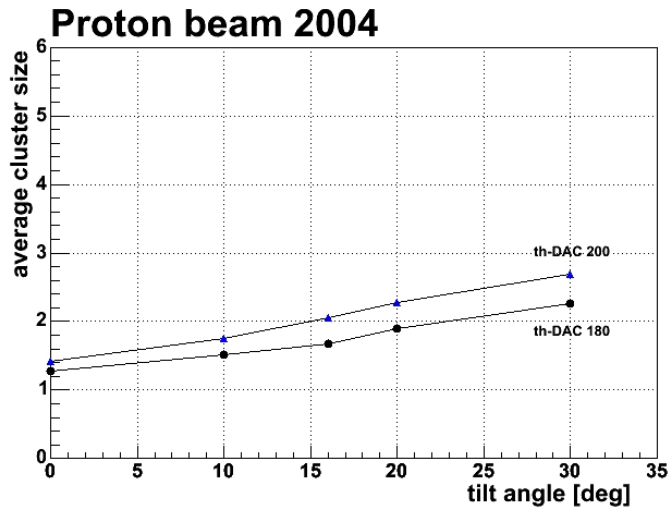


Figure 5.29: Average cluster size as function of the track incidence angle at different threshold settings for the joint beam test 2004 (200  $\mu\text{m}$  thick sensor).

At higher thresholds and at large beam incidence angles another effect could be observed. A high threshold (160 DAC setting) decreases the effective pixel cell size, while the incidence angle shortens the traversing path of the incident particle through one pixel cell. As the result of these two effects, the average cluster size decreases.

### 5.3 Summary

I carried out extensive studies of the ALICE Silicon Pixel Detector performance using data collected in the 2003 and 2004 beam tests. The setup of the beam tests and the architecture of the DAQ and detector control for both beam tests carried out in 2003 and 2004 have been described.

The beam test 2004 data was analyzed within the AliROOT software package, which is the final framework for simulation, reconstruction and analysis.

For the data from the 2003 beam test, I developed a novel alignment procedure. This alignment method takes into account the tilt and azimuthal angle and allows to study also the wide beam settings. The achieved intrinsic resolution of the detector were in the expected range below 10  $\mu\text{m}$  in the 50  $\mu\text{m}$  cell size coordinate. The residual resolution was studied as function of both, the threshold setting and the track incidence angle.

Using self-coded algorithms within ROOT and AliROOT the distributions of the average cluster size for both detector thicknesses (200  $\mu\text{m}$  in 2004 and 300  $\mu\text{m}$  in 2003) have been compared and showed the expected behavior. I studied also the average cluster size for different beam conditions (focused versus wide beam setting), which showed no difference whatsoever and which indicates a uniform behavior of the pixel matrix.



## Chapter 6

# Development of an Infrared Laser Test System

### Contents

---

6.1	Introduction . . . . .	<b>106</b>
6.2	Laser Test Setup . . . . .	<b>106</b>
6.3	Laser Light Characteristics . . . . .	<b>108</b>
6.4	Laser Calibration . . . . .	<b>109</b>
6.5	Measurements carried out with the Laser Setup . . . . .	<b>116</b>
6.5.1	Time Walk of the Discriminator and the Delay Scans . . . . .	116
6.5.2	Study of the Sensitive Pixel Area . . . . .	118
6.5.3	Charge Sharing Measurements . . . . .	121
6.5.4	Bias scans . . . . .	127
6.6	FastOr-Study . . . . .	<b>131</b>
6.6.1	The FastOr Signal and the ALICE Trigger . . . . .	132
6.6.2	Chip Latency Measurements . . . . .	135
6.6.3	FastOr-Signal . . . . .	138
6.7	Summary . . . . .	<b>144</b>

---

## 6.1 Introduction

A test system based on an infra-red laser light was built in order to test the SPD assemblies. This laser allows a detailed study with well defined timing and energy deposition in the Silicon sensor and of the ALICE1LHCB chip characteristics. A class III Fabry-Perot 1060 nm laser was used to illuminate the SPD sensors. For this purpose, the Aluminum layer on the back-side of the sensor had to be removed to allow the light to penetrate into the Silicon. The laser beam had a divergence of  $2^\circ$  and beam spot size at the end of the laser fiber of less than  $10 \mu\text{m}$ . With this spot size it was possible to carry out precise position scans across the pixel matrix.

A laser calibration was performed using the internal threshold DAC and two radioactive sources ( $^{55}\text{Fe}$  and  $^{109}\text{Cd}$ ). The passage of a particle through the silicon sensor with energy depositions from 0.5 to 1.5 MIP could thus be simulated. For the study of charge sharing effects and bias scan dependent measurements two additional lasers were added to the setup which permitted measurements at different wavelengths (679 nm and 974 nm).

The laser measurements on ALICE assemblies could be directly compared with the results of the beam test 2002 and 2003. Furthermore, this setup allowed for the first time, a complete characterization of the working point and performance of the internally generated FastOr signal in the readout chip. This signal will contribute to the L0 trigger in ALICE proton-proton runs.

In the following chapter, the test system and the calibration of the laser is described. The measurements carried out on the ALICE assemblies are presented and discussed.

## 6.2 Laser Test Setup

An SPD prototype assembly was utilized for these measurements. One single ALICE1LHCB chip was flip-chip bonded to an SPD sensor and mounted on a test card. An identical setup to this (see chapter 5) was used in the beam tests 2002 and 2003. The SPD test readout chain is described in chapter 3.1.2. The SPD assembly had an opening in the aluminum back side contact of the sensor of  $\sim 11 \times 10 \text{ mm}^2$  allowing the laser light to penetrate into the Silicon sensor (see Figure 6.1).

A schematic view of the test system is shown in Figure 6.2. A pulsed solid state laser (Fabry Perot InGaAs) [77] in single mode at a wavelength of 1060 nm is pigtailed to a single mode fiber. The laser light traverses the fiber with a speed of 0.2 m/ns [78].

The laser bias voltage is provided by an HP<sup>1</sup> 81110A 330/165 MHz Pulse/Pattern generator in the range of 0 V to 2 V [79]. The pulse generator has a 5 ps time resolution with 0.01% frequency accuracy. The repeatability is typically 4 times better than the accuracy. The pulser can be triggered either internally, producing periodic pulses or externally by an input transition (rising or falling). The output pulse can be delayed in steps of 0.1 ns.

---

<sup>1</sup>Hewlett Packard, European Marketing Centre, P.O. Box 999, 1180 AZ Amstelveen, The Netherlands

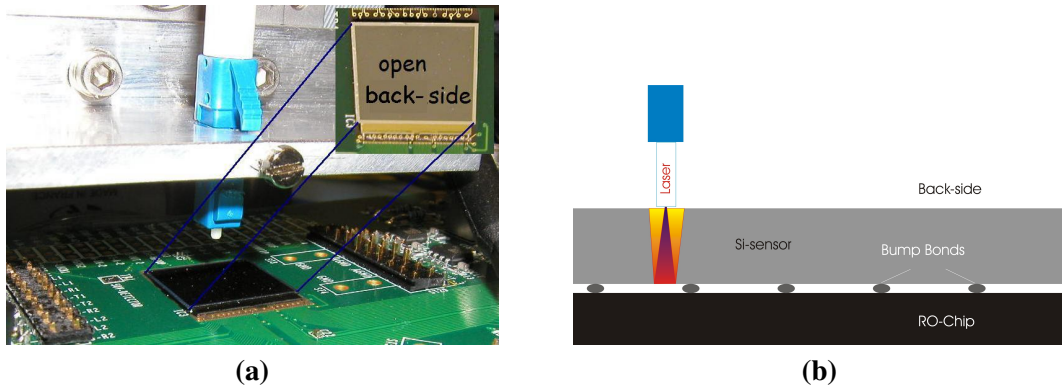


Figure 6.1: (a) Picture of the setup and of the single chip assembly showing the open back side of the sensor. The bias voltage is provided via ultrasonic wire bonds to the Aluminum ring. (b) Illustration of the passage of the laser light through the silicon sensor.

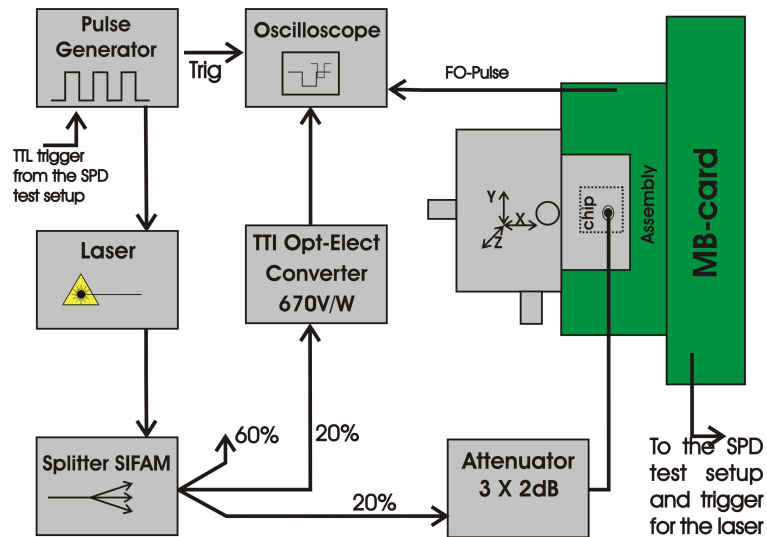


Figure 6.2: Illustration of the laser test setup system

The laser light is divided by a single mode SIFAM<sup>2</sup> 1x3 optical splitter into one 60% and two 20% branches [80].

One of the 20% fibers is used to monitor the laser pulse stability via a TIA-950 optical electrical converter from TTI<sup>3</sup> [81] and a 1GHz 9374M LeCroy<sup>4</sup> oscilloscope [82]. The optical head is powered by a 9 V Lithium battery and covers a spectral region of 900 to 1700 nm. Two gain modes can be set (x1200 or x12 000). The electrical bandwidth for the lower gain setting exceeds 750 MHz. The optical electrical converter uses an InGaAs diode as a photo detector and has a conversion factor of 670 V/W [83].

The second 20% beam is attenuated and brought to the SPD assembly (see Figure 6.1). The laser fiber is mounted on micrometric support structures above the SPD assembly and can be manually moved in 5  $\mu\text{m}$  steps. The tip of the fiber is oriented perpendicular to the Silicon surface with a beam spot size of less than 10  $\mu\text{m}$  on the surface [84].

### 6.3 Laser Light Characteristics

The laser wavelength of 1060 nm was chosen because its photon energy of 1.17 eV lies slightly above the energy gap of Silicon of 1.12 eV at room temperature [85]. From -20 °C to 20 °C the energy gap increases by roughly 1%. The ionization density is thus nearly uniform along the path of the beam through the sensor thickness and no focusing is required [86]. The absorption of the laser light in Silicon is described by Equation 2.1. The absorption coefficient  $\mu\text{m}$  is correlated to the extinction coefficient  $K$  by

$$K = \frac{\mu\lambda}{4\pi} \quad (6.1)$$

where  $\lambda$  is the wavelength of the penetrating light and  $K$  denotes the weakening coefficient of the initial wave amplitude as described in:

$$|E_T(z)| = |E_T(0)|e^{-K/z}. \quad (6.2)$$

The laser light with a wavelength of 1060 nm can penetrate  $\sim 890 \mu\text{m}$  into the silicon bulk. [87] For a 200  $\mu\text{m}$  thick silicon sensor as used for the ALICE assemblies the quantum efficiency is around 20 to 30% [88]. The laser light is reflected by the Aluminum layer on the front side of the silicon sensor and hence transverses the SPD silicon bulk twice.

To assure stability of the laser pulse the duty cycle was set to approx.  $10^{-6}$ . The pulse was repeated with a rate of 1 kHz with a pulse width of approx. 1.5 ns (see Figure 6.3). At higher laser energies the laser pulse width increases slightly (see chapter 6.4). For the chip latency and time walk measurements it was necessary to trigger the pulse generator externally with the clock of the ALICE1LHCB chip to ensure synchronization between the laser pulse and the SPD readout system. For this purpose the 10 MHz clock of the chip was scaled down by a factor 8192, corresponding to a frequency of  $\sim 1220$  Hz.

<sup>2</sup>SIFAM Fibre Optics Ltd. Broomhill Way, Torquay, Devon TQ2 7QL, England

<sup>3</sup>Terahertz Technologies Inc., 169 Clear Road, Oriskany, New York 13424 USA

<sup>4</sup>LeCroy Europe, 4 Rue Moise Marcinhes, Case postale 341, 1217 Meyrin 1, Switzerland

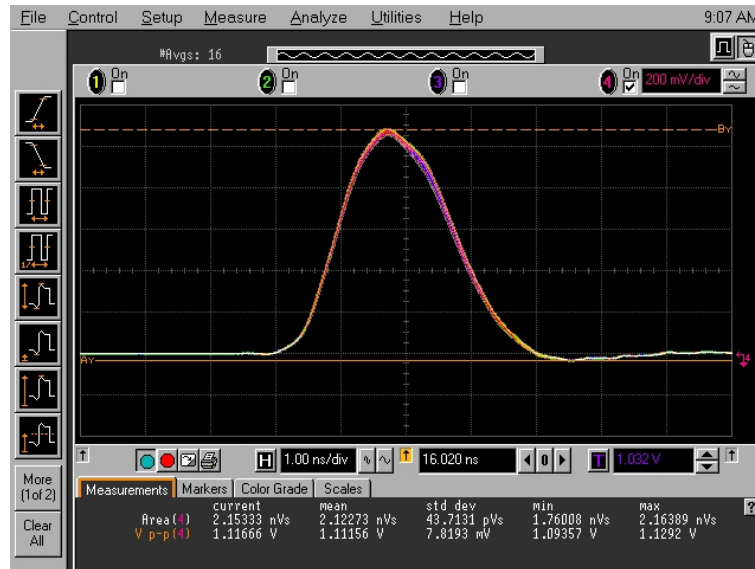


Figure 6.3: Screenshot of the oscilloscope showing the laser optical pulse. The settings of the pulse generator were: 1.45 V el. pulse amplitude, pulse width 5 ns, leading edge 0.8 ns.

The InGaAs Laser is a pulsed solid state laser system. The active medium is a rod of InGaAs and is pumped by a flash lamp, which illuminates the rod. The photons produced generate a spontaneous emission in the rod. With mirrors at the end of the rod, it is assured that the photons will traverse through the rod many times producing more and more photons in the rod. The photons produced are synchronous. One of the mirrors usually has a reflectivity of only 50% allowing an exit of the laser light out of the rod [89]. At lower bias voltages of the flash lamp, not enough photons are produced in the rod to start a spontaneous emission and the light emitted is not synchronous and is referred to as LED-light. Only when a certain threshold is exceeded, is enough photons pumped into the laser rod to start a chain reaction. The laser light becomes synchronous and enters the lasing range. In Figure 6.4, the transition from LED-light to the lasing range can be seen. The laser power is plotted against the laser bias voltage. For this measurement, the width of the laser bias was set to 5  $\mu$ s with a periodicity of 10  $\mu$ s. It can be observed that the lasing range starts around 0.8 V. Below this voltage, only LED-light is emitted from the laser. At higher laser bias setting, there is a linear region between the laser bias and the laser power (lasing range).

## 6.4 Laser Calibration

The pulse-generator was set to produce 5 ns wide electrical pulses at a frequency of 1 kHz. The rise time of the leading edge of the pulses amounted to 1.6 ns and the baseline voltage was set to -60 mV. The amplitude of the electrical pulses corresponds to the laser bias voltage. The induced laser pulses had a width of approx. 1.5 ns (see Figure 6.3).

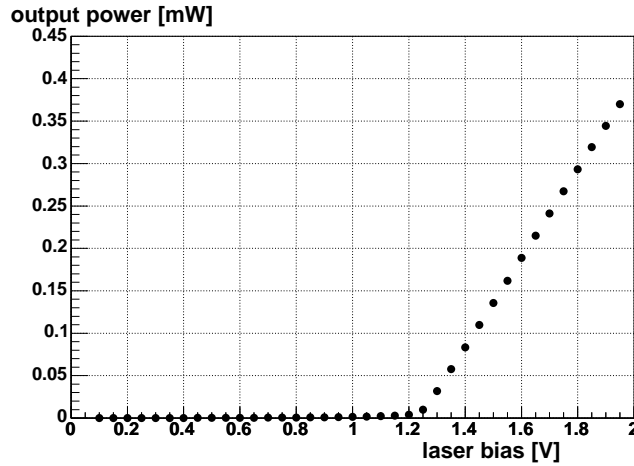


Figure 6.4: The laser response graph for a  $5 \mu\text{s}$  wide laser bias pulse at a periodicity of  $10 \mu\text{s}$ . The laser power was measured with a laser power meter.

As a first step in the calibration of the laser, the laser output pulse was measured with the O/E-converter. As described in chapter 6.2, the converter was calibrated to  $670 \text{ V/W}$ . The output voltage and the area below the laser pulse were recorded for every  $0.1 \text{ V}$  resp.  $0.5 \text{ V}$  step of the laser bias voltage and are plotted in Figure 6.5. Since the number of photons generated at this time structure of the pulse gets very small the output of the O/E converter can be measured only for laser bias settings higher than  $1.37 \text{ V}$ . It can be seen from the curve plotting, the area below the laser pulse is not proportional to the laser amplitude curve. At higher laser bias voltages the laser pulse becomes not only higher in amplitude but also wider and thus the inclination of the pulse-area curve is larger. For further calibration the laser power per pulse was calculated out of the pulse-area curve, since it is directly proportional to the number of the produced photons.

While the error on the laser bias voltage is very small ( $\leq 0.01\%$ ) [79], the error on the output of the O/E converter can not be neglected. The sigma of the output voltage at 200 sweeps is taken as the error.

This measurement confirmed the expected linear behavior in the lasing range for short laser pulses (Figure 6.6).

The laser bias voltage settings were correlated to the internal threshold DAC settings of the ALICE1LHCB chip. For every laser bias voltage the threshold DAC setting (8-bit DAC), at which the readout efficiency of the induced signal decreased to 50%, was assigned to the corresponding laser bias voltage. The DAC-setting behaves inversely proportional to the signal threshold. At high DAC setting the threshold is low and vice versa. For different settings of the laser bias voltage, the efficiency curves were recorded. The resulting S-curves are plotted in Figure 6.7. The laser bias voltage was varied between  $1.39 \text{ V}$  and  $1.6 \text{ V}$  and the threshold

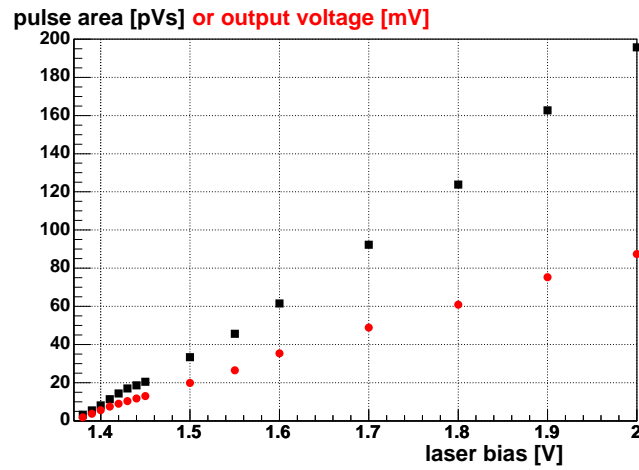


Figure 6.5: The laser response graph for a 1.5 ns wide laser bias pulse. The upper line (boxes) shows the area below the laser pulse and the lower line (circles) the amplitude of the laser pulse. Both curves were taken with a gain of 1200 of the O/E converter.

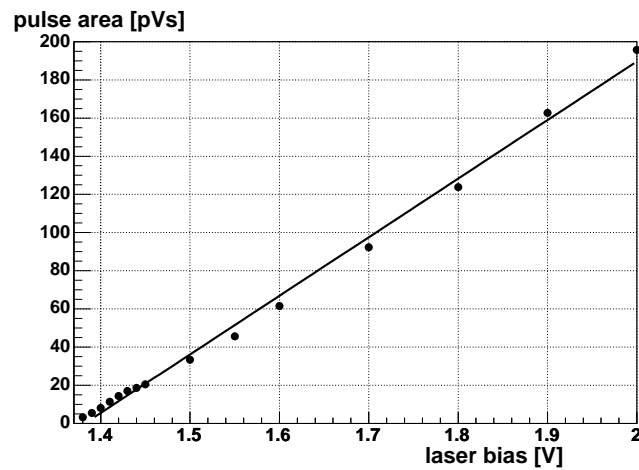


Figure 6.6: The laser response graph taken as the area below the laser pulse for different laser bias settings is linear fitted.

DAC was scanned from 60 to 210. From each S-curve, the 50% value was obtained by fitting the data with a standard error function as described in:

$$\operatorname{erf}(x) = \frac{2}{\sqrt{\pi}} \int_0^x e^{-t^2} dt [90] \quad (6.3)$$

The results of the correlation are shown in Figure 6.8. The RMS of the fit-function is used as the error of the DAC-calibration, while the error on the DAC setting can be neglected [79]. While the correlation for laser bias settings lower than 1.45 V is linear, at higher settings the threshold DAC is measured to be higher than expected due to the nonlinearity of the DAC-threshold below a setting of 130. One can also see that the S-curves below this setting are wider due to this internal non-linearity. Therefore only the region with the linear correlation was considered for the calibration of the laser. Using the results from the measurements with the O/E converter the linear correlation could be extrapolated to higher laser bias voltage settings. In order to

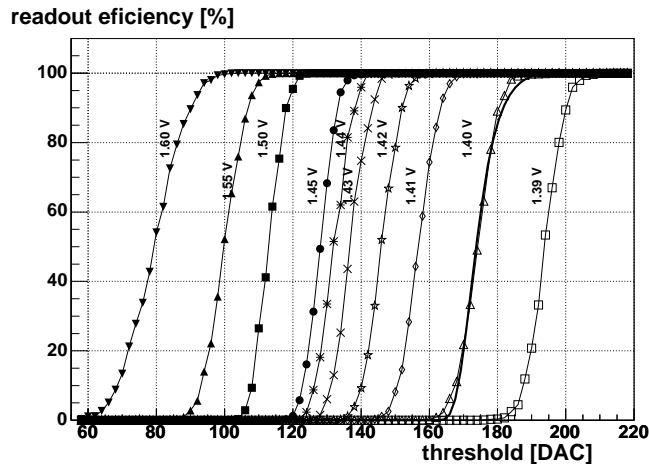


Figure 6.7: S-Curves for different laser bias voltages.

express the threshold DAC values as the number of charge carriers a DAC-calibration of the SPD assembly was performed using radioactive sources  $^{55}\text{Fe}$  and  $^{109}\text{Cd}$ . For these sources the charge generated in the sensor is well understood. The  $^{55}\text{Fe}$  source emits X-rays with a maximum energy of 6 keV corresponding to 1600 electron-hole pairs in the silicon sensor, while  $^{109}\text{Cd}$  has two X-ray lines with the maximum energy of 22 keV (resp. 6100 electrons) at 76.4% and 24.9 keV (resp. 6900 electrons) at 13.7%.  $^{109}\text{Cd}$  has also a third X-ray line with maximum energy of 88 keV but this one can be neglected due to its occurrence of only 3.6%. It will only result in a higher background [91].

For both radioactive sources a threshold DAC-scan was performed, resulting in the curves shown in Figure 6.9 and Figure 6.10. Here the number of fired pixels per second is plotted versus the threshold DAC setting. The curves show the behavior of a standard S-curve with one exception. A plateau is not reached at the lower threshold as expected in case of efficiency

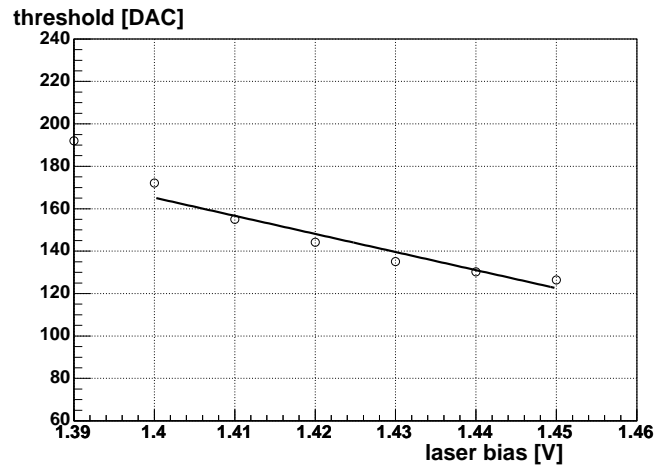


Figure 6.8: DAC Calibration with the laser. The DAC value at which 50% of the efficiency is measured and correlated to the laser bias setting.

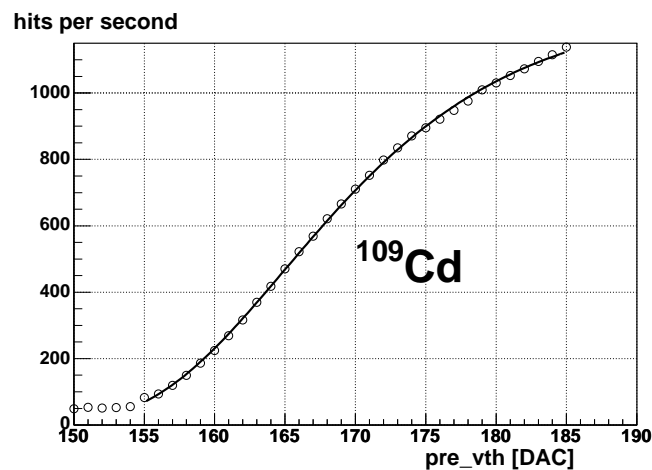


Figure 6.9: Source calibration of the SPD assembly with a  $^{109}\text{Cd}$  source. Fired pixel cells per second for different threshold settings are plotted. The fitting was performed with an error function giving the 50% value of the S-curve which corresponds to the 22 keV and 24.9 keV lines of  $^{109}\text{Cd}$ . The range for the plot was set from DAC 155 to DAC 185 in order to avoid the influence of the 80 keV line of  $^{109}\text{Cd}$  and the effect of the threshold on the effective size of a pixel cell.

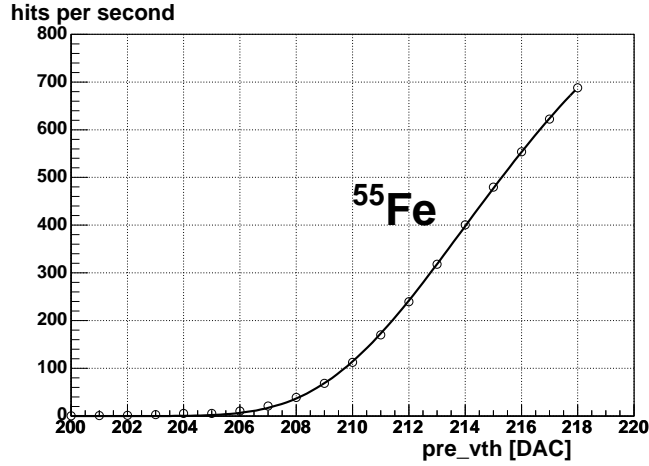


Figure 6.10: Source calibration of the SPD assembly with a  $^{55}\text{Fe}$  source. Fired pixel cells per second are plotted for a threshold range from DAC 200 to DAC 218, which is the found minimum threshold. The error function was used to fit the points and gives the 50% value, which corresponds to the 6keV line of  $^{55}\text{Fe}$ .

measurements utilizing the laser pulse to ionize the sensor. This effect is a consequence of the charge sharing between two or more adjacent pixels. At lower threshold, it is more probable for an incoming X-ray to fire more pixels. Hence, the number of fired pixels per second does not reach a plateau, but increases further with increasing pre\_vth setting. Due to this charge sharing effect, the recorded curves could not be fitted by the same curve fitting equation as the S-curves measured in the case of the laser illumination, but were differentiated to show the corresponding 50% value. The differentiated curve was fitted with a polynomial of the 6th order and the maximum of the fitting curve was taken as the threshold of the SPD required for the X-ray line to be detected with 50% efficiency. The RMS of the fit was taken as the error on the points of the corresponding DAC-calibration values. The error on the DAC setting can be neglected. By obtaining these two points, the DAC-calibration of the SPD assembly could be performed and is shown in Figure 6.11. The DAC-calibration can also be described by a simple linear equation:

$$n_{el} = -93.2 \cdot DAC + 21601.7 \quad (6.4)$$

The error on the DAC-calibration is performed using the error propagation.

From these measurements, the correspondence between the laser bias voltage and the charge collected in the silicon can be determined. The result is shown in Figure 6.12. The errors on the laser bias were neglected due to the very good accuracy of the pulse-generator. The errors in the quantity of generated electrons are the quadratic sum of the errors in the fit function of the laser power scan and the errors of the linear DAC-calibration and are of the order of 950 to 1200 electrons.

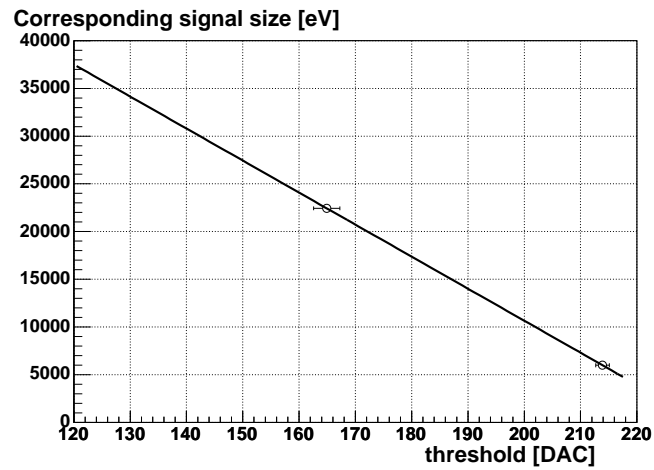


Figure 6.11: The DAC calibration of the SPD assembly performed with two radioactive sources -  $^{55}\text{Fe}$  and  $^{109}\text{Cd}$ .

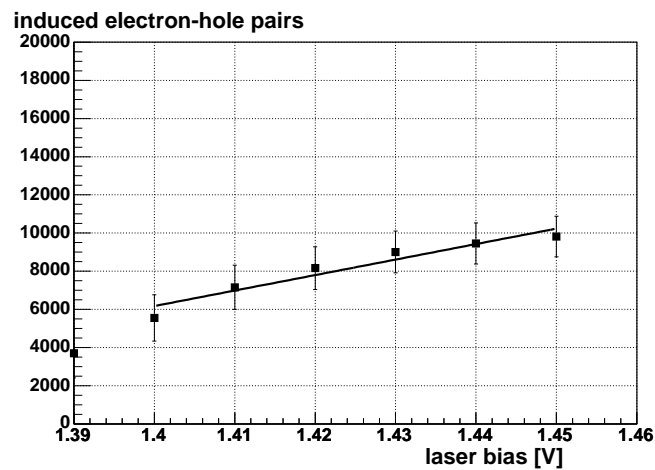


Figure 6.12: Laser Calibration. The number of induced charge carriers is plotted as a function of the laser bias voltage.

## 6.5 Measurements carried out with the Laser Setup

The measurements using the 1060 nm laser provide the possibility to cross-check the results obtained in the beam tests of the ALICE SPD assemblies obtained in 2002 and 2003. A detailed description of these beam tests can be found in chapter 5. All the tests were carried out using high energetic proton beams. Therefore the energy loss of one MIP in 200  $\mu\text{m}$  of Silicon had to be simulated with the laser while keeping the laser pulse width as small as possible (1.5 ns) to achieve comparable conditions as provided in the beam tests. A detailed simulation of the mean energy loss of one MIP in 200  $\mu\text{m}$  of silicon can be found in chapter 2.1.1.

### 6.5.1 Time Walk of the Discriminator and the Delay Scans

For these measurements the SPD readout system and the laser pulse were operated fully synchronously by triggering the laser using the scaled down chip clock ( $\sim 1220$  Hz). The ALICE1LHCB chip has two DACs for the control of the delay of the strobe signal, which generates the readout of the SPD system, allowing the readout strobe signal to be shifted in 100 ns steps respectively to the trigger. This is sufficient for a fully efficient readout because in the SPD test readout system, the strobe signal length was set to 200 ns. The internal DACs and the readout process of the SPD ALICE1LHCB chip are described in chapter 3.

For a more detailed study of the time walk of the discriminator, but also to make measurements of the mobility of the charge carriers under different bias voltages, it was necessary to delay the readout in finer steps. This could be achieved by delaying the laser pulse instead of the readout strobe. The pulse-generator allows shifting of the electrical laser bias pulse in 0.1 ns steps.

The time walk of the discriminator corresponds to the time difference in the signal rise time and on the size of the induced signal. The time when the signal threshold is crossed determines the time when the hit is recorded. When more charge carriers are induced in the Si-sensor the rising edge of the electrical signal is steeper and the threshold is reached faster. In Figure 6.14 the effect of the different rise times on the time walk is illustrated schematically. The laser bias voltage was set to simulate four different signal sizes:  $\sim 8600$ ,  $\sim 14300$ ,  $\sim 30500$  and  $\sim 467000$  electron-hole pairs. At each setting of the laser bias voltage a delay scan was performed by shifting the laser pulse in steps of 1 ns towards the strobe signal. The threshold of the pixel matrix was set to  $\sim 2900$  electrons. In Figure 6.13 the efficiency curves for the four different laser power settings are plotted as a function of the laser pulse delay time. The efficiency is defined as the ratio of totally registered events to empty events. In all cases the 100% efficiency plateau is approx. 200 ns long and is in good agreement with the strobe length. From the rising edge of the efficiency curve, it can be seen that the SPD becomes completely efficient within approx. 6 ns. In case of a higher laser power, the efficiency plateau is shifted in respect to the laser pulse. As the amplitude of the generated electrical signal is higher the crossing point occurs earlier compared to lower energies, when the signal amplitude is smaller and the rise time of the shaped signal is slower. This means, that the distance from the electrical signal to the strobe signal increases resulting in a delay of the efficiency curve.

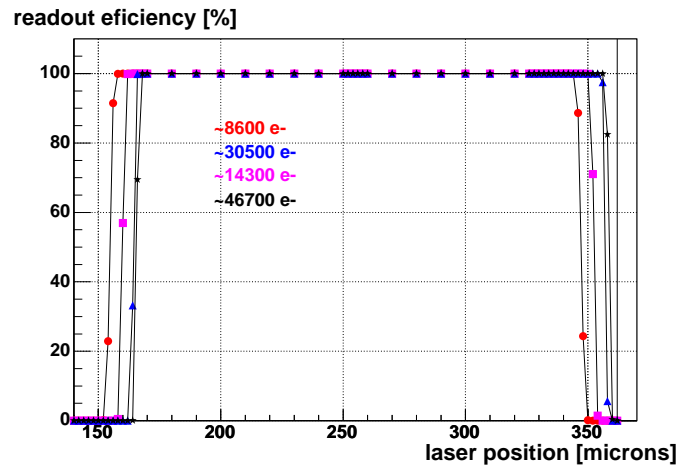


Figure 6.13: The readout efficiency curve is delayed in respect to the trigger with increasing laser power. The signal is built up faster in the discriminator on the pixel cell level, which results in a faster hit registration.

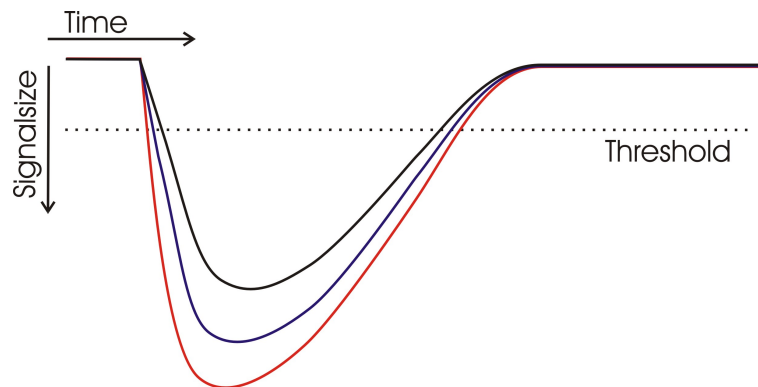


Figure 6.14: Illustration of the time walk of the discriminator. If a higher signal is induced in the sensor, the rise time of the signal pulse in the discriminator is faster and thus the hit registration.

With this measurement the time walk of the discriminator of the ALICE1LHCB chip was measured directly for the first time. In case of an increase in the number of induced charge carriers in the sensor from  $\sim 0.5$  MIP to  $\sim 3$  MIP the readout is performed faster by  $11.48 \pm 0.75$  ns.

### 6.5.2 Study of the Sensitive Pixel Area

Several position scans using the laser were performed across the pixel matrix and the efficiency of the readout under different threshold conditions was recorded. In case of the  $r\varphi$ -direction of the pixel matrix ( $50 \mu\text{m}$  pixel cell length) the scans were done in  $5 \mu\text{m}$  steps, while for the  $z$ -direction ( $425 \mu\text{m}$  pixel cell length) the beam spot was moved in steps of  $10 \mu\text{m}$ .

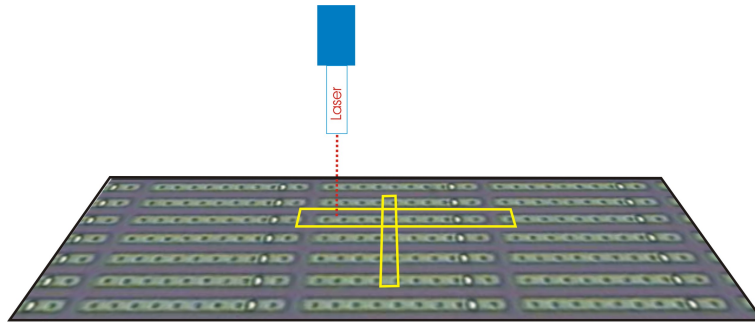


Figure 6.15: Illustration of the scan directions. Four pixel cells were scanned in the  $r\varphi$ -direction and one in the  $z$ -direction.

In the short direction, up to four pixel cell lengths were scanned and the results are plotted in Figure 6.15. For these measurements, the laser power was set to induce  $\sim 8600$  charge carriers and the threshold was varied between the DAC settings 200 ( $\sim 2900$  electrons) and 160 ( $\sim 6700$  electrons). While at low threshold, the pixel profile can not be seen, the pixel structure becomes evident if the threshold is increased. At very high threshold settings, the charge carriers induced between two pixels, are not sufficient to trigger a hit. Thus, the efficiency drops to 0, as it can be seen in this Figure.

In this way the size of the sensitive pixel area in the  $z$ -direction ( $425 \mu\text{m}$ ) was also measured. For this purpose, the FWHM of the efficiency curves taken during position scans were calculated for different settings of the threshold. The results are plotted in Figure 6.17. With a laser power setting close to threshold, the borders of pixel cells are not fully efficient due to charge sharing with the adjacent pixel cell. The length of the sensitive pixel area decreases to approx.  $400 \mu\text{m}$  for a threshold of around 7600 electrons if 8600 electrons were generated with the laser pulse. If the laser pulse is set to illuminate the border of one pixel cell, the charge sharing with the adjacent cell causes a decrease in the effective area of the pixel cell.

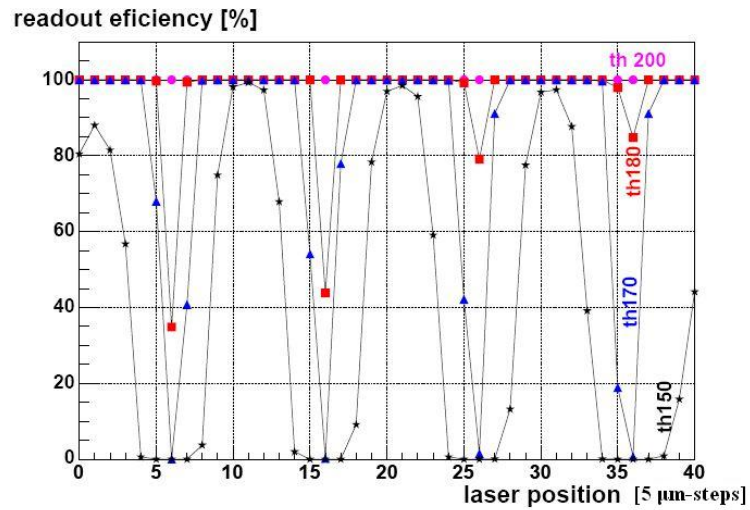


Figure 6.16: Readout efficiency plot for the scan in the  $r\varphi$ -direction. 8700 electrons were induced into the silicon sensor and the threshold was set to the DAC value 200 ( $\sim 2900 e^-$  - discs), 180 ( $\sim 4800 e^-$  - squares), 170 ( $\sim 5800 e^-$  - triangles) and 150 ( $\sim 7600 e^-$  - stars).

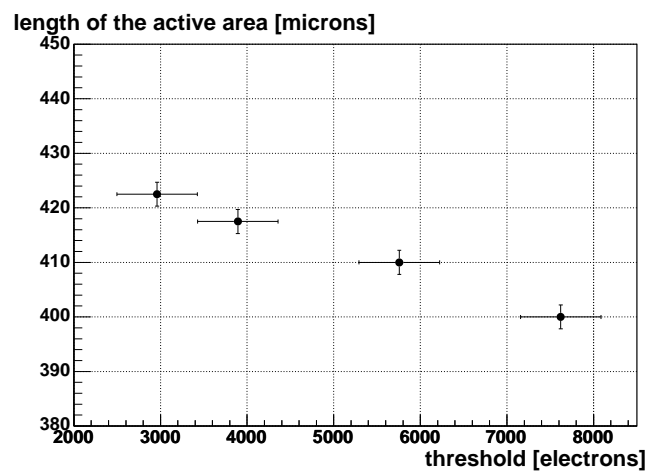


Figure 6.17: Effective length of the active area of one pixel cell in the long direction ( $z$ ).

The sensitivity of the active width of the pixel cells could be studied in detail because of the low threshold settings possible and thus, the laser power could be set to induce a small number of charge carriers into the silicon sensor. A drawback of this is the decrease of the pixel cell active area when the charge induced is close to the threshold.

### Effect of the Al-vias on the efficiency

During position scans in the long width of the pixel, an oscillation in the trigger efficiency curve became evident for a laser power close to the threshold. An illustration of the measurement is given in Figure 6.18. Every  $40\ \mu\text{m}$  a maximum in efficiency could be observed. The first visible maximum is slightly wider,  $60\ \mu\text{m}$  wide. The oscillation could be correlated to the position of the aluminum vias through the  $\text{SiO}_2$  layer between the pixel aluminum and the implantation (p+) of the sensor pixel. A description of the Al-vias is given in chapter 3. The efficiency of

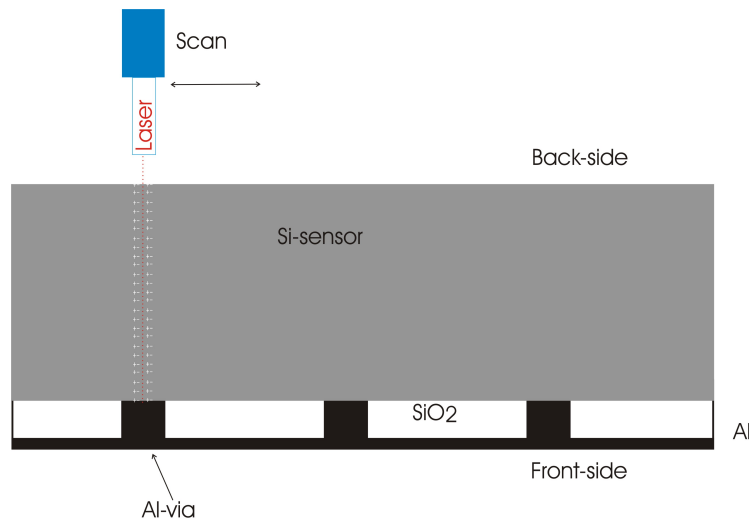


Figure 6.18: Illustration of the effect of the aluminum vias on the efficiency. The Al-vias cause a field distortion in the silicon sensor. Increasing the bias voltage, the field distortions are weakened.

the readout dropped when the laser beam was illuminating the area close to the vias. The first maximum, which is wider by  $20\ \mu\text{m}$  than the others, corresponds to the pad used for the Pb-Sn bump-bond. In Figure 6.19 this effect and the correlation to the Aluminum on the front side of the sensor is shown.

The efficiency drop at the Al-vias was caused by field distortions in the silicon sensor. The  $\text{SiO}_2$  layer is normally positively charged and induces negative charges in the silicon sensor (accumulation layer) close to the contact with the  $\text{SiO}_2$  layer. In this way field distortions in the sensor are created close to the surface and the charge carrier collection is disturbed. A

measurement of this effect is the so called flat-band voltage  $V_{fb}$ , which was found to be 2 - 3 V [39]. By increasing the bias voltage, the readout efficiency drops at the positions of the Al-vias and should become less evident due to the straightening of the field lines. This effect can be seen in Figure 6.19. For these measurements, the laser induced  $\sim 5300$  electrons at a threshold of  $\sim 3900$  electrons. The oscillations are well pronounced in the case of a bias voltage of 20 V. With increasing bias voltage the field distortions in the Si-sensor are weakened. At a bias voltage above 150 V, corresponding to an electrical field of approx. 750 kV/m, the oscillations in efficiency have disappeared.

It is important to note that this effect is only visible if the induced signal is close to the threshold. The operating settings (bias voltage + threshold) during data taking are such that this effect is negligible for normal condition runs.

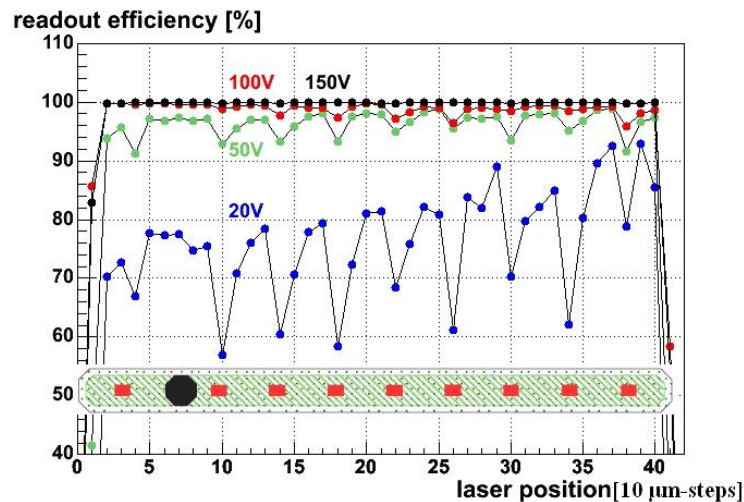


Figure 6.19: The Al-vias on the front-side of the sensor located along one pixel cell induce field distortions and hence cause an efficiency drop if the laser power is set close to the threshold. The field distortion can be weakened with higher bias voltage.

### 6.5.3 Charge Sharing Measurements

In order to study the charge sharing between two adjacent pixels, the laser spot was moved in  $5 \mu\text{m}$  steps across two pixels in the short and in the long direction. The measurements were performed with three different laser wavelengths. Besides the 1060 nm laser, lasers with a wavelength of 679 nm and 974 nm were also used. The penetration depth for the chosen laser lights can be seen in the Table 6.1 and Figure 6.21. The laser light with the wavelength of 1060 nm penetrates completely the sensor, while the light from the 974 nm laser is completely absorbed after  $80 \mu\text{m}$ . With the 679 nm laser, an alpha particle, which penetrates only a couple of microns into the silicon, could be simulated. At every position, the laser bias voltage of all three lasers was set to produce a charge equivalent to the passage from 0.5 MIP ( $\sim 8600 e^-$ ), 0.6

MIP ( $\sim 10200 e^-$ ), 0.8 MIP ( $14300 e^-$ ) and 1 MIP ( $18300 e^-$ ) in  $200 \mu\text{m}$  silicon. The threshold of the detector was set to a 200 DAC value corresponding to approx. 2900 electrons. Figure 6.20 illustrates schematically the method used for these measurements. The charge sharing

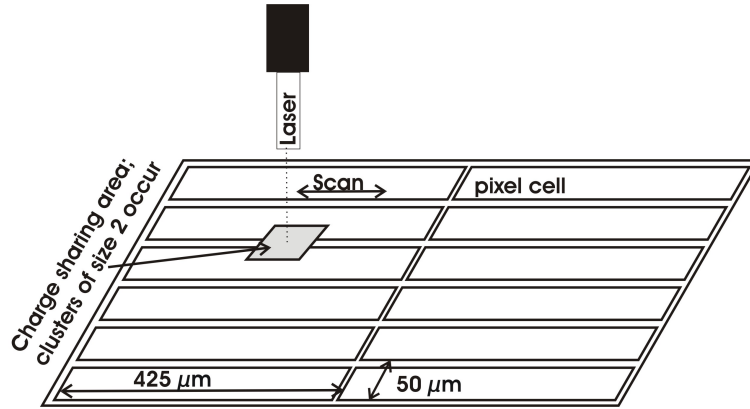


Figure 6.20: For charge sharing study the pixels were scanned in the  $r\varphi$ -direction in  $5 \mu\text{m}$  steps and in the  $z$ -direction in  $10 \mu\text{m}$  steps. The charge sharing area, in which both pixel cells register a hit, is recorded with three different laser wavelengths.

Wavelength	Absorption coefficient ( $\text{cm}^{-1}$ )	Penetration depth ( $\mu\text{m}$ )
679	2560	3.9
974	125	80
1060	11.2	890

Table 6.1: Absorption coefficients and penetration depth for the three laser wavelengths used. [93]

area is defined as the distance over which hits are recorded in two adjacent pixel cells (i.e. two-pixel clusters). This area corresponds to a rectangular distribution with a length  $d$ . The calculated spatial resolution of such a distribution corresponds to the digital resolution, which can be calculated with

$$\sigma(x) = \frac{d}{\sqrt{12}} \quad (6.5)$$

and can be compared to the spatial resolution for two pixel clusters obtained from the beam tests. The results of the laser measurements are presented in Figure 6.22, where the width  $d$  of the charge sharing area is plotted versus the laser power setting expressed in induced electrons. The error on the width of the charge sharing area is composed of the error of the step size ( $5 \mu\text{m}$ ) and the size of the beam spot. The beam spot is  $10 \mu\text{m}$  wide at the back-side of the sensor and widens as it transverses the Silicon sensor. Therefore for the error calculations the sigma of the mean width of the beam spot is taken. The mean width was chosen as the width of laser beam at its half intensity, i.e. when the laser light is attenuated to 50%. Taking into account the divergence of the laser light of approx.  $2^\circ$  [84] the mean width of the laser beam in case of 1060 nm laser spot amounts to  $20 \mu\text{m}$ . Assuming a perfect Gaussian profile of the laser

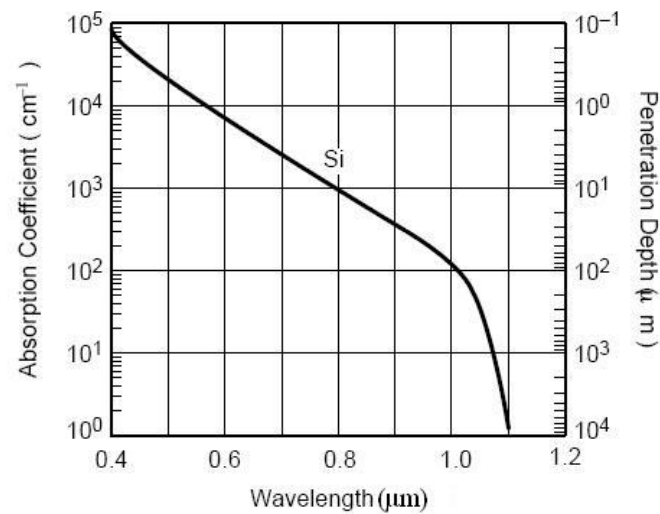


Figure 6.21: Absorption coefficient in  $\text{cm}^{-1}$  and penetration depth in  $\mu\text{m}$  of light in Silicon. Below the band gap cutoff in silicon ( $\sim 1100$  nm corresponding to 1.14 eV) all absorbed Photons produce electron hole pairs. [87]

beam, this leads to a sigma of the beam spot of approx.  $4.5 \mu\text{m}$ . The total error on the beam position hence sums up quadratic to  $6.8 \mu\text{m}$ .

From Figure 6.22 it can be seen that in the case of the 1060 nm laser light the width  $d$  of the charge sharing area in the short direction amounts to  $10 \pm 6.8 \mu\text{m}$  and  $5 \pm 6.8 \mu\text{m}$  in the long direction in the case of a laser power setting of 0.5 MIP. The width  $d$  increases to  $30 \pm 6.8 \mu\text{m}$  and in the long direction to  $25 \pm 6.8 \mu\text{m}$  when the laser power was set to produce 18000 charge carriers in the sensor (1 MIP) at a threshold setting of 200 DAC. A similar result was obtained for the laser light with the wavelength of 974 nm inducing approx the same amount of charge carriers into the SPD-sensor.

If the 679 nm laser was used the width of the charge sharing area for all four laser power settings is wider by  $5 \mu\text{m}$  compared to longer wavelength lasers. This is an effect of the diffusion of the electron-hole pairs. For the 679 nm laser the charge is induced close to the back-side of the sensor and it needs to traverse through almost the complete sensor thickness of  $200 \mu\text{m}$  to the front-side, where it is collected. The longer wavelength lasers induce their charge uniformly through the sensor due to the larger penetration depth. Thus the diffusion has less influence on the charge sharing area.

### Spatial resolution - Comparison with beam tests

To compare the spatial resolution of two pixel clusters with results obtained in beam tests, the results on the charge sharing area obtained with the 1060 nm laser at a power setting of

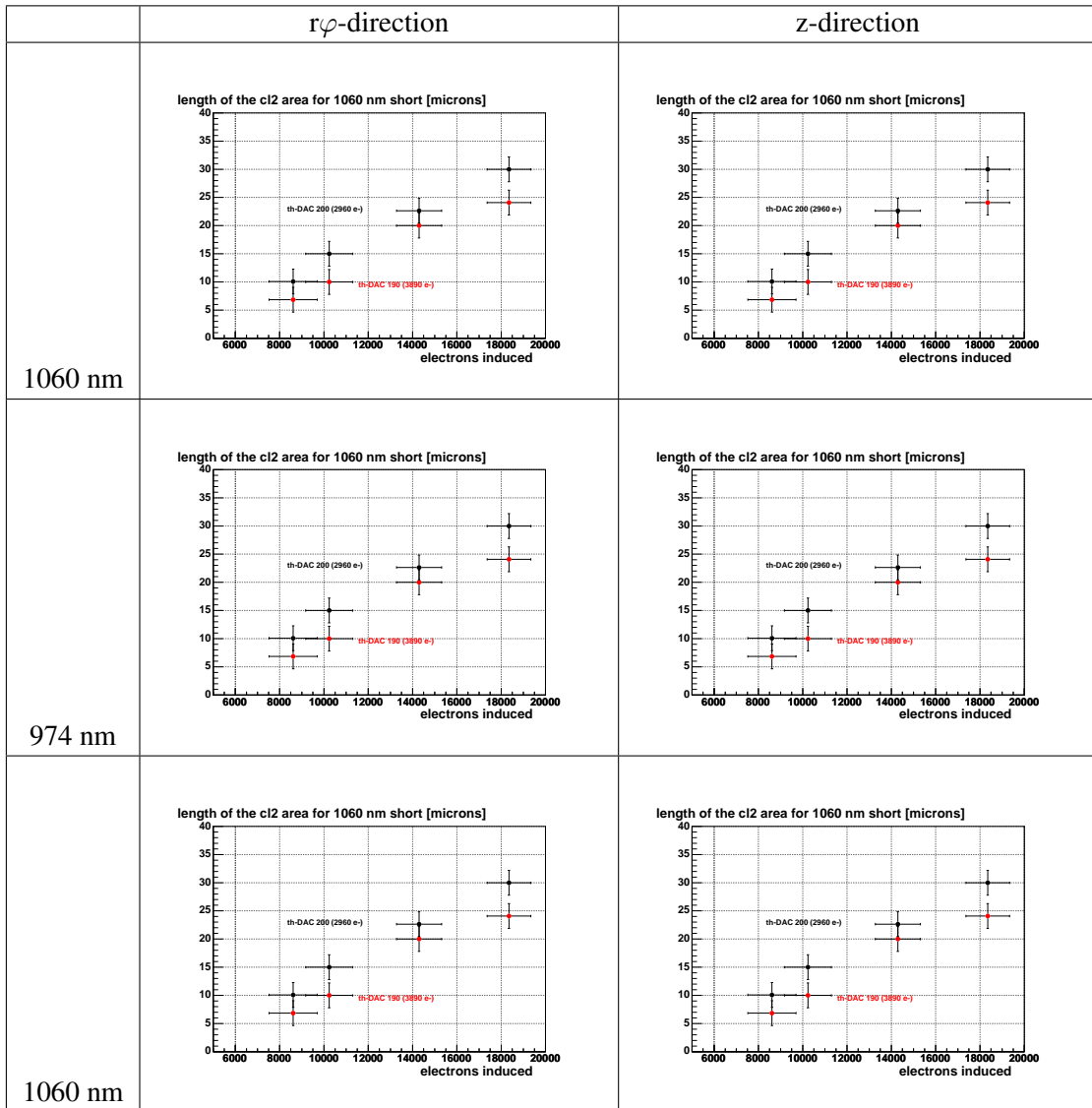


Figure 6.22: Size of the charge sharing area between two adjacent pixel cells in both directions for the three used laser wavelengths (679 nm, 974 nm and 1060 nm).

1 MIP were studied. The light of this laser illuminates the sensor completely inducing charge carriers evenly distributed along the beam. Therefore a direct comparison with the results from the beam tests is possible, where the charge carriers induced are also evenly distributed in the silicon sensor.

From the laser measurements the obtained widths of the charge sharing area in the short ( $r\varphi$ ) and the long (z) directions the spatial resolution can be calculated using Equation 6.5 and are summarized in Table 6.2: These results can be only partly directly compared to the results from

	Intrinsic resolution
$\sigma^{cls2}$ ( $r\varphi$ -direction)	$8.66 \pm 2 \mu\text{m}$
$\sigma^{cls2}$ (z-direction)	$7.22 \pm 2 \mu\text{m}$

Table 6.2: Spatial resolutions measured with the 1060 nm laser in both directions.

the beam test 2002, i.e. only the  $r\varphi$ -direction. In this beam test, the silicon sensor thickness of the SPD plane under study had the same thickness as the assembly used in the laser test setup (200  $\mu\text{m}$ ). For a detailed description of the run conditions and the beam test setup see chapter 5. The 200  $\mu\text{m}$  are the nominal thickness of the silicon sensors for the ALICE SPD (see chapter 3). The spatial resolution for two pixel clusters from the beam test 2002 is only available for the  $r\varphi$ -direction, while for the z-direction this parameter had to be estimated using the results from the beam test 2003, when the available SPD assembly under study had a sensor thickness of 300  $\mu\text{m}$  and the spatial resolution was calculated for both directions (see chapter 5).

In the 2003 beam test the spatial resolution was measured in both directions. Taking these results into account and assuming that the spatial resolution scales linearly by the same amount in both directions for the two sensor thicknesses used the spatial resolution in the z-direction for a 200  $\mu\text{m}$  thick sensor could be estimated. In Table 6.3 the results of the spatial resolution in both directions and both detector thicknesses are presented. One can see that the results obtained from the laser measurements are in good agreement with the analysis of the beam test data. From these measurements it can also be seen that the width of the charge sharing area

Detector thickness	200 $\mu\text{m}$	300 $\mu\text{m}$
( $r\varphi$ -direction)		$7.7 \pm 0.9 \mu\text{m}$
(z-direction)	$6.8 \pm 0.3 \mu\text{m}$	$9.2 \pm 0.6 \mu\text{m}$

Table 6.3: Spatial resolutions for both directions and two detector thicknesses (200 and 300  $\mu\text{m}$ ) from the beam test analysis [92] and [94].

between two pixel cells is bigger in the  $r\varphi$ -direction than in the z-direction. This is a direct consequence of the geometrical conditions of the pixel matrix. While two adjacent pixel cells in the  $r\varphi$ -direction share a 425  $\mu\text{m}$  border, in the z-direction the border is only 50  $\mu\text{m}$  wide. All charge carriers induced between two pixels in the  $r\varphi$ -direction will be shared only by these two pixel cells. In the z-direction on the other hand the spreading of the generated charge carriers on more than two pixel cells is more probable. This spreading of charge carriers can be described

with the Gaussian diffusion:

$$Q(x, y) = \frac{e}{2\pi\sigma_{diff}^2} \exp \left[ \frac{(x - x_0)^2}{2F_{da}^2\sigma_{diff}^2} + \frac{(y - y_0)^2}{2\sigma_{diff}^2} \right] \quad (6.6)$$

while

$$\sigma_{diff}^2 = \frac{2k}{e} T F_{df} l_{dr} \quad (6.7)$$

where:  $F_{dv}$  sensor thickness / bias voltage  
 $F_{da}$  asymmetry parameter for the x/y diffusion

With the asymmetry parameter  $F_{da}$  the factor describing the difference in probabilities of the generation of two pixel clusters in the two direction can be set. In the simulation of the cluster size distributions the asymmetry parameter  $F_{da}$  was set to 0.85 in order to correctly fit the data from the beam test 2003. In 6.23 the simulation of the cluster size distribution and the real data from beam test 2002 are shown. As one can see the agreement especially in case of the dominating cluster patterns is good. The asymmetry parameter  $F_{da}$  could be measured directly

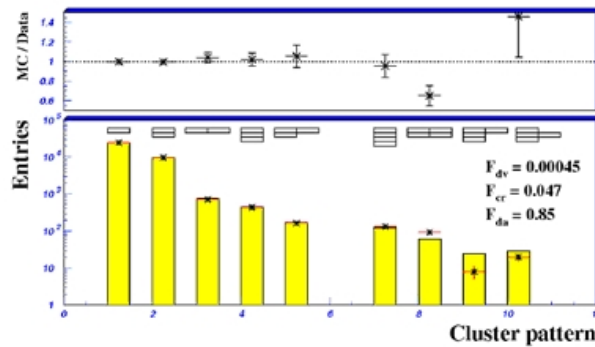


Figure 6.23: Simulated distribution of cluster topologies and the comparison to beam data 2003. [95] The asymmetry parameter  $F_{da}$  had to be set 0.85 in order to comply with the beam data. This coefficient could be directly measured with the laser setup (see Figure 6.22 and Table 6.4).

with the laser setup. This parameter corresponds to the ratio of the width of the charge sharing area in the  $r\varphi$ -direction to the parameter of the  $z$ -direction. As expected, for all three laser measurements, the width of the charge sharing area in the short direction is smaller than in the long direction. The coefficient  $F_{da}$  could be calculated to 0.83 confirming the simulation settings. With the measurements on charge sharing with the three different laser lights it was possible to cross check and confirm the results of the spatial resolution obtained in the beam tests. Further, a parameter which was tuned empirically in the simulation could also be directly verified by taking the ratio of the width of the charge sharing areas in the two directions.

	1060 nm	974 nm	679 nm
( $r\varphi$ -direction)	$30 \pm 6.8 \mu\text{m}$	$31 \pm 6.8 \mu\text{m}$	$34 \pm 6.8 \mu\text{m}$
(z-direction)	$25 \pm 6.8 \mu\text{m}$	$25 \pm 6.8 \mu\text{m}$	$30 \pm 6.8 \mu\text{m}$
$F_{da}$	0.83	0.83	0.88

Table 6.4: Lengths of the charge sharing area in both directions for the three laser wavelengths give the asymmetry parameter  $F_{da}$ .

### 6.5.4 Bias scans

#### Depletion Area

Applying a reverse bias voltage to the p-n junction of the sensor the depletion of the sensor can be increased. The CV-measurements at the foundry show that for the  $200 \mu\text{m}$  thick SPD sensors, the sensor volume is fully depleted at about 12 V.

Illuminating the sensor with three different laser wavelengths allowed a charge carrier production at different sensor depths and thus a study of the size of the depletion area. In Figures 6.24 - 6.26 the change of the average cluster size can be observed as the bias voltage is scanned from 0 to 50 V. These cluster sizes can be understood as directly proportional to the size of the depletion area. At each bias voltage setting, the laser power was set to generate  $\sim 10200$ ,

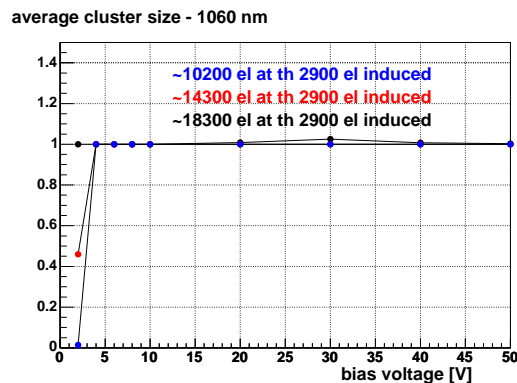


Figure 6.24: Average cluster size as a function of the bias voltage in the case of illumination with a 1060 nm laser. The energy was tuned to generate  $\sim 10200$ ,  $\sim 14300$  and  $\sim 18300$  electrons in the silicon sensor.

$\sim 14300$ , and  $\sim 18300$  electrons at a threshold of  $\sim 2900$  electrons, respectively. The laser light was set to illuminate the center of one pixel. For the longer wavelength lasers (974 nm and 1060 nm) hits are registered down to 5 V, while for the 679 nm laser light, not enough charge to fire a pixel is collected below 12 V. The 679 nm light does not penetrate deep enough into

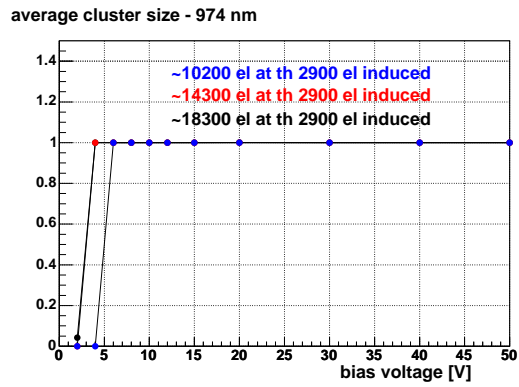


Figure 6.25: Average cluster size as a function of the bias voltage in case of illumination with a 974 nm laser. The energy was tuned to generate  $\sim 10200$ ,  $\sim 14300$  and  $\sim 18300$  electrons in the silicon sensor.

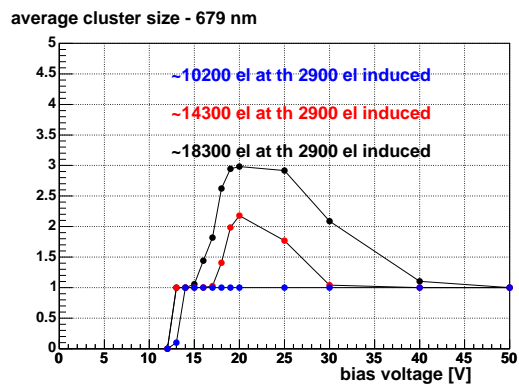


Figure 6.26: Average cluster size as a function of the bias voltage in case of illumination with a 679 nm laser. The energy was tuned to generate  $\sim 10200$ ,  $\sim 14300$  and  $\sim 18300$  electrons in the silicon sensor.

the silicon sensor to produce enough charge carriers in the depleted area. There is no electric field in this area and therefore the diffusion of the charge carriers becomes the dominant transport process. The charge carriers move much slower towards the potential well and the charge carriers also partly recombine. Therefore no signal is induced in the readout chip. Additionally, the charge carriers are spread over more pixel cells due to the lateral diffusion. Only above 12 V, is the full sensor depleted allowing a complete collection of produced electron-hole pairs in the sensor. In the following chapter, the diffusion and the mobility of the charge carriers are studied in more detail.

### **Diffusion and Mobility of the Charge Carriers**

By recording the average cluster sizes at different bias voltages another effect in the bias scan study could be observed: When the sensor was illuminated with the 679 nm laser light, an increase of the average cluster size up to 3 was observed for the bias voltage setting from 15 to 30 V. As stated above, in the case of the 679 nm laser the charge carriers are generated only close to the back-side of the sensor. An incoming alpha-particle would have a similar ionization effect in the silicon sensor. The induced charge carriers have a longer drift distance to the potential well: almost the complete thickness of the sensor (200  $\mu\text{m}$ ). And therefore the lateral diffusion of the charge carriers has a larger effect and causes an increase of the average cluster sizes. This effect was not observed with the longer wavelength lasers, where the light can penetrate deeper into the silicon and the charge is induced uniformly along the beam path.

The cluster form was composed of the illuminated pixel cell and the adjacent pixel cells in the short direction. At higher bias voltages the drift velocity of the charge carriers increases and dominates the effect of the diffusion. The result of this is a decrease of the average cluster size at higher voltages (50 V) and can be seen in Figure 6.26.

These results are a confirmation of the study on the diffusion of the charge carriers during the beam tests 2002 and 2003. Then the number of hits with a cluster size 1 and 2 were investigated for different bias voltages. Cluster size 1 is defined as a single pixel hit and cluster size 2 as an event in which two adjacent pixel cells fired. In 2003 a 300  $\mu\text{m}$  silicon sensor was used and the bias voltage was scanned from 0 to 80 V, while in 2004, a 200  $\mu\text{m}$  sensor was irradiated and the bias voltage was only scanned until full depletion at 15 V, due to the break down of the leakage current at higher voltages. Figure 6.27 shows the results of this beam test study. In both diagrams, an increase of the hits with the cluster size 2 can be observed if the bias voltage is increased, while the hits with cluster size 1 are decreasing confirming the results obtained with the laser setup and shown in Figure 6.26.

The effect of the electrical field in the silicon sensor on the mobility of the charge carriers could be studied. For different bias voltages the collection time of the charge carriers was recorded within delay scans. As explained in chapter 1.3.1 the time shift of the readout efficiency curves can be directly correlated to the signal rise time in the chip and thus to the mobility of the charge carriers. In Figure 6.28 the readout efficiency is plotted as a function of the laser pulse delay for different bias voltages (20 - 170V). The depletion voltage was measured to be 12 V (see Figure 6.26). From these results, a relative difference in the mobility of the charge carriers

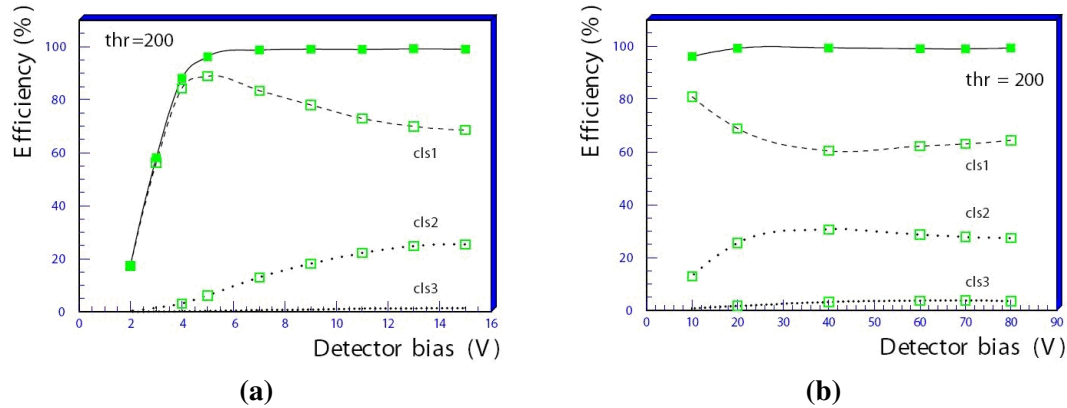


Figure 6.27: Average cluster size as a function of the bias voltage from beam test data 2002. The left plot (a) shows the results for the 300  $\mu\text{m}$  thick sensor and the plot the right (b) the results for the 200  $\mu\text{m}$  sensor. [92]

can be calculated. The delay of the readout efficiency curves for each bias voltage setting in respect to the curve at bias setting of 20 V was plotted in Figure 6.29. One can observe that the drift velocity enters a saturation range above a bias voltage of 100 V which corresponds to 5 kV/cm.

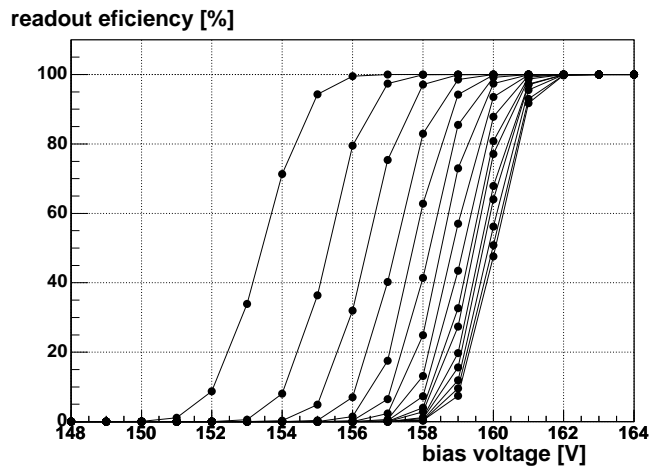


Figure 6.28: Delay of the S-curves at different bias voltage settings (20 V - 170 V)

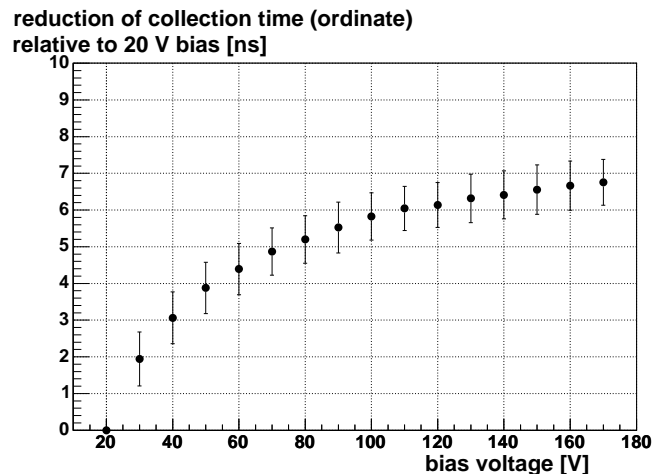


Figure 6.29: Reduction of charge carrier collection time which is proportional to the mobility of minority charge carriers measured during a bias voltage scan. The difference in the time of the signal generation is plotted with respect to the hit generation at bias voltage setting of 20 V. The depletion voltage amounts to 12 V.

## 6.6 FastOr-Study

The FastOr signal of the SPD is part of the L0 trigger and is particularly relevant for the study of proton-proton collisions. The expected low multiplicity environment in the central region, where SPD covers the pseudorapidity range from -1.98 to +1.98 (first layer) and -1.31 to +1.31 (second layer), calls for a trigger from the SPD. To understand if the FastOr signal can be generated quickly enough to arrive at the central trigger processor (CTP) in time for the L0 trigger decision, it was necessary to characterize and understand the FastOr signal as well as to produce an estimate on the time the chip requires to generate the FastOr signal upon registration of a hit. Using the laser setup different measurements on the FastOr signal could be performed. The position of the FastOr signal generation could be controlled by illuminating one or more pixel cells across the whole pixel matrix.

In the following chapter, the motivation for the FastOr signal as part of the L0 decision in ALICE pp collisions is explained. The measurements on the chip latency are described and a lower limit estimate on the chip latency is given. The results of the FastOr signal study under different FastOr DACs settings and depending on the position of the generation across the pixel matrix are presented. Further, the FastOr signal was examined during position scans across two pixel cells.

### 6.6.1 The FastOr Signal and the ALICE Trigger

The FastOr signal is a special feature of the SPD. Whenever a hit produces an above-threshold pulse it will close the FastOr circuit in the pixel readout cell generating the FastOr signal. This signal is produced after the threshold discrimination and sent off-detector without further processing in the readout cell allowing a fast response, hence the name FastOr. In chapter 3 the schematic block diagram of the ALICE1LHCB chip illustrates the generation of the FastOr signal. The individual cell signals are ORed together to generate a FastOr pulse at chip level. For each readout chip one FastOr signal is produced. Thus, the SPD can send 1200 independent FastOr signals, 800 from the outer and 400 from the inner layer<sup>5</sup>.

The expected high multiplicities during the heavy ion collisions and thus high occupancy in the two layers of SPD do not allow a minimum bias trigger for ALICE using the FastOr signal of SPD<sup>6</sup>. In the low multiplicity environment of the proton-proton collisions however, the FastOr signal of the SPD could serve as a part of the L0 trigger decision. SPD shows a high acceptance in the central region as it can be seen in Figure 6.30.

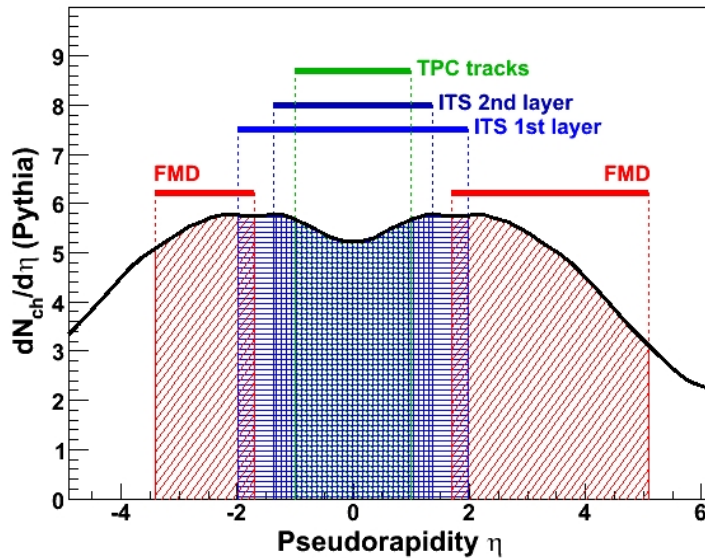


Figure 6.30: The pseudorapidity acceptance of different ALICE sub-detectors. [96]

Seven different trigger algorithms for combining the generated FastOr signals were studied by J. Conrad et al in [96]. These were:

- Global FastOR: An OR of all FastOr signals from the SPD.
- Layer: Per SPD layer one FastOr signal is generated.

<sup>5</sup>The SPD consists of two layers: inner at 3.9 cm and outer at 7.6 cm (see chapter 3)

<sup>6</sup>The possibility of a multiplicity trigger for heavy ion collisions is discussed below.

- Sector : A FastOr signal from one of the inner two staves of one sector together with at least one FastOr signal from the outer layer of the same sector is required.
- Half Sector: A coincidence of FastOr signals coming from one staffe of the first layer and the corresponding two staves of the outer layer is required.
- Sliding Window: FastOr signals coming from one staffe of the inner layer are correlated to 5 corresponding staves of the outer layer, while the staves from the outer layer are situated symmetrically in  $\varphi$  around the staffe in the inner layer.
- Vertex: Additional to the  $\varphi$ -coincidence trigger algorithms. Depending on the beam interaction area, the FastOr signal coming form the inner layer is correlated with in z-direction geometrically possible hits in SPD chips in the outer layer.
- Upper Cut: An upper cut on the FastOr occupancy can be set. This trigger algorithm can be used as the high multiplicity trigger in heavy ion collisions.

For this study 60 000 fully reconstructed pp-events were generated with PYTHIA [97] and analyzed. In Table 6.5 the efficiencies of the different trigger algorithms are presented for different process types, while in Figure 6.31 the efficiencies of two trigger algorithms (Global FastOr and Sector) are correlated to the multiplicity distributions of charged particles. As it can be seen the global FastOr trigger has the best efficiency. It is 100% efficient for one or more charged particles within  $|\eta| < 1.5$ . The simulations show that the FastOr electronics will only need 5 ns for the generation of this trigger although the algorithm will not be the limiting factor as was shown by A. Kluge [98].

Process	GL.FO	LAYER	SEC	HALF SEC	SW	VER	UPP. CUT
Non-diffractive Inelastic							
$qq \rightarrow qq$	96.6	94.7	93.4	93.1	93.7	92.9	82.8
$qg \rightarrow qg$	100	100	100	100	100	99.7	47.9
$gg \rightarrow qq$	100	100	100	100			
$gg \rightarrow qg$	99.9	99.7	99.7	99.7	100	100	54.5
<i>TotalND</i>	99.1	98.6	98.3	98.2	98.4	98.2	57
Diffractive							
$pp \rightarrow pY$	59.8	56.2	56.2	54.3	56.2	54.8	55.7
$pp \rightarrow Xp$	60.1	56.8	56.3	55.9	56.3	55.9	56.3
$pp \rightarrow XY$	69.6	62.0	59.9	58.7	60.8	58.4	62.0
<i>TotalDif</i>	64.1	58.9	57.8	56.6	58.2	56.6	58.6
<i>Allinelastic</i>	88.0	86.0	85.5	85.0	85.6	85.0	57.5

Table 6.5: Efficiencies of different FastOr algorithms for pp fully simulated PYTHIA events. The "UPPER CUT" algorithm was tuned to give high efficiencies for low multiplicities, hence therefore smaller efficiencies compared to other algorithms. [96]

The layout of the FastOr trigger architecture is schematically explained in Figure 6.32. It involves ten receiver cards, one processor card called BRAIN and one FPGA chip. Data from

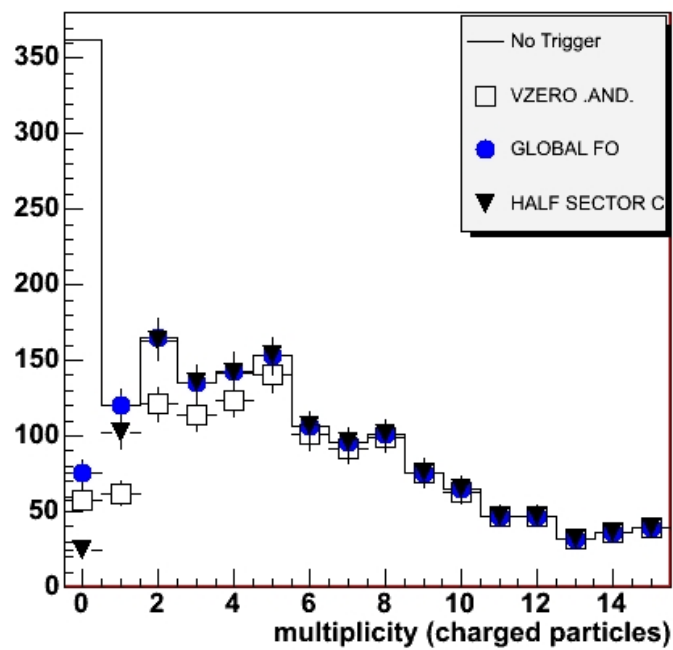


Figure 6.31: The efficiencies of two different FastOr trigger algorithms for different multiplicity distributions of charged particles compared to the VZERO .AND. trigger algorithm. The GLOBAL FastOr trigger shows the highest efficiencies in the investigated range of the multiplicity of the charged particles. [96]

12 half-staves is collected via 800 MHz optical links in one receiver card, where the deserialization and FastOr signal extraction is performed. Each of the 10 receiver cards sends the extracted FastOr signals from the 12 half-staves via a 2.4 GHz Multi Gigabit serial link to the processor card with the FPGA chip, where the FastOr algorithm generates the FastOr trigger signal. Since the trigger algorithm is located in one FPGA, the FastOr trigger is not dependent on the system architecture.

An important factor in the implementation of the FastOr as a part of the L0 trigger is the time constraint on the formation of the L0 trigger. The overall requirement for the L0-trigger to reach the Front end electronics of the ALICE detector systems is  $1.2 \mu\text{s}$ . Considering the latency of the Central Trigger Processor (CTP) and the transfer time to the read-outs, which amounts to about 300 ns, the FastOr signal has to be generated and transferred to the CTP within 900 ns. In Figure 6.32 and Table 6.6 the different delay factors in the generation and transfer of the FastOr signal are shown. In total 875 ns will be required to generate the L0 trigger with the FastOr signal, which is slightly below the limiting 900 ns.

The FastOr signal can not be correlated to a specific bunch crossing (25 ns) due to the signal integration of 100 ns corresponding to a 1 clock cycle of the pixel system clock. Therefore a bunch crossing identification will not be possible with a FastOr signal as part of the L0-trigger. Taking this into account, a minimum bias trigger for the pp-collisions with the FastOR signal is feasible. The chip latency, as it can be seen in chapter 6.6.2 was measured to be below 200 ns and does not introduce a significant delay in the formation of the chip latency. The FastOr signal has a good efficiency for inelastic events especially at low multiplicity.

The use of the FastOr signal as the minimum bias trigger opens many possibilities to select required events:

- Multiplicity trigger: The FastOr signal could be used as to select high multiplicity events in the central region to enrich pp data sample.
- HMPID trigger: The High Momentum Particle Identification Detector (HMPID) does not cover the complete  $\varphi$ -phase of the ALICE detector. The FastOr trigger could select events pointing towards the HMPID in order to allow more tracks involving the data from this detector.
- JET trigger: Requiring FastOr signals from two or more adjacent pixel chips would possibly allow triggering on particle jets.

### 6.6.2 Chip Latency Measurements

The chip latency together with the event to pixel chip capture it is constrained to less than 300 ns. The event to pixel chip capture results from the fact that the FastOr signal is sent synchronously with the clock. Depending on the time of the hit registration, the event to pixel chip capture can vary from 0 ns to 100 ns. The chip latency is the time the readout chip needs to generate the FastOr signal after hit registration.

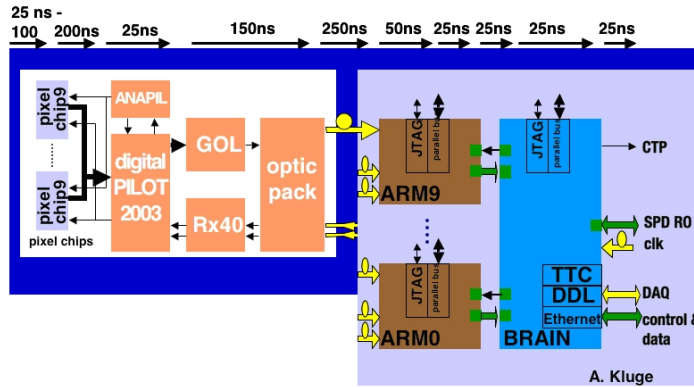


Figure 6.32: Layout of the FastOr trigger logic. Data from 12 half-staves are collected on one receiver card (ARM) using an 800 MHz optical link. Each of the 10 ARM processors sends the FastOr signal to the processor card (BRAIN) via a 2.4 GHz serial link. The trigger algorithm is located in one FPGA on the processor card, which generates the FastOr trigger. [98]

Latency Path	Latency time [ns]
Event to pixel chip capture Max.	100 ns
Pixel chip latency	200 ns
Pilot chip resynchronization	25 ns
Pilot chip - Serialization - Deserialization (GOL-HDMP 1034)	150 ns
Data Transmission on fiber (50 m * 5 ns)	250 ns
Resynchronization and delay adjust in FastOr ARM	50 ns
Data serialization in FastOr ARM	25 ns
Transmission to FastOr Brain	25 ns
Processing in FastOr Brain	25 ns
Transmission to Central Trigger Processor CTP	25 ns
<b>Total</b>	<b>875 ns</b>

Table 6.6: The estimated latency path. The event to pixel chip capture together with the pixel chip latency should be less than 300 ns. [98]

Disregarding the data transmission time via fibers, which is well known, the biggest factor in the latency path is the pixel chip latency (see Table 6). Therefore it is important to know, how large the chip latency is and how close to the clock edge the hit can be registered without generating the FastOr signal in the next clock cycle. The pixel chip latency could be for the first time measured using the laser setup and its feature to delay the laser pulse in 1 ns steps. For this purpose the time difference between the registrations of the laser pulse and the FastOr signal were recorded with a 1GHz LeCroy 9374M oscilloscope. The 20% fiber which is brought to the SPD assembly is attenuated and prolonged with an extra 3 m long FC/LC optical fiber. The second 20% fiber is brought to the O/E converter, which was directly connected to the oscilloscope.

The delay between the two laser pulses is caused by the three attenuators (measured to be  $0.41 \pm 0.29$  ns) and the 3 m long FC/LC fiber. The FastOr signal was collected at the chip card with the oscilloscope probe PP005a from LeCroy, which had a delay of  $7.47 \pm 0.02$  ns. The O/E converter generating the laser pulse on the oscilloscope and thus the reference for the chip latency measurement adds an extra delay, which could not be exactly measured, but was estimated to be less than 20 ns. Therefore only a lower limit on the chip latency can be given. From the measured value of the chip latency the extra delay of the 3 m long fiber and the attenuators are subtracted and the estimated delay of the TTI optical head and the delay caused by the oscilloscope probe is added.

In Figure 6.33 the results on the chip latency measurements are presented. The corrected lower limit of the distance of the FastOr signal to the laser pulse is plotted as function of the laser pulse delay. The laser pulse was shifted in 1 ns to cover the strobe signal of the chip, which is used as the reference for the measurements. The strobe signal has a fixed relation with the clock signal, i.e. it is synchronous with the clock, and it generates the readout of the chip. It could be measured via the efficiency of the readout, which is defined as the number of registered hits divided by the number of sent triggers.

As the laser pulse is shifted, the delay of the FastOr signal is reduced linearly. This is due to the event to pixel chip capture. If the laser pulse arrives within one clock cycle, the FastOr signal is always sent at the same time. Hence, the time distance between the laser pulse and the FastOr signal decreases in steps of the delay of the laser pulse. As soon as the laser pulse comes close to the edge of the clock the FastOr signal becomes unstable, jumping 100 ns back and forth. This transition time from one clock cycle to the next is measured to be less than 6 ns. After this transition time the FastOr signal becomes stable again. During one clock cycle, the FastOR delay is reduced by 100 ns, which corresponds exactly to one clock cycle and thus to the pixel to chip capture contribution to the FastOr delay.

When the laser pulse is shifted close to the clock cycle transition, the pixel to chip capture is close to zero and the remaining contributing factor to the FastOr delay is the chip latency. Due to the instability of the FastOr signal during the clock cycle transition time, the contribution from the pixel to chip latency is not exactly zero, and therefore an exact measurement of the pixel chip latency is not possible, but only an estimate on the higher limit. The lowest measured value of the FastOr delay and thus, the pixel chip latency is measured to be  $199.4 \pm 0.3$  ns.

To confirm the repeatability of the measurement, the time difference between the FastOr signal

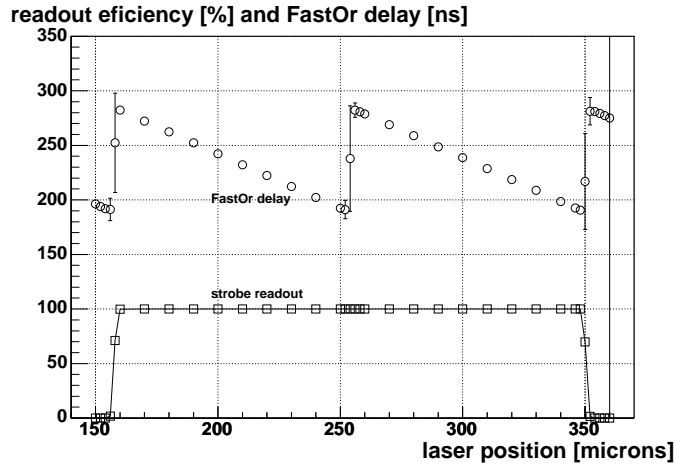


Figure 6.33: The chip latency. The upper curve shows the chip latency as the laser pulse is delayed towards the strobe signal, which is shown in the lower curve.

and the laser pulse at a delay setting of 160 ns is measured 25 times on two separate days under the same conditions, while the laser, the pulse generator and the SPD test readout system were turned off between the measurements. The laser pulse delay of 160 ns was chosen due to its closeness to the clock cycle transition time. The FastOr signal was delayed by 291.14 ns in average stable within 0.39 ns, what ensured a repeatability of this measurement. The clock cycle transition time was always measured to be less than 6 ns. The width of the FastOr signal stayed always constant during the measurements amounting to  $39.25 \pm 0.27$  ns.

Using the laser setup, the chip latency and the pixel to chip capture could be measured for the first time. The chip latency was verified to be less than 200 ns, which confirms the estimations from the chip design. Thus, the chip latency will not be the limiting factor for the FastOr trigger.

### 6.6.3 FastOr-Signal

#### OnChip FastOr-DAC Settings

The intensity of the current injected in the FastOr circuit is controlled by the Fast-CONVPOL DAC and the threshold for the FastOr signal can be changed using the Fast-COMPREF DAC (Figure 6.34). These on-chip DACs can be adjusted externally via the JTAG chain. Figure 32:

The signal width was studied as a function of the two DAC settings (Figure 6.35) in order to find an optimum working point.

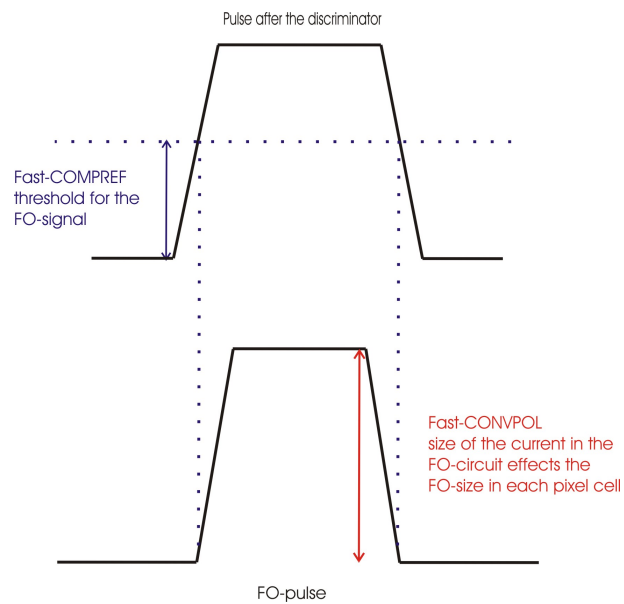


Figure 6.34: Illustration of the effect of the two FastOr DACs on the width of the FastOr signal. At higher FastOr threshold (controlled by Fast-COMPREF) the width of the FastOr signal is smaller and by increased amount of the FastOr current in the FastOr circuit (controlled by Fast-CONVPOL) the signal becomes wider.

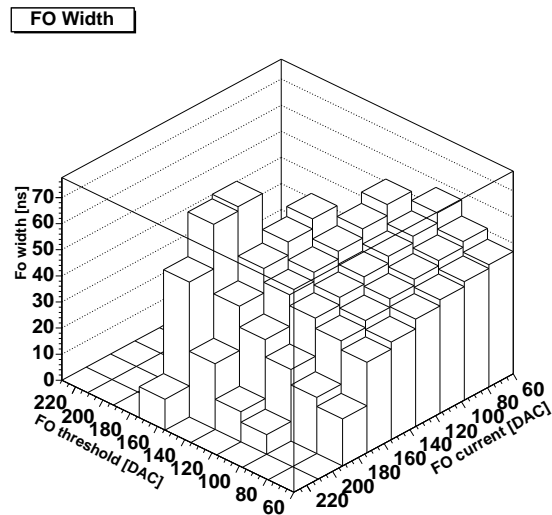


Figure 6.35: Width of the FO signal vs different settings of Fast-CONVPOL and Fast-COMPREF. The laser pulse generates  $\sim 8600 e^-$ ; the threshold DAC setting is  $\sim 2900 e^-$ .

It can be seen that the width of the FastOr signal increases if the Fast-CONVPOL is decreased, which corresponds to an increase of the current in the FastOr circuit. A wider FastOr signal can also be seen in case of a lower threshold (higher Fast-COMPREF DAC value). From Figure 6.35 an optimum working point for the two FastOr DACs was found. The width of the FastOr signal is stable for a setting from 60 to 140 for both DACs. A setting above 180 for the Fast-COMPREF DAC results in a noisy FastOr signal.

### Homogeneity Study

Setting the FastOr DACs at the optimum working point, a scan over the full pixel matrix was performed. The width of the FastOr signal of different pixel cells was measured in steps of 20 pixels in the  $r\phi$ -direction ( $20 * 50 \mu\text{m}$ ) and in steps of 5 columns in the  $z$ -direction ( $5 * 425 \mu\text{m}$ ) of the pixel matrix. Extra measurement points in the  $z$ -direction were made in order to cover for the test-columns in the pixel matrix (See chapter 2). In Figure 6.36 the result of this scan can be seen.

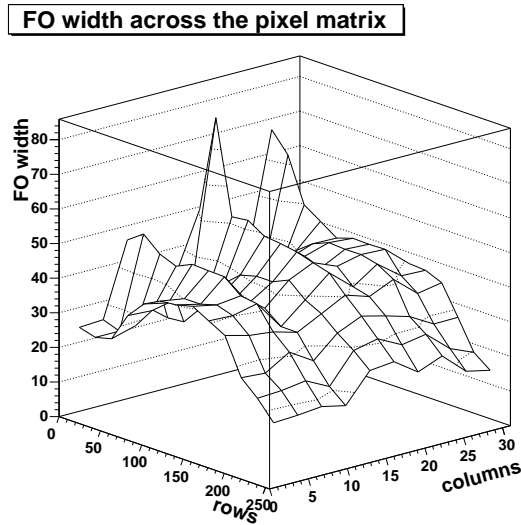


Figure 6.36: The width of the FastOr signal across the pixel matrix.  $\sim 8600 e^-$  were induced at a threshold setting of  $\sim 2900 e^-$ .

In the center of the pixel matrix the FastOr signal is wider compared to the edges. Another interesting outcome is the wider width of the FastOr signal in the beginning of the test columns. This effect is not yet understood, but it seems to correlate with the test-columns problems observed during the chip wafer and ladder testing (See chapter 4).

Although this effect is not yet completely understood, it is not of great importance, since the width of the FastOr signal has no effect on the FastOr trigger.

### Charge Sharing Effect

Charge sharing in two adjacent pixel cells results in a widening of the FastOr signal. The effect is shown in Figure 6.37 where the width of the FastOr signal is plotted as a function of the position of the laser spot. It is observed that the stability of the width of the FastOr signal in this case gets worse. This is due to the fact that the input charge is close to the threshold level. In Figure 6.38 the same effect can be observed when the laser pulse amplitude is increased. The charge sharing causes two pixels to fire and thus increases the FO signal length.

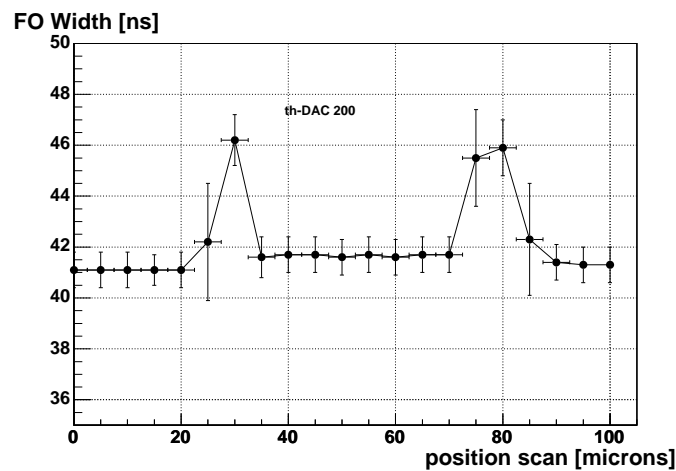


Figure 6.37: The width of the FastOr signal is plotted as function of the position of the laser spot. An increase is visible if the laser light penetrates the Si-sensor between two pixels thus increasing the FastOr signal length at chip level. About 8600 electrons were generated by the laser pulse and the threshold was set to  $\sim 2900 e^-$ .

### FastOr Efficiency

If the FastOr signal is to be used as a part of the L0-trigger, also the efficiency of the FastOr is very important and was therefore studied using the laser test system. A defined number of triggers was sent to the laser and compared to the number of the generated FastOr signals. The FastOr efficiency is defined as the ration of the number of generated FastOr signals and the number of sent laser pulses. Two sets of measurements were performed for this purpose. First, the FastOr efficiency was studied as a function of the threshold DAC settings. In Table 6.7 and Figure 6.39 the result of this study is shown. The laser bias voltage was set to induce 8600 electron-hole pairs in the silicon sensor. The FastOr efficiency was measured to be higher than 99.99%. At lower thresholds the FastOr efficiency decreases as expected. In the second set of measurements, the FastOr efficiency was measured across the pixel matrix. Different pixel

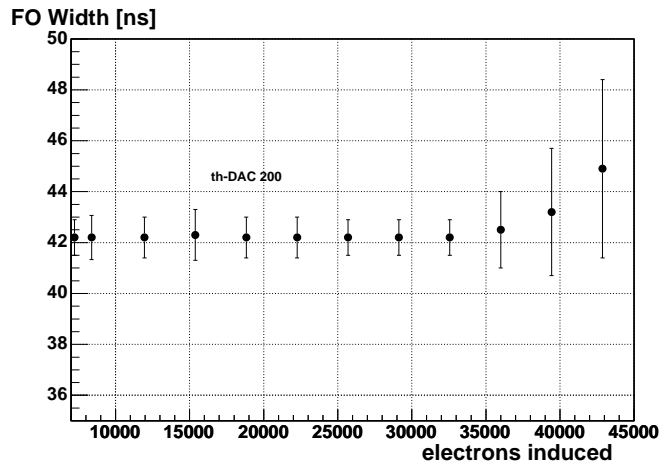


Figure 6.38: FastOr signal as function of the laser energy. The threshold was set to  $\sim 2900 e^-$ .

Threshold setting [DAC]	Sent triggers	Generated FastOr signals	FastOr eff. [%]
217	50832	50827	99.99
200	50515	50512	99.99
180	50688	50681	99.99
160	53127	53122	99.99
140	50920	23635	46.416
130	53899	27	0.05
120	57277	7	0.01

Table 6.7: FastOr efficiencies for different threshold settings. The number of generated FastOr triggers is compared to the number of sent laser pulses. The FastOr is efficient to 99.99% for thresholds below the set laser energy.

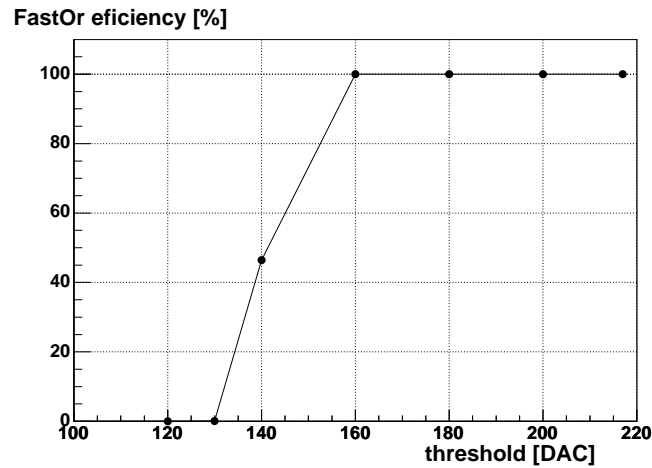


Figure 6.39: Efficiency of the FastOr signal as a function of the threshold. The DAC setting is inverse proportional to the threshold.

Pixel cell (col/row)	Sent triggers	Generated FO signals	FastOr eff [%]	
10/30	30514	30507	99.98	
30/30	30484	30478	99.98	
27/30	30460	30458	99.99	
9/200	30514	30505	99.97	Test col
9/30	30752	33321	108.35	Test col
1/30	30866	30158	97.71	Test col
17/30	30525	30528	100.01	Test col
17/10	32385	32391	100.02	Test col
9/5	60420	64772	107.21	Test col

Table 6.8: FastOr efficiencies for different pixel cells across the pixel matrix. The pixel cells in the lower part of the test columns are over efficient. Same behavior is observed in Figure 33. This is a well known problem, also occurring during thresholds scans in the production tests.

cells, in particular in the test columns were illuminated. These results are summarized in Table 6.8. One can see that as in the study of the FastOr width across the pixel matrix, the pixel cells in the test columns give a different outcome than the others. The FastOr is over efficient, if charge is induced in those pixel cells.

## 6.7 Summary

The pulsed infrared laser test system, which I developed in the framework of my doctoral thesis, was used to characterize the ALICE Silicon Pixel Detector. [99] The light pulse simulates the passage of a particle through the sensor and can be adjusted in amplitude. The calibration of the laser was explained in detail in chapter 6.4. For these measurements I also performed the absolute calibration of the detector using radioactive sources.

By varying the laser energy, the time walk of the discriminator could be studied. Further, the sensitive pixel area was examined by means of position scans and threshold variations. The effect of the aluminum vias on the charge collection efficiency, when the laser energy was close to the threshold, was observed and explained. Increasing the bias voltage straightened the filed lines in the sensor, which lead to a better charge carrier collection and as such to the decrease of this effect.

From the charge sharing studies I could derive an estimate of the spatial resolution for the two-pixel clusters which is in good agreement with the analysis of beam test data. Bias scans provided the possibility to study the diffusion and mobility of the charge carriers in the SPD sensor.

In view of the fact that the Pixel Trigger (PIT) will be used as a part of the L0-trigger decision, I carried out an extensive study of the FastOr signal of the Alice SPD. Using the laser setup an independent measurement of the chip latency was possible for the first time. These results enabled the understanding of the behavior of the FastOr signal under different operating conditions and provided a reference measurement for the optimization of the FastOr DACs.

## Chapter 7

# Conclusions

The presented work deals with the ALICE Silicon Pixel Detector System. ALICE is the dedicated experiment for the study of heavy ion collisions at the LHC. The ALICE SPD constitutes the two innermost layers of the detector at close vicinity to the interaction point. Due to its high granularity and small pixel cell size, it will provide precise tracking information of primary and secondary vertices. It has in total 9.8 million channels and the pixel cells measure  $50\ \mu\text{m}$  in the  $r\varphi$ -direction and  $425\ \mu\text{m}$  in the  $z$ -direction arranged in 32 columns and 256 rows in a readout chip. One silicon sensor is flip-chip bonded to 5 readout chips forming one ladder, of which two pieces are connected via an AI-bus with a Multi Chip Module (MCM).

The in the chip internally generated analog FastOr signal will contribute to the L0 trigger decision in the ALICE proton-proton program. Thus, a large scale HEP experiment will for the first time use tracking information close to the interaction point for low level triggering.

An introduction to CERN and its LHC program is given in chapter 1, where also the ALICE experiment, its goals and the contributions from the ITS and in particular from the SPD are explained. In chapter 2 the working principle of the silicon detectors is briefly sketched and the deployment of the hybrid pixel detectors in LHC experiments is depicted. Chapter 3 gives a detailed description of the different components of the ALICE SPD, the detector electronics and the production process.

This thesis is based on three topics:

- Quality assurance tests and protocols of the ALICE SPD components (readout wafer and ladders)
- Analysis of prototype detector modules in particle beams
- Development of an infra-red laser test system and measurements on ALICE SPD assemblies

The functionality and performance testing of SPD ladders, readout wafers and sensors were

performed on a SUSS probe station at CERN. These tests include visual and electrical inspection of sensor wafers of which each contains sensors for five SPD ladders and 13 SPD singles. The mechanical defects, the alignment of the position markers and the leakage currents are examined in detail to extract information on the sensor wafer process. Further, the testing of the SPD readout wafers to select KGD (Known Good Die) for bump bonding according to the established selection criteria and measurements of ladders and single assemblies using the internal test pulse generator as well as a  $^{90}\text{Sr}$ -source in order to determine the potential bump bonding defects were performed. The readout wafers show good yield in the order of 52% class I chips on average. The production of the SPD ladders, which show an average yield of 66% with a very good bump bonding yield of less than 1% defect pixel cells for most readout chips, is well under way and should be accomplished by August 2006.

As a result of detailed quality assurance measurements back-side aluminum layer delamination effects were observed in some of the new  $\text{SiO}_2$  passivated wafers. Investigations of this effect involved in particular studies using a Scanning Electron Microscope (SEM) in the TS-MME group. This systematic work has been a decisive factor for the identification of the delamination problem, which due to the introducing of an additional cleaning and protection step in the sensor wafer production is now under control and has not appeared since.

Open contacts in the corner of the chips resulting from bowl like shape of the readout chips were observed temporarily during ladder tests. By means of metrology measurements this mechanical deformations could be studied in detail. Immediate feedback of these results and close contact with bonding foundry have prevented further occurrence since then.

During two beam tests in 2003 and 2004 extensive tests of ALICE SPD prototypes was performed. In 2003 a SPD assembly was illuminated with a heavy ion and a proton/pion beam. Four other SPD planes were used as tracking references. The plane under study had a  $300\ \mu\text{m}$  thick sensor. The ALICE SPD test system provided the detector control and the DAQ. In 2004 a joint beam test with two planes of each subdetector from the Inner Tracking System (ITS) took place. The SPD deployed 2 half-staves in the final configuration. A novel alignment method taking tilt and azimuthal angle into account was developed in order to be able to study the data taken at wide beam setting of the proton/pion beam. Using this method an intrinsic spatial resolution of the plane under study below  $10\ \mu\text{m}$  could be reached, which is comparable to the resolution achieved for focused beam setting. The spatial resolution of the detector was studied as function of the threshold and incidence angle.

The average cluster size as function of the track incidence angle was studied also for both detector thicknesses ( $300\ \mu\text{m}$  in 2003 and  $200\ \mu\text{m}$  in 2004) and showed the expected behavior. For the 2003 data, a comparison of the cluster sizes for the focused and the wide setting of the proton beam could be performed. The results indicate a uniform response of the pixel matrix.

A test system based on an infra-red laser was developed in order to test SPD single assemblies and in particular the FastOr signal. The setup allowed a detailed study of the ALICE1LHCB chip characteristics with well defined timing and energy deposition in the silicon sensor. The time walk of the discriminator could be investigated and a study of the size of the sensitive pixel area as function of the threshold could be performed. By using three different laser wavelengths the charge sharing between two adjacent pixel cells and the diffusion and mobility of charge

carriers was studied. The optimum working point and the performance of the FastOr signal was characterized. The chip latency, i.e. the time the chip needs to generate the FastOr signal after the ionization process, was measured directly for the first time.

The results presented in this thesis illustrate the production phase of the SPD and the measurements performed in order to qualify components for inclusion in the detector and to characterize the detector performance.



## **Appendix A**

# **Scanning Electron Microscopy Functionality**

### **A.1 Introduction**

The theoretical limit for the resolution of an optical microscope is one half of the wavelength in the medium used. That means, even with UV-light and under optimal conditions, optical microscopes can reach only a resolution of 100 nm. It is not possible to use radiation with even smaller wavelength as X-rays due to the lack of focusing lenses and other optics for such hard photons.

De Broglie introduced his theory that all particles have a wave-like nature and that electron waves assuming high enough energy will have a wavelength in the range of 5 pm. Finally in 1926 when Busch developed axially symmetric electromagnetic lenses, it was possible to focus electrons and use them for imaging of objects. Using the electron microscope the resolution could be improved by a factor 100 000 [100]. In the following section the functionality principle of the scanning electron microscope will be described shortly. We used the SEM for the study of the back-side aluminium adhesion problem (see chapter 4).

### **A.2 Working Principle**

The Scanning Electron Microscope (SEM) consists of an electron gun, an aperture, focusing magnetic lenses, scanning magnetic lenses and two types of electron detectors. All these components form the Electron Optical Column, which needs to be kept under vacuum. For comparison: a 50 kV electron beam will be stopped by 20 cm of air. In Figure A.1 the schematic view of the Electron Optical Column is presented.

In the electron gun, voltage is applied to a filament, which can be made of different materials.

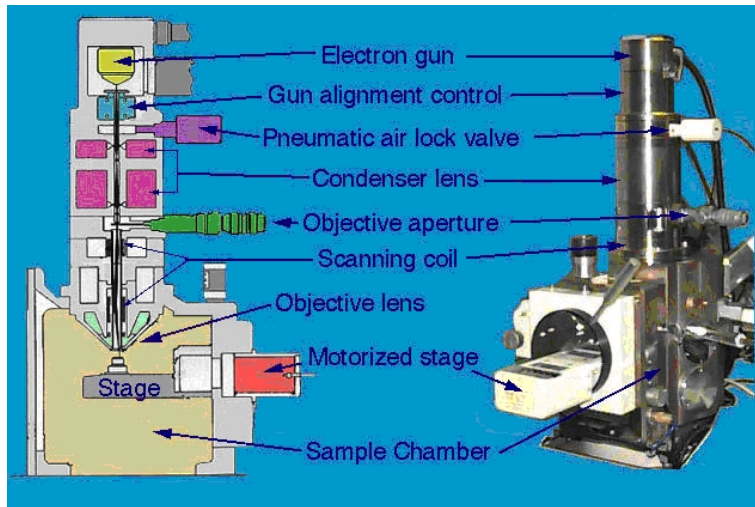


Figure A.1: Illustration of the Electron Optical Column. [101]

Tungsten is however widely used filament material. The filament is heated up and emits electrons. These are then accelerated towards the anode, which is at a positive potential with respect to the filament. The anode passes the electrons further down the Optical Column to the condensing magnetic lenses. When electrons pass between those axially symmetric magnets they experience a repelling force from the magnets. Only in the optical axis, exactly in the middle of the magnets, the electrical field and therefore the force on the electrons is zero. Since the force on the off-axis electrons is always perpendicular to the field and to the original direction of motion, they are spiraling around and towards the optical axis. In Figure A.2 the principle of magnetic lenses is illustrated.

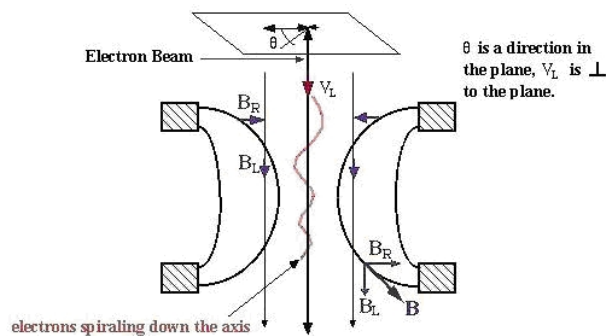


Figure A.2: Principle of the magnetic lenses. [101]

The so focused electrons are then hitting the sample. With the same principle as in a TV-screen the scanning magnets just above the sample force the electrons to scan over the chosen part of the surface of the sample. This way a picture and also the composition of the surface can be

visualized. When electrons hit the surface they penetrate into it and react with the atoms of the sample. The penetration depth depends on the energy of the electrons and the incident angle. Two main reactions with the atoms are elastic and inelastic scattering. In case of elastic scattering the electrons react with the atomic nucleus and are backscattered. With a detector around the primary electron beam (Backscattered Electron Detector) the out coming electrons are collected and read out. Since the number of the backscattered electrons (BSE) is proportional to the size of the nucleus, also an image showing different elements present in the sample can be produced.

In case of an inelastic reaction, the incoming electrons transfer a part of their kinetic energy on the electrons of the sample throwing them out of the sample. These electrons are then collected on the Secondary Electrons Detector.

An Energy Dispersive Detector, sensitive to the fluorescent radiation, allows a qualitative analysis of the surface of the sample. In Figure A.3 the three detectors can be seen.

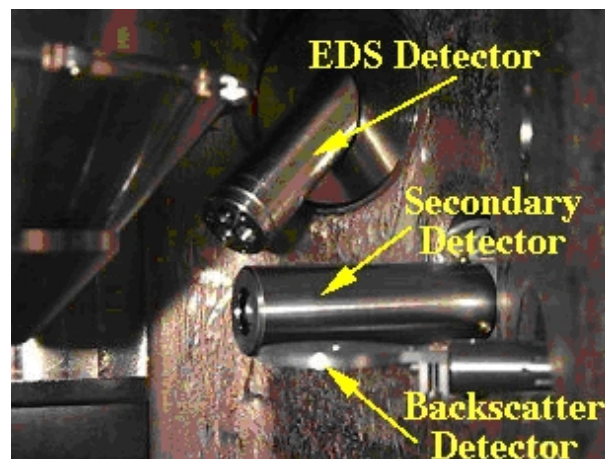


Figure A.3: Picture of the three detectors in a SEM. [101]

### A.3 Sample Preparation

The surface of the specimen needs to be conductive in order to transfer the incoming charge in form of electrons. The samples which are not conductive must be therefore coated with a conductive layer, for example with gold.

## A.4 Lens Defects

The magnetic lenses have the same defects as the optical lenses. However, the magnetic lens defects can not be corrected. The only possibility to avoid the spherical aberration, the chromatic aberration and the coma is to use a small aperture ( $10^{-2}$  to  $10^{-3}$  radians)[102] selecting only electrons close to the axis. The aperture is located below the condensing lenses. Even though only a small spot of the surface is radiated by the electron beam, the signal over noise ratio is sufficient

## Appendix B

# Geometry Setup for the Beam Test 2003

These are the geometrical setups for the test beam, showing the positions of the tracking planes in relation to the target and the beam. The size of the chips have been exaggerated. All numbers are in mm. The y-positions correspond to the measured distances to the center of the pixel chips (in the log book, all numbers are to the lower edge of the chip). The POSX/Y/Z values are to be used in the analysis software (to be inserted into the ana.par file for a corresponding run). The POSZ values have the origin at the position of the middle plane (Plane 2). Note that all POSX values are zero, since they were more or less impossible to measure. Alignment should take care of this. They will be off by a few mm. Setups #4-5 have the best measured y-positions. Overall the measure error is in the mm range.

Setup #1 has the planes out of position, and tracks can not be formed that pass through all planes. This was fixed in Setup #2. The complete file tree has information about which setup to use for each file. In general, the setups should be used for the dates written above each picture in the yellow fields.

In the raw data, chip 1 and chip 0 correspond to tracking plane 0 and 1 respectively, for the first minibus. In the second minibus, chip 1 and chip 0 correspond to tracking plane 3 and 4. The minibuses used during the proton beam had a rotated and mirrored geometry. For details, see the drawing below for Setup #3.

When Plane 5 can be used by the analysis software, add the corresponding numbers for the positions. Note that there are three different y-positions for this plane. The first setting for set too high for track correlations with the other planes, although some tracks were seen, the second setting was too high (no correlations at all), and the third was good ( $y = 69.4$  mm). The corresponding z-position is 322 mm.  $x = 0$ .

Position parameters for the analysis software for the Setup #2:

- POSX 0. 0. 0. 0. 0.
- POSY 38. 38. 83.3 142.1 142.1
- POSZ -345. -325. 0. 423. 445.

Position parameters for the analysis software for the Setup #3:

- POSX 0. 0. 0. 0. 0.
- POSY 0. 0. 0. 0. 0.
- POSZ -345. -325. 0. 423. 445.

Position parameters for the analysis software for the Setup #4:

- POSX 0. 0. 0. 0. 0.
- POSY 37.4 38.4 44.4 44.9 46.4
- POSZ -88. -67. 0. 29. 50.

Position parameters for the analysis software for the Setup #5:

- POSX 0. 0. 0. 0. 0.
- POSY 36.4 36.4 43.4 42.4 42.4
- POSZ -88. -67. 0. 29. 50.

When Plane 5 can be used by the analysis software, add the corresponding numbers for the positions,  $x = 0.$ ,  $y = 69.4$  and  $z = 322.$

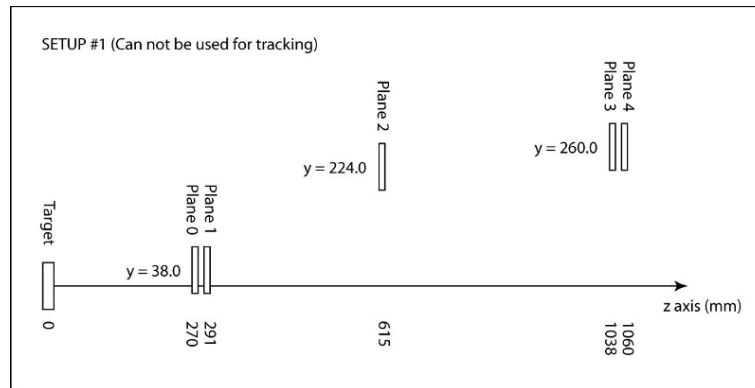


Figure B.1: SETUP #1: To be used with data from October 27, 2003 to October 29, 2003. The planes are in the wrong positions for tracking.

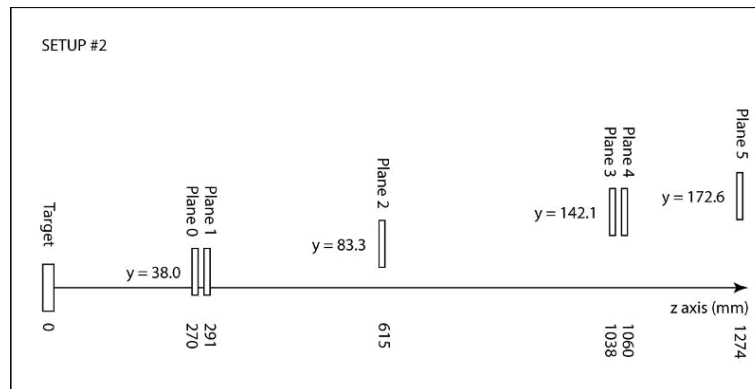


Figure B.2: SETUP #2: To be used with data from October 29, 2003 to October 31, 2003. Note that the Rudolf plane (Plane 5) has been introduced in the drawing. However, the raw data does NOT contain data from this plane. All planes are now in position for recording tracks.

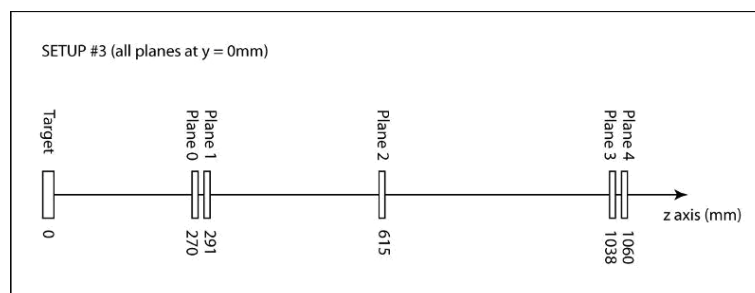


Figure B.3: SETUP #3: To be used with data from October 31, 2003 to November 3, 2003. Proton/Pion run. All planes are placed in the beam at  $y = 0$  mm. Rudolf plane still out of data. Coordinate system details can be found in 5.2. Note also that chip 1 and 0 corresponds to plane 0 and 1 (plane 3 and 4) for pilot 0 (2) respectively.

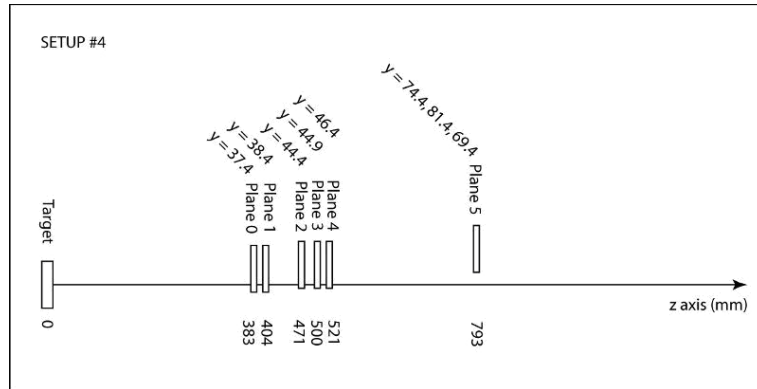


Figure B.4: SETUP #4: To be used with data from November 3, 2003 to November 5, 2003. There are now special data files with merged Plane 0-4 and Plane 5 data, although most files are with Plane 0-4.

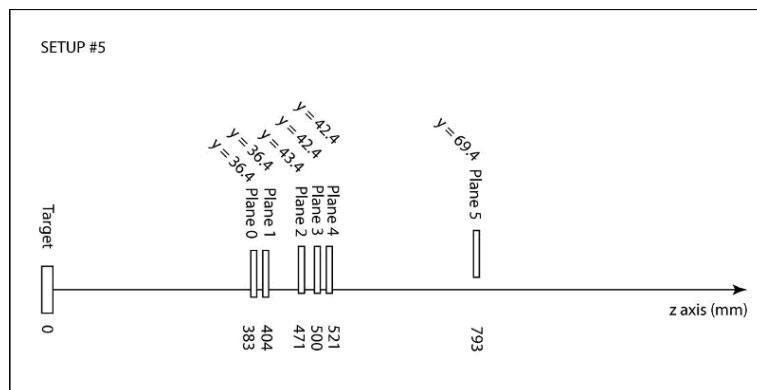


Figure B.5: SETUP #5: To be used with data from November 5, 2003. This is the final setup and should be used for the rest of the files. There is an uncertainty in the y-positions for Plane 3-4 (on the order of a few mm). Alignment should take care of this.

## Bibliography

- [1] W.Buchmüller: *Field Theory and the Standard Model*, Lecture at the European School of High Energy Physics 2005, Kitzbühel, Austria
- [2] P.W.Higgs: *Spontaneous Symmetry Breakdown without Massless Bosons*, Phys. Rev. 145, 1156-1163, 1966
- [3] J.Ellis: *Physics beyond the Standard Model*, Lecture at the European School of High Energy Physics 2005, Kitzbühel, Austria
- [4] LHC OUTREACH, <http://lhc-machine-outreach.web.cern.ch/lhc-machine-outreach/>
- [5] ALICE Collaboration: *ALICE Physics Performance Report Volume I*, CERN/LHCC 2003-049
- [6] H.Tydesjo: *Net-Charge Fluctuations in Ultra-Relativistic Nucleus-Nucleus Collisions*, PhD thesis, Department of Physics Lund University, 2004
- [7] J.-P.Revol et al.: *Day One Proton-Proton Physics with the ALICE Central Detector*, ALICE Internal Note, ALICE-INT-2000-28 v.1
- [8] ALICE Collaboration: *ALICE Technical Proposal*, CERN/LHCC/1995-71
- [9] <http://alice1.web.cern.ch/alice1/>
- [10] ALICE Collaboration: *Technical Design Report of the Inner Tracking System*, CERN/LHCC/1999-12
- [11] A.V.Kazak et al.: *Inner Tracking System – Cooling-Mechanics-Alignment*, St.Petersburg, 1999
- [12] ALICE Collaboration: *ALICE Physics Performance Report Volume II*, CERN/LHCC 2005-030
- [13] A.Morsch, B.Pastircak: *Radiation in ALICE Detectors and Electronic Racks*, ALICE Internal Note ALICE-INT-2002-28, 2002
- [14] A.Dainese: *Open heavy-flavour production in ALICE*, Presented at Hadron Collider Physics Symposium 2005, Les Diablerets, Switzerland, 2005
- [15] <http://www.britneyspears.ac>
- [16] Universitaet Siegen: *Compton Praktikum*, [ida1.physik.uni-siegen.de/praktikum/compt\\_e.pdf](http://ida1.physik.uni-siegen.de/praktikum/compt_e.pdf)
- [17] M.Krammer: *Detektoren, Wechselwirkung von Teilchen / Strahlung mit Materie*, Lectures at the Institute of High Energy Physics, Vienna, 2005
- [18] C.Gruppen: *Teilchendetektoren*, BI Wissenschaftsverlag, Mannheim 1993
- [19] Particle Data Group: *Particle Physics Booklet*, Elsevier, LBL and CERN, 2004
- [20] S.M.Sze: *Semiconductor devices: physics and technology*, Wiley 1985

- [21] <http://hyperphysics.phy-astr.gsu.edu/hbase/hframe.html>
- [22] L.Tlustos: *Performance and limitations of high granularity single photon processing X-ray imaging detectors*, PhD thesis, CERN-THESIS-2005-032, University of Technology Vienna, Austria, 2005
- [23] Silicon Lectures, [www.to.infn.it/activities/experiments/alice/presentazioni/lezioniSilicio2.ppt](http://www.to.infn.it/activities/experiments/alice/presentazioni/lezioniSilicio2.ppt), INFN Torino, Italy, 2006
- [24] I.Ropotar: *An investigation of silicon pixel tracking detectors and their application in a prototype vertex telescope in the CERN NA50 heavy-ion experiment*, PhD thesis, CERN, 2000
- [25] ATLAS collaboration, CERN, Geneva, Switzerland
- [26] CMS collaboration, CERN, Geneva, Switzerland
- [27] M.Winter: *R&D on Monolithic Active Pixel Sensors for the CBM Vertex Detector*, DOC-2005-Mar-59, CBM - GSI Annual Report, Germany, 2003
- [28] G.Gaycken: *Monolithic Active Pixel Sensors for Radiation tolerant fast Vertex Detectors*, contribution to the VERTEX 2004, Como, Italy, 2004
- [29] R.Kohrs et al.: *DEPFET Pixel vertex Detector for the ILC*, DESY PRC R&D, Germany, 2005
- [30] A.Kluge et al.: *The Alice Silicon Pixel Detector*, Proceedings of the 8th ICATPP, Como, Sept. 2003
- [31] A.Pepato: *The mechanics and cooling system for the ALICE Silicon Pixel Detector (SPD)*, proceedings of the PIXEL Conference Bonn, Germany, 2005
- [32] J.Hunen et al.: *Irradiation and SPD Beam Tests of the Alice/LHCb Pixel Chip*, 7<sup>th</sup> Workshop on Electronics for LHC Experiments, Stockholm, Sweden, 2001, ALICE-PUB-2001-15
- [33] M.Campbell: <http://www.cern.ch/mcampbell>
- [34] K.Wylie et al: *A pixel readout chip for tracking at ALICE and particle identification at LHCb*, LEB 99, Snowmass Colorado, 1999
- [35] *IEEE Standard Test Access Port and Boundary-Scan Architecture*, IEEE Std 1149.1-1990
- [36] W.Snoeys et al.: *Pixel readout electronics development for the ALICE pixel vertex and LHCb RICH detector*, Nucl. Instrum. Methods Phys. Res., A : 465 (2001) 176-189
- [37] B.Gunning: *A CMOS Low Voltage-Swing Transmission-Line Transceiver*, ISSCC Dig. Of Tech.Papers, 1992
- [38] P.Riedler: *Status and Overview of the ALICE Silicon Pixel Detectors*, proceedings of the PIXEL Conference Bonn, Germany, 2005
- [39] Canberra: *private communications*
- [40] VTT: *Centre for Microelectronics*, Finland, 2005
- [41] S.Savolainen-Pulli et al.: *Experiences in Flip Chip Production of Radiation Detectors*, proceedings of the PIXEL Conference Bonn, Germany, 2005
- [42] A.Kluge et al.: *The ALICE Silicon Pixel Detector Front-end and Read-out Electronics*, proceedings of the Vertex 2004, Como, submitted to NIM A

- [43] A.Kluge: *The ALICE Silicon Pixel Detector Front-end and Read-out Electronics*, ALICE Internal Note, ALICE-INT-2004-030
- [44] A.Boccardi et al.: *Integration and test of the ALICE SPD readout chain*, proceedings of the LECFC 2004
- [45] M.Morel: *The ALICE Pixel Detector Bus*, [http://home.cern.ch/Morel/pixel\\_carrier.pdf](http://home.cern.ch/Morel/pixel_carrier.pdf)
- [46] A.Kluge: *The read-out system of the ALICE pixel detector*, Proceeding of the Pixel 2002 Conference, SLAC Electronic Conference Proceedings, Carmel, USA, September 2002
- [47] See <http://www.vita.com/vmeproducts.html>
- [48] M.Krivda: <http://alice1.web.cern.ch/alice1/Router/index.htm>, Slovak Academy of Sciences, SK-04353 Kosice, Slovakia
- [49] R.Divia et al.: *Data Format over the ALICE DDL*, ALICE-INT-2002-010 V5.0, 2004
- [50] B.G.Taylor: - *Timing Distribution at LHC*, presented at the 8<sup>th</sup> Workshop on Electronics for LHC Experiments, CERN/LHCC/2002-034 (<http://ttc.web.cern.ch/ttc>)
- [51] ALICE Collaboration: *ALICE Technical Design Report, CERN-LHCC-2003-062 ALICE TDR 10, 2004*
- [52] M.Caselle et al.: *Assembly procedure of the module (half-stave) of the ALICE Silicon Pixel Detector*, Proceeding of the 9<sup>th</sup> Pisa Meeting on Advanced Detectors, published in Nuclear Instruments and Methods in Physics REasearch A, 501 (2003) p. 111-118, 2005
- [53] P.Riedler et al: *The ALICE Silicon Pixel Detector: System, Components and Test Procedures*, Proceedings of the 10 European Symposium on Semiconductor Detectors, Wildbad Kreuth, Germany, 2005, Accepted for publication in NIM A, 2005
- [54] INFN Bari, Italy, 2005
- [55] M.Lunardon et al.: *The Barrel Sector Assembly System of the ALICE Silicon Pixel Detector*, IMTC Instrumentation and Measurement Technology Conference Como, Italy, 2004
- [56] See <http://www.ni.com>
- [57] M.Burns, *Status of MB cards and Rx card*, <http://alice1.web.cern.ch/alice1/Docs/Presentations/June2002/burns.ppt>
- [58] P.Chochulla et al.: *The ALICE Pixel Detector Readout Chip Test System*, 7<sup>th</sup> Workshop on Electronics for LHC Experiments, Stockholm, Sweden, 2001
- [59] M.Burns et al.: *The ALICE Silicon Pixel Detector Readout System*, Cracow 2000, 6<sup>th</sup> Workshop on Electronics for LHC experiments, CERN/LHCC/2000-041, 2000
- [60] M.Caselle et al: *The Database for the ALICE Silicon Pixel Detector*, ALICE Internal Note, ALICE-INT-2003-024, 2003
- [61] P.Riedler et al: *First results from the ALICE silicon pixel detector prototype*, Proceedings of the VERTEX 2001 conference, Brunnen, Switzerland, published in Nuclear Instruments and Methods in Physics Research A, 501 (2003) p. 111-118
- [62] P.Riedler: *Status of Wafer and Ladder Testing*, presentation given at the ITS SPD General Meeting, CERN, Switzerland, 2006
- [63] S.Ceresa and P.Riedler: *Leakage Current Measurement*, [http://spd-ladders.web.cern.ch/spd-ladders/ladder\\_setup.htm](http://spd-ladders.web.cern.ch/spd-ladders/ladder_setup.htm), CERN, Switzerland

- [64] J.Conrad and P.Nilsson: *Techniques to estimate the intrinsic resolution of the ALICE Silicon Pixel Detector with application to 2003 beam test data*, ALICE internal note, ALICE-INT-2005-003, CERN, Switzerland, 2005
- [65] F.Osmic & P.Riedler: *Investigation by SEM/EDX of wire bonding on a sensor for ALICE*, EDMS document, Id 545630, CERN, Switzerland, 2005
- [66] D.Glaude: *ALICE SPD VTT 122*, EDMS document, Id 672129, CERN, Switzerland, 2005
- [67] ALICE SPD Colaboration: *Beam test 2003 log book*, CERN, Geneva, Switzerland, 2003
- [68] P.Riedler: *ALICE SPD beam test 2003 summary*, presentation at CERN, Geneva, Switzerland, 2003
- [69] P.Nilsson and F.Osmic: *ALICE SPD beam test 2003 homepage*, <http://alice1.web.cern.ch/alice1/testbeam2003/index.aspon>
- [70] W.R.Leo: *Techniques for Nuclear and Particle Physics Experiments*, Springer Verlag, 1994
- [71] D.Elia et al.: *Study of the ALICE Silicon Pixel Detector performance in a beam test at the SPS*, ALICE internal note, ALICE-INT-2005-007
- [72] P.Riedler: *Joint Testbeam 2004*, presentation given at the SPD General Meeting, CERN, Switzerland, 2004
- [73] D.Nouais: *Common ITS beam test*, presentation given at the Technical Forum at CERN, Geneva, Switzerland, 2004
- [74] P.Riedler *SPD Participation in common ITS Beamtest - Status*, status report on the joint beam test 2004, CERN, 2004
- [75] Homepage of the ALICE Offline group, <http://aliweb.cern.ch/offline/>
- [76] J.Conrad: *ITS beam test 2004*, presentation given at the ALICE Offline Meeting, CERN, Geneva, Switzerland, 2005
- [77] M.Glaser: *CERN, Division PH-TA1-SD*
- [78] S.Haas: *The IEEE 1355 Standard: Developments, Performance and Application in High Energy Physics*, PhD thesis at the University of Liverpool, 1998
- [79] Hewlett Packard: *HP 81101A Pulse Generators, Technical Specifications, p/n 5967-6274E (Q4/98)*
- [80] SIFAM: *Network Expansion Module, PEC0118 Rev 2, Technical Specifications*
- [81] Terahertz Technologies Inc.: *TIA-950 O/E Converter, data sheet*
- [82] LeCroy: *9370 Series Digital Oscilloscopes 1 GHz Bandwidth, 2 GS/s, data sheet*, [http://ess.web.cern.ch/ESS/ePoolDoc/9699\\_2003.html](http://ess.web.cern.ch/ESS/ePoolDoc/9699_2003.html)
- [83] M.Glaser: *CERN, Division PH-TA1-SD*, private communications
- [84] F.Vasey: *CERN, Division PH-MIC*, private communications
- [85] B.WITTMER: *CERN, The Laser Alignment System for the CMS Silicon Microstrip Tracker*, PhD thesis at the Rheinisch-Westfälischen Technischen Hochschule Aachen, 2002
- [86] A.Sokolov: *Test of ALICE SSD-detectors with an infrared laser*, presentation at the ITS Meeting, CERN, 2002

- [87] Vishay Telefunken: *Physics and Technology - Emitters*, <http://www.vishay.com/>
- [88] M.Blouke et M.Nelson: *Stable ultraviolet antireflection coatings for charge-coupled devices*, SPIE 1900 (1993), 228-240
- [89] LEOT - Laser Technology, chapter 3-5: *Pulsed Solid Laser Test System*, <http://cord.org/cm/content1.htm>
- [90] Bronstein, Semendjajew, Musiol and Mühlig: *Taschenbuch der Mathematik*, 3., überarbeitete und erweiterte Auflage, Verlag Hari Deutsch, Frankfurt am Main, Thun, 1997
- [91] Radioactive Material Safety Data Sheet: *Cadmium-109*, [www.stuarthunt.com/Downloads/RMSDS/Cd109.pdf](http://www.stuarthunt.com/Downloads/RMSDS/Cd109.pdf)
- [92] D.Elia on behalf of the ALICE SPD Collaboration: *Performance of ALICE pixel prototypes in high energy beams*, proceedings of the PIXEL Conference Bonn, Germany, 2005
- [93] Z.Dolezal et al.: *Laser tests of silicon detectors*, submitted to Nuclear Instruments and Methods A (NIMA)
- [94] D.Elia et al.: *Sensor thickness dependance of the ALICE Silicon Pixel Detector performance*, ALICE internal note, ALICE-INT-2005-011, 2005
- [95] D.Elia on behalf of the ALICE SPD Collaboration: *SPD simulation: status of the fine tuning*, ALICE SPD General Meeting, CERN, Geneva, Switzerland, 2006
- [96] J.Conrad, J.G.Contreras and C.E.Jorgensen: *Minimum Bias Triggers in Proton-Proton Collisions with the VZERO and Silicon Pixel Detectors*, ALICE internal note, ALICE-INT-2005-025, 2005
- [97] T. Sjöstrand et al.: *Computer Physics Commun.* 135 238 (2001)
- [98] A.Kluge: *Status of the Pixel Trigger Processor (PIT)*, ALICE SPD General Meeting
- [99] F.Osmic et al.: *Infrared laser testing of ALICE silicon pixel detector assemblies*, proceedings of the PIXEL Conference Bonn, Germany, 2005
- [100] D.Gabor: *The Electron Microscope*, Hulton Press, London, 1944
- [101] Iowa State University: *Project ExCell*, <http://mse.iastate.edu/excel/>
- [102] Th.Gareth: *Transmission Electron Microscopy of Metals*, John Wiley & Sons, New York, 1962



## Curriculum Vitae

### ***Fadmar Osmić***

---

date of birth	14. March 1978
nationality	Austrian
marital status	single, 8 year old daughter
postal address in Austria	Kohlgasse 2a/29/2 A-1050 Vienna
postal address in France	156, rue du Mont Rond F-01630 St. Genis
phone	+41 76 5082091 (mobile) +41 22 7671829 (office)
email	fadmar.osmic@cern.ch



### ***Education***

---

expected in 06/2006 2003-2006	doctoral degree in physics doctoral thesis in physics at CERN, Geneva, Switzerland and Vienna University of Technology, Vienna, Austria "The ALICE Silicon Pixel Detector System"
10/2002 1996-2002	Diplom Ingenieur (master degree in physics) diploma studies in physics at the Vienna University of Technology, Vienna, Austria "Vergleich eines Si(Li) Detektors mit einem Si-Drift Detektor für TXRF Anwendungen"
1999-2000	Erasmus exchange program at the Royal University in Uppsala, Sweden
05/1996 1992-1996	Reifeprüfung (A levels) Gymnasium Diefenbachgasse Wien XV, Vienna, Austria

### ***Projects***

---

07/98-02/01	in total 6 month AOSA Telekom, Vienna, Austria: Development and utilization of a software tool for analysis of the telecommunication traffic
05/01-06/01	IAEA, Vienna, Austria (2 months), "Nuclear Threat Factor Calculations", Ao.Univ.Prof. Dr.phil. M. Tschurlovits
07/01-08/01	Siemens Medical Solutions, Erlangen, Germany (2 month), Modular Transfer Function for CT-applications, Ao.Univ.Prof. Dr.phil. Gurker